Measurement of the invisible width of the Z boson using the ATLAS detector

Nicholas Charles Kolpin (né Ryder)

(Nick Ryder)

St Cross College, University of Oxford



Thesis submitted in partial fulfilment of the requirements for the degree of Doctor of Philosophy at the University of Oxford

Michaelmas Term, 2013

Measurement of the invisible width of the Z boson using the ATLAS detector

Nicholas Charles Kolpin (né Ryder)
(Nick Ryder)
St Cross College, University of Oxford

Thesis submitted in partial fulfilment of the requirements for the degree of Doctor of Philosophy at the University of Oxford, Michaelmas Term, 2013

Abstract

The invisible width of the Z boson is its partial width to neutrinos and is a well known Standard Model quantity. A direct measurement of the Z boson's invisible width has been performed using the ATLAS detector. The width was measured to be $\Gamma(Z \to \text{inv}) = 481 \pm 5(\text{stat.}) \pm 22(\text{syst.})$, which rivals the precision of the direct measurements performed by the LEP experiments. Such a precise was measurement performed by measuring the ratio of $Z \to \nu\nu$ to $Z \to ee$ events and correcting for the differences between the neutrino and electron selections. The measurement is sensitive to any non Standard Model interactions with a jet(s) + undetected particle final state. No evidence was found for a deviation from the Standard Model, however improvements have been suggested to allow more sensitivity to new phenomena at high energies.

Acknowledgements

I would like to acknowledge the financial support that I received during my degree from the Science and Technology Facilities Council, the department of physics at the University of Oxford and the John Fell Fund. I would also like to thank members of the department's various support groups, in particular the particle physics secretaries, the UNIX support team and the mechanical and electronic workshops, without whom this work would not have been possible.

I would like to thank the three supervisors that I had over the period of my degree. No thanks can be enough for Tony Weidberg's years of advice, support and guidance. Tony was always available for discussions not only of my D. Phil. work but also for career guidance. He spent a considerable time critically assessing my work and greatly improved the written work in my thesis. Hugo Beauchemin also supervised my work on the measurement presented in this thesis. Not only was the measurement Hugo's idea, he also played a large role in guiding the design of the measurement and assessing the results that I found. I would also like to thank Todd Huffman for supervising an experiment that I performed that is not presented in this thesis. Together Todd and I built, tested and used a dual phase CO_2 cooling system to measure the radiation hardness of optical fibres. Todd was great fun to work with and this experiment was a great introduction to more practical physics experiments.

Finally I would also like to acknowledge the support of friends and family who made the years of my degree enjoyable. Most importantly I'd like to thank my lovely wife, Amy, for all her support and for generally making my life much happier. I'd like to thank my parents for their continued support and for ensuring that I had a good education. I'd also like to thank my fellow Oxford D. Phil. students who provided assistance with my work but more importantly made the time more fun.

Author's contributions

The analysis detailed in chapters 3 to 7 of this thesis was performed completely by the author. However the analysis relies on a number of contributions from the ATLAS collaboration. The analysis makes use of the data collected by the collaboration during the 2012 LHC proton-proton run. The analysis uses the data reconstructed by the collaboration and follows a number of recommendations from the collaboration. The initial idea for measuring the invisible width of the Z boson using the ATLAS detector comes from Hugo Beauchemin, who performed a similar measurement at CDF. Both Hugo Beauchemin and Tony Weidberg played an important part in designing the experiment in collaboration with the author.

In addition to the work detailed in this thesis the author also performed experiments to test the radiation hardness of optical fibres and optical splitters for the high luminosity upgrade of the LHC. These experiments are not detailed in the thesis as they form a separate body of work and have been published elsewhere[1, 2].

Contents

1 Introduction **2**
- 1.1 Previous measurements of the invisible width . . . 8
  - 1.1.1 Indirect measurements at LEP . . . 8
  - 1.1.2 Direct measurements at LEP . . . 10
  - 1.1.3 Direct measurement at CDF . . . 11
  - 1.1.4 Comparison of direct and indirect measurements . . . 12
- 1.2 The Large Hadron Collider . . . 13
- 1.3 Design of the invisible width measurement . . . 17

2 Event reconstruction **19**

3 Event selection **29**
- 3.1 $Z \to$ inv specific selection criteria . . . 30
- 3.2 $Z \to e^+e^-$ specific selection criteria . . . 32
- 3.3 Jet selection criteria . . . 33
- 3.4 Background rejection criteria . . . 34
  - 3.4.1 Non collision backgrounds . . . 35
  - 3.4.2 Bad events . . . 35
  - 3.4.3 QCD backgrounds . . . 36
  - 3.4.4 Electroweak backgrounds . . . 36
- 3.5 Data reduction . . . 37
- 3.6 Number of selected events . . . 37

4 Background estimations **46**
- 4.1 Background estimations in the jet + $Z \to$ inv channel . . . 46
  - 4.1.1 Monte Carlo estimations . . . 47
  - 4.1.2 Scaling MC estimations . . . 52
  - 4.1.3 QCD background estimation . . . 58
- 4.2 Background estimations in the jet + $Z \to e^+e^-$ channel . . . 64
  - 4.2.1 Monte Carlo background estimations . . . 64
  - 4.2.2 QCD background estimation . . . 66
- 4.3 Background removed $E_{\mathrm{T}}^{\mathrm{miss}}$ and $E_{\mathrm{T,had}}^{\mathrm{miss}}$ distributions . . . 69

5 Corrections to the measured ratio **74**
- 5.1 Z boson's p_{T} distributions and resolutions . . . 77
- 5.2 Trigger correction . . . 84
- 5.3 Electron correction . . . 86
- 5.4 Z boson's p_{T} correction . . . 90
- 5.5 Electron acceptance correction . . . 94

5.6 γ^* interference correction 98
5.7 Invisible width extraction 101

6 Estimation of systematic uncertainties 103
6.1 Background estimations 104
6.2 Parton density functions 107
6.3 Jets 109
6.4 Electrons 111
6.5 Pileup 113
6.6 Combined systematic uncertainty 115

7 Discussion of results 118

8 Conclusion 122

List of Figures

1.1 Diagram of $e^+e^- \to Z \to f\bar{f}$ interaction. . . . 3
1.2 Diagrams of $e^+e^- \to Z\gamma$ interaction. . . . 4
1.3 Feynman diagrams of Z + jet production at the LHC. . . . 5
1.4 The t-channel $e^+e^- \to Z \to e^+e^-$ interaction. . . . 9

2.1 Diagram of the ATLAS detector . . . 19
2.2 Jet Energy Scale uncertainty . . . 24
2.3 Electron identification efficiency . . . 25
2.4 $E_{\mathrm{T}}^{\mathrm{miss}}$ resolution . . . 28

3.1 Estimated $E_{\mathrm{T}}^{\mathrm{miss}}$ trigger efficiency . . . 31
3.2 Measured electron trigger efficiency . . . 33
3.3 $E_{\mathrm{T}}^{\mathrm{miss}}$ in the $Z \to$ inv channel . . . 38
3.4 $E_{\mathrm{T,had}}^{\mathrm{miss}}$ in the $Z \to$ inv channel . . . 38
3.5 $E_{\mathrm{T}}^{\mathrm{miss}}$ and $E_{\mathrm{T,had}}^{\mathrm{miss}}$ ϕ . . . 41
3.6 Leading jet p_{T} . . . 41
3.7 Number of jets . . . 42
3.8 Leading jet η . . . 42
3.9 Leading jet ϕ . . . 43
3.10 Leading jet $\eta - \phi$ in $Z \to ee$ channel . . . 43
3.11 Leading jet $\eta - \phi$ in $Z \to$ inv channel . . . 44
3.12 m_{ee} in $Z \to ee$ channel . . . 44
3.13 p_{T} distributions of the two electrons from the Z decay. . . . 45

4.1 Monte Carlo estimated $E_{\mathrm{T}}^{\mathrm{miss}}$ distributions in the invisible channel. . . 50
4.2 Sources of MC backgrounds in $Z \to$ inv channel . . . 51
4.3 Sources of MC backgrounds in $t\bar{t} \to e\mu$ sample . . . 53
4.4 Data / MC ratio in $t\bar{t} \to e\mu$ . . . 55
4.5 Sources of MC backgrounds in $W \to e\nu$ and $W \to \mu\nu$ channels . . . 56
4.6 Data / MC ratio in $W \to e\nu$ and $W \to \mu\nu$ . . . 57
4.7 $\Delta\phi(\mathrm{jet}, E_{\mathrm{T}}^{\mathrm{miss}})$ for nearest jet . . . 60
4.8 p_{T} of 'bad' jet in MC backgrounds . . . 60
4.9 p_{T} of 'bad' jet in lowest $E_{\mathrm{T}}^{\mathrm{miss}}$ bin . . . 61
4.10 Data - MC p_{T} of 'bad' jet in first bin . . . 61
4.11 Data - MC p_{T} of 'bad' jet in high $E_{\mathrm{T}}^{\mathrm{miss}}$ bins . . . 62
4.12 Data - MC p_{T} of 'bad' jet in smaller bins . . . 63
4.13 $E_{\mathrm{T,had}}^{\mathrm{miss}}$ distribution in MC estimated backgrounds . . . 65
4.14 m_{ee} templates . . . 67
4.15 m_{ee} fit . . . 68
4.16 $E_{\mathrm{T,had}}^{\mathrm{miss}}$ distribution in estimated QCD background . . . 68

4.17 Background removed $E_{\mathrm{T}}^{\mathrm{miss}}$ and $E_{\mathrm{T,had}}^{\mathrm{miss}}$ . . . 70
4.18 Measured ratio . . . 70
4.19 $E_{\mathrm{T}}^{\mathrm{miss}}$ and $E_{\mathrm{T,had}}^{\mathrm{miss}}$ ϕ . . . 71
4.20 Leading jet p_{T} . . . 72
4.21 Number of jets . . . 72
4.22 Leading jet η . . . 73
4.23 Leading jet ϕ . . . 73

5.1 Z boson's p_{T} distribution in $Z \to ee$ channel . . . 78
5.2 Ratio of data and SHERPA MC Z boson's p_{T} distributions. . . . 79
5.3 Invariant mass distributions in different bins of Zp_{T}. . . . 79
5.4 $E_{\mathrm{T}}^{\mathrm{miss}}$ and $E_{\mathrm{T,had}}^{\mathrm{miss}}$ compared to truth Z p_{T} . . . 81
5.5 $E_{\mathrm{T}}^{\mathrm{miss}}$ and $E_{\mathrm{T,had}}^{\mathrm{miss}}$ resolutions as a function of truth Z boson's p_{T}. . . . 82
5.6 Parallel and perpendicular $E_{\mathrm{T}}^{\mathrm{miss}}$ and $E_{\mathrm{T,had}}^{\mathrm{miss}}$ resolutions . . . 83
5.7 Estimated $E_{\mathrm{T}}^{\mathrm{miss}}$ and electron trigger efficiencies . . . 85
5.8 Trigger efficiency correction as a function of $E_{\mathrm{T}}^{\mathrm{miss}}$ or $E_{\mathrm{T,had}}^{\mathrm{miss}}$. . . . 85
5.9 Electron reconstruction efficiency scale factor distribution. . . . 87
5.10 Electron scale factor impact on $E_{\mathrm{T,had}}^{\mathrm{miss}}$ . . . 87
5.11 $E_{\mathrm{T,had}}^{\mathrm{miss}}$ with truth and reco electrons . . . 89
5.12 The electron selection correction as a function of $E_{\mathrm{T,had}}^{\mathrm{miss}}$. . . . 89
5.13 Z p_{T} correction . . . 92
5.14 Z boson's p_{T} correction with different selection criteria . . . 93
5.15 p_{T} distribution of electrons in jet + $Z \to e^+e^-$ events. . . . 95
5.16 η distribution of electrons in jet + $Z \to e^+e^-$ events. . . . 95
5.17 $\Delta R(e,e)$ distribution in jet + $Z \to e^+e^-$ events. . . . 97
5.18 Acceptance correction as a function of Z boson's p_{T}. . . . 97
5.19 m_{ee} in Z/γ^* and pure Z . . . 100
5.20 Correction factor, δ_γ, as a function of the Z boson's p_{T}. . . . 100
5.21 Product of different corrections as a function of Z boson's p_{T}. . . . 102
5.22 $\Gamma(Z \to \mathrm{inv})$ as a function of Z p_{T} . . . 102

6.1 Background estimation systematic shifts . . . 106
6.2 PDF systematic shifts . . . 108
6.3 Jet Energy Scale systematic shifts . . . 110
6.4 Electron systematic shifts . . . 112
6.5 Pileup stability . . . 114
6.6 Pileup stability in $E_{\mathrm{T}}^{\mathrm{miss}}/E_{\mathrm{T,had}}^{\mathrm{miss}}$ . . . 114
6.7 Measured invisible width of the Z boson as a function of its p_{T}. . . . 117

List of Tables

1.1 PDG full and partial widths 9
1.2 Direct $\Gamma(Z \to \text{inv})$ measurements 11
1.3 LEP and CDF combined widths 13

3.1 Events passing the selection criteria in the $Z \to \text{inv}$ channel. 39
3.2 Events passing the selection criteria in the $Z \to ee$ channel. 40

4.1 MC samples 49
4.2 MC background estimations in $Z \to \text{inv}$ channel 51
4.3 Size of estimated QCD background in different $E_{\mathrm{T}}^{\mathrm{miss}}$ bins. 63
4.4 MC background estimations in jet $+ Z \to e^+e^-$ channel 65
4.5 Full background estimations in $Z \to \text{inv}$ channel 69
4.6 Full background estimations in jet $+ Z \to e^+e^-$ channel 71

5.1 Summary of the definitions of terms used in the correction. 76
5.2 Events passing the electron requirements. 96
5.3 Events in Z/γ^* and pure Z 99

6.1 Estimated systematic uncertainties due to background estimations. . 106
6.2 Systematic uncertainties on the invisible width measurement. 115

Chapter 1

Introduction

The Standard Model of particle physics very successfully explains most experimental results. With the recent discovery of the Higgs boson all of the particles within the Standard Model have been discovered. However there are problems with the Standard Model, particularly at the TeV scale where new phenomena are expected to explain the huge discrepancy between the electroweak scale and a theorised grand unification scale. The high energy and luminosity of the Large Hadron Collider make it ideal for searching for evidence of physics beyond the Standard Model. Such searches can either be tuned to maximise the sensitivity to specific new theories or alternatively search in a model independent way by precisely measuring a well known Standard Model value in order to check for any deviation due to new phenomena. The latter approach is used in this thesis by measuring the invisible width of the Z boson.

Unstable particles that are produced by a resonance have a decay width, Γ, which is proportional to the the inverse of their lifetime. The total decay width of the Z boson was measured precisely by the experiments at the Large Electron-Positron collider (LEP) to be $\Gamma = 2.4952 \pm 0.0023$ GeV [3]. In the Standard Model of particle physics the Z boson can decay into any fermion + anti-fermion pair, excluding a pair of top quarks. This interaction is shown in figure 1.1. For each decay channel, $Z \to f\bar{f}$, a partial width $\Gamma_{Z \to f\bar{f}}$ can be determined as the product of the total width with the branching ratio for decays into $f\bar{f}$. The invisible width of the Z boson,

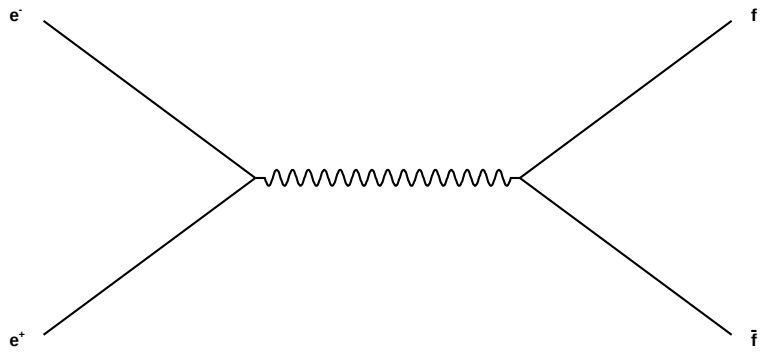


Figure 1.1: Feynman diagram of $e^+e^- \to Z \to f\bar{f}$ interaction, measured at LEP.

$\Gamma(Z \to \text{inv})$, is the partial width to any final states that are not detected by standard collider detectors. In the Standard Model this corresponds only to the decay into neutrinos, however many extensions to the Standard Model introduce new invisible final states that mimic $Z \to \nu\nu$ decays.

The LEP experiments were able to identify the different Z decay states by identifying electrons, muons, taus and hadrons. By measuring the cross sections for

$$e^+e^- \to Z \to f\bar{f}$$

as a function of the centre of mass energy, close to the Z mass of 91 GeV, they were able to perform fits of the Z line shape and extract measurements of the Z mass, total width and the partial widths to electrons, muons, taus and hadrons.

The LEP experiments used two different methods to measure the invisible width. The direct method required an initial state radiation (ISR) of a photon from either the electron or the positron and an invisible decay of the Z boson. The ISR photon gives the complete event signature - a single low energy gamma ray. This interaction is shown in figure 1.2. Using the sample of such events a measurement of the cross section for the invisible channel as a function of the centre of mass energy is made, from which a fit of the Z line-shape allows the extraction of the invisible width. The indirect measurement merely requires the definition that the invisible width is the difference between the measured total width and the sum of the measured visible partial widths. Both methods and their results are explained in detail in section 1.1.

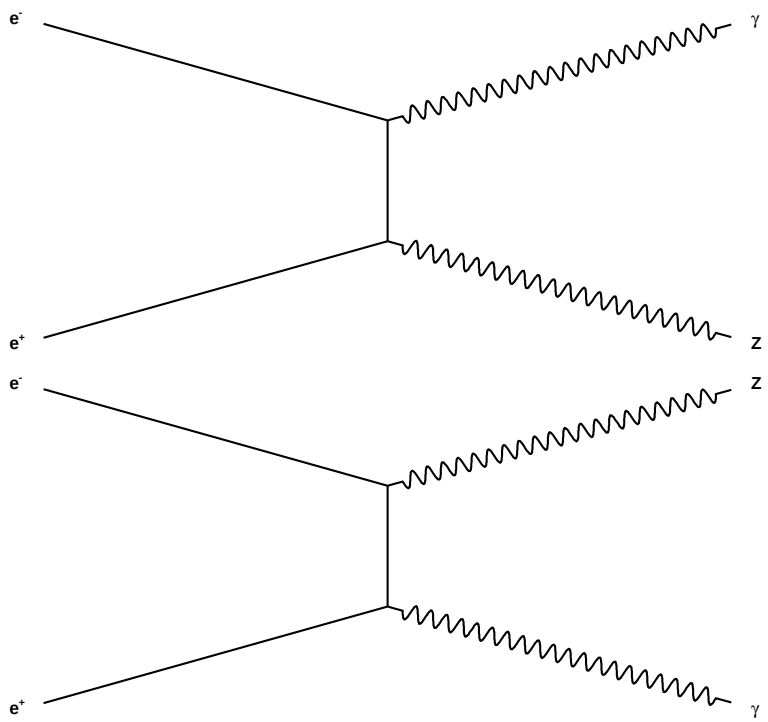


Figure 1.2: Feynman diagrams of $e^+e^- \to Z\gamma$ interaction, used for the direct measurement at LEP.

A direct measurement of the Z boson's invisible width is also possible at the LHC. Here the initial state gluon radiation can be used as an event signature, along with the missing transverse energy from the invisible particles since the Z boson is recoiling from the radiated gluon. Two possible interactions that produce the Z with an initial state radiation are shown in figure 1.3.

The LHC direct measurement has some advantages over the LEP measurements. The cross section for the required initial state radiation is larger by a factor of α_s/α_{EM}. The LHC has already collected data from a higher integrated luminosity than was used in the LEP experiments. However the LHC environment makes the measurement harder. At the LHC the total proton-proton cross section is more than seven orders of magnitude larger than the Z boson production cross section. In the invisible channel there are no leptons identified and so the events appear very similar to purely QCD events. The only difference is that the neutrinos contribute some missing transverse energy. In order to distinguish the invisible channel events from the much higher rate of QCD events, the Z boson is required to be recoiling from

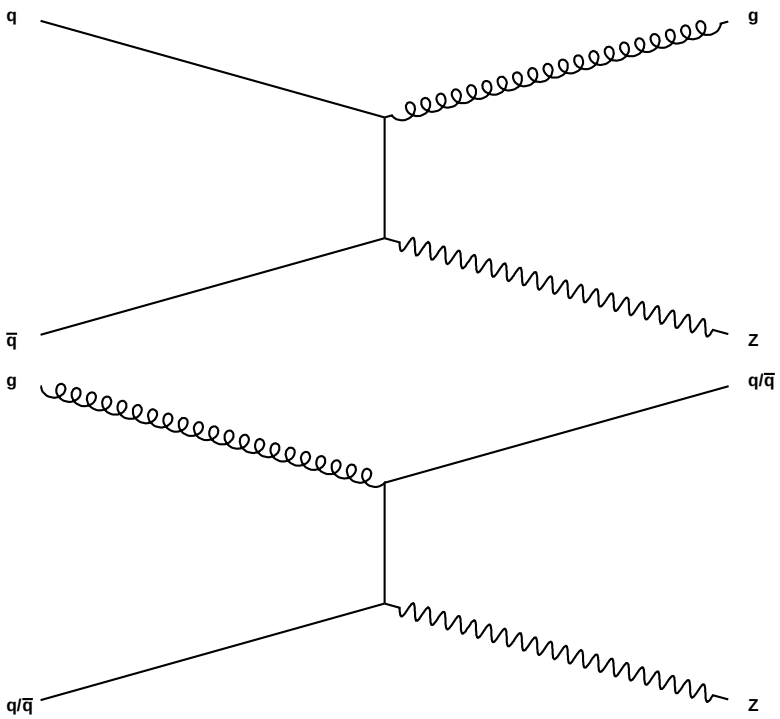


Figure 1.3: Feynman diagrams of Z + jet production at the LHC.

a high momentum initial state radiation. This recoil therefore gives a large missing transverse energy as the Z boson's momentum is converted into the combined momentum of the neutrinos. Importantly, since the centre of mass energy of the colliding partons is not known and cannot be controlled, only the total cross section can be measured rather than the cross section as a function of the centre of mass energy. A precise absolute cross section measurement is also difficult. Such a measurement would be limited by the uncertainties on the Jet Energy Scale (explained in chapter 2), the missing transverse energy resolution and also the uncertainty on the collected luminosity.

It is possible to avoid these uncertainties by taking advantage of the fact that the cross section for the Z + jet production and decay factorises as

$$\sigma(pp \to \text{jet} + (Z \to \nu\bar{\nu})) = \sigma(pp \to \text{jet} + Z) \times BR(Z \to \nu\bar{\nu}).$$

A suitable ratio measurement, comparing the jet + Z production in both the neutrino and a charged lepton channel can therefore cancel out the luminosity, jet

energy and missing transverse energy resolution uncertainties and result in the ratio of branching ratios,

$$R = \frac{\sigma(pp \to \text{jet} + Z) \times BR(Z \to \nu\nu)}{\sigma(pp \to \text{jet} + Z) \times BR(Z \to ee)} = \frac{BR(Z \to \nu\nu)}{BR(Z \to ee)}$$

from which the invisible width, $\Gamma(Z \to \text{inv})$, is extracted using a world average of the charged electron partial width

$$\Gamma(Z \to \text{inv}) = \Gamma(Z \to ee)^{\text{world}} \times R.$$

In order for the jet + Z cross sections to cancel the event selections in both channels must be carefully designed. The event selections used in this measurement are detailed in chapter 3.

There are two goals of this measurement. The first is to make a direct measurement of the invisible width of the Z boson with a precision that rivals that of the LEP direct measurements. The second is to provide a measurement of the ratio of the neutrino channel to the electron channel as a function of Z boson p_{T} that would be sensitive to any extra contributions from new interactions outside of the Standard Model.

Whilst it is not expected that an LHC based experiment will be able to reach the 0.3% precision of the LEP indirect measurements, a 3.5% precision, equalling the best LEP direct measurement may be possible. Although such a measurement would not improve the best knowledge of the invisible width it would form an important test of the Standard Model by making a measurement in a very different regime. Not only is the Z boson phase space quite different at the LHC due to the high missing transverse energy requirement, but the hadronic collision environment is also in contrast to the collisions at LEP. These factors should not affect the value of the invisible width.

The measurement should be insensitive to the Z boson's p_{T}. As such the ratio of neutrino to electron channels, following a correction procedure, should be flat as

a function of Z boson's p_{T}. Many extensions to the Standard Model introduce new interactions whose final states include particles that would be invisible to the detector. An example of such an extension is the existence of an interaction decaying into a pair of Dark Matter particles. If these Dark Matter particles only interact with the detector via the weak force then they would be invisible. The existence of such a final state would mimic the jet $+ Z \to \nu\bar{\nu}$ signature and would lead to an increase in the ratio above a threshold determined by such particles' mass. Importantly, previous LHC searches, such as [4], for such particles may have been insensitive to such a final state. These searches have focused on large additional contributions at high mass ranges and have not had the precision to measure a small additional contribution starting at a relatively low mass. The measurement of the invisible width, however, could be sensitive to such phenomena. The added sensitivity allowed by taking a ratio measurement and cancelling a number of systematic uncertainties therefore provides a robust, model independent method of searching for new interactions. The measurement presented in this thesis is corrected for all detector effects and can therefore be used by theorists to set limits on any theories which would alter the result. In order to set such limits a theorist would only have to calculate the extra contribution to the ratio from their model and compare the sum of the Standard Model and their contribution with the measured results presented in this thesis. It is unlikely that any new phenomena would introduce an extra contribution to the charged lepton channel since the requirement that the charged lepton pair has an invariant mass consistent with the Z boson's mass would mean that such a contribution should also have been seen in previous measurements.

This thesis details the direct measurement of the invisible width of the Z boson performed using data collected by the ATLAS detector at the Large Hadron Collider. In the remainder of this chapter previous measurements of the invisible width of the Z boson are summarised. The Large Hadronic Collider is then introduced, followed by a description of the design of the measurement presented in this thesis. In chapter 2 the ATLAS experiment is introduced and a brief explanation of how the

objects used in this analysis are reconstructed is given. Chapter 3 gives details of the event selection criteria that were applied to the invisible and electron channels and gives results of the two selections applied to the 2012 ATLAS data sample. Both channels select non Z decay background events as well as the desired $Z \to \nu\nu$ or $Z \to ee$ signals. Estimations of the various background sources are made in chapter 4 and the ratio of the background corrected values is found. In chapter 5 a number of corrections are calculated and applied to the measured ratio to take into account unavoidable differences in the two selection channels and then the measurement of the invisible width, along with the statistical uncertainty, is extracted. This is followed by an estimation of the systematic uncertainties on the measurement in chapter 6. In chapter 7 the result is discussed and areas where improvements can be made are identified. Finally chapter 8 contains a conclusion for the thesis.

1.1 Previous measurements of the invisible width

The Large Electron-Positron collider (LEP) made precision measurements of the Z boson. The LEP experiments made both indirect and direct measurements of the Z boson's invisible width. These measurements are explained in section 1.1.1 and section 1.1.2, respectively.

The CDF experiment at the Tevatron also made a direct measurement of the invisible width. This measurement is not included in the Particle Data Group's combination since it was not published, however details are given in section 1.1.3.

Comparisons between the direct and indirect measurements are made in section 1.1.4.

1.1.1 Indirect measurements at LEP

Indirect measurements of $\Gamma(Z \to \text{inv})$ were made at LEP [5, 6, 7, 8]. LEP collided electrons and positrons with a centre of mass energy around the Z mass, that scanned through a range (88-94 GeV). $e^+e^- \to f\bar{f}$ events were selected and the cross sections

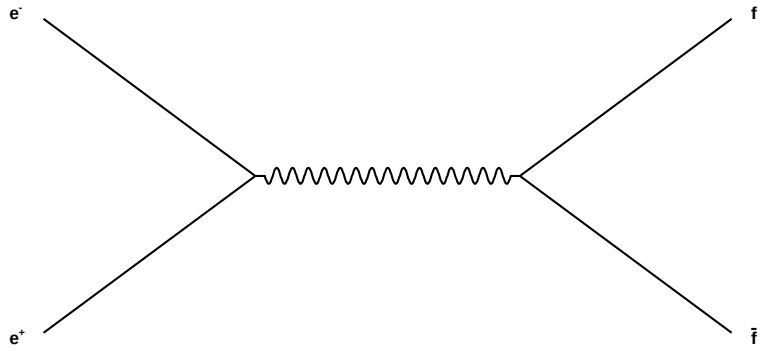


Figure 1.4: Feynman diagram of the t-channel $e^+e^- \rightarrow Z \rightarrow e^+e^-$ interaction, removed from the indirect measurement made at LEP.

Table 1.1: PDG fits of the full and partial widths of the Z measured by LEP experiments.

Width	PDG Fit (MeV)
$\Gamma(Z \rightarrow ee)$	83.91 ± 0.12
$\Gamma(Z \rightarrow \mu\mu)$	83.99 ± 0.18
$\Gamma(Z \rightarrow \tau^+\tau^-)$	84.08 ± 0.22
$\Gamma(Z \rightarrow \text{had})$	1744.4 ± 2.0
Γ	2495.2 ± 2.3
Indirect $\Gamma(Z \rightarrow \text{inv})$	499.1 ± 1.5

for each final state, at each centre of mass energy were calculated. The final states considered were e^+e^- (from which the t-channel contribution, shown in figure 1.4, was removed), $\mu^+\mu^-$, $\tau^+\tau^-$ and pairs of hadrons. No invisible final states were measured, and so the calculated invisible width is an indirect measurement. For each final state the shape of the cross sections as a function of centre of mass energy formed a Breit-Wigner resonance. The resonances were all subjected to a 9 parameter fit. The fit parameters included m_Z, Γ, $\sigma(Z \rightarrow \text{had})$, R_l, the ratio of the width into hadrons to the width into each lepton, and A^l_{FB}, the forward-backward asymmetry for each lepton. In this fit, where each lepton had an independent coupling, the leptonic partial widths were seen to be consistent with each other. A further 5 parameter fit was therefore made assuming lepton universality, from which the invisible width was extracted. Table 1.1 shows the PDG fit for each of the partial widths, the total width and the indirect invisible width.

1.1.2 Direct measurements at LEP

Direct measurements of $\Gamma(Z \to \text{inv})$ were made by the LEP experiments by measuring the cross section of

$$e^+e^- \to \gamma Z \to \gamma\nu\bar{\nu},$$

where the photon is from initial state radiation [9, 10, 11]. The three experiments used very similar event selection. Events were triggered based upon energy deposited in the electromagnetic calorimeter. Events were then selected containing a single energy deposit in the electromagnetic calorimeter at a high angle from the beam line which was consistent with a photon. Events with any tracks or significant energy deposited in the hadronic calorimeter were vetoed.

The dominant background came from radiative Bhabha scattering, $e^+e^- \to e^+e^-\gamma$, where the electron and positron are emitted close to the beam line and avoid detection. The backgrounds were estimated using Monte Carlo studies.

The cross sections for the process were measured at a range of centre of mass energies around the Z peak. The measured cross sections were then fitted to the function form of the $Z \to \nu\nu$ production at the reduced (by photon emission) centre of mass energy $\sqrt{s'} \approx \sqrt{s} - E_\gamma$

$$\sigma_0(s') = \frac{12\pi}{m_Z^2} \frac{s'\Gamma(Z \to ee)\Gamma(Z \to \text{inv})}{(s' - m_Z^2)^2 + s'^2\Gamma^2/m_z^2} \tag{1.1}$$

where Γ and $\Gamma(Z \to ee)$ are the total width of the Z and the partial width to electrons. The values of m_Z, Γ and $\Gamma(Z \to ee)$ were taken from previous measurements. Fitting this function over the cross sections found for the varying centre of mass energies, the experiments found the values of $\Gamma(Z \to \text{inv})$ shown in table 1.2. The differences in precision between the LEP experiments' results are due to the length of the LEP1 data periods used by each experiment. The L3 result has the most precise measurement since it used more than twice the integrated luminosity of ALEPH or OPAL.

Table 1.2: Directly measured values of $\Gamma(Z \to \text{inv})$ from the LEP experiments and CDF.

$\Gamma(Z \to \text{inv})$ (MeV)	Experiment	Year
$498 \pm 12 \pm 12$	L3	1998
$539 \pm 26 \pm 17$	OPAL	1995
$450 \pm 34 \pm 34$	ALEPH	1993
466 ± 42	CDF	2008

1.1.3 Direct measurement at CDF

A direct measurement of the invisible width was also made at CDF [12]. The measurement involved calculating the cross sections for events with Z + 1 jet in which the Z decayed into either l^+l^- (for both e and μ) or where it decayed into invisible particles (monojet events). These cross sections can be factorised as

$$\sigma(Z + 1\text{jet} + \text{inv}) = \sigma(Z + 1\text{jet}) \times \text{BR}(Z \to \text{inv}) \tag{1.2}$$

and

$$\sigma(Z + 1\text{jet} + l^+l^-) = \sigma(Z + 1\text{jet}) \times \text{BR}(Z \to l^+l^-). \tag{1.3}$$

Assuming events can be selected with the same Z + jet phase space, the ratio of the two measured cross sections then gives

$$\frac{\sigma(Z + 1\text{jet} + \text{inv})}{\sigma(Z + 1\text{jet} + l^+l^-)} = \frac{\text{BR(inv)}}{\text{BR}(l^+l^-)} = \frac{\Gamma(Z \to \text{inv})}{\Gamma(Z \to \ell\ell)}. \tag{1.4}$$

This ratio is then multiplied by the leptonic partial width given in the PDG to find $\Gamma(Z \to \text{inv})$.

The monojet sample was selected by requiring $E_{\text{T}}^{\text{miss}} > 80$ GeV, a jet with $p_{\text{T}} > 80$ GeV and $|\eta| < 1.0$, no other jets with $p_{\text{T}} > 30$ GeV and less than three jets with $p_{\text{T}} > 20$ GeV. A number of cuts were also used to reject the large backgrounds to the 'monojet' sample, such as a veto on isolated tracks, on jets with a high fraction of their energy deposited in the electromagnetic calorimeter, requiring the leading jet to have tracks associated with the primary vertex, etc. These selection criteria are

also important to the ATLAS analysis, and will be explained further in chapter 3.

The $Z \rightarrow l^+l^- + 1$ jet sample was selected by requiring two leptons meeting various quality requirements. The two leptons were required to have an invariant mass $66 < m_{ll} < 116$ GeV. In order to then select events with the same jet phase space as the invisible channel, a modified version of the monojet selections was also required. The monojet selections were modified in order to treat the charged leptons as if they were not present in the event. For example, events were vetoed if they had an isolated track other than the ones associated with the two leptons from the Z decay. In order for the Z cross sections to cancel a correction was made to the leptonic channel for the phase space that is lost due lepton - jet overlap removal and due to the acceptance of the lepton.

Combining the electron and muon measurements and using the LEP combined value for $\Gamma(Z \rightarrow ee)$ and $\Gamma(Z \rightarrow \mu\mu)$ resulted in a measurement of $\Gamma(Z \rightarrow \text{inv}) = 466 \pm 42$ MeV (also shown in table 1.2). The uncertainty on the measurement is dominated by the background estimation in the monojet sample. The uncertainty on the estimation is of the order 5%, however the background is almost twice the size of the $Z \rightarrow \nu\nu$ signal.

1.1.4 Comparison of direct and indirect measurements

The PDG gives values of the invisible width that are calculated from the four LEP experiments. These values, and also the unpublished CDF result are shown in table 1.3. The indirect measurements are much more precise than the direct ones. This is because the visible channels have higher statistics (since they do not require an initial state radiation) and also because the visible final states are easier to select with a low background rate. However the indirect measurements perform an important function in their comparison to the more imprecise direct measurement. It can be seen that the direct measurements agree with the indirect measurement, which can be used to set limits on beyond the Standard Model particles which either couple to the Z or which escape the detectors unseen, mimicking the Z to neutrino

decays.

The CDF measurement, although less precise than the combined LEP experiments, rivals the ALEPH experiment's precision. The CDF measurement's main importance is due to the fact that it comes from a completely different experimental regime. The Tevatron collided protons and anti-protons at the TeV scale, rather than electrons and positrons at the Z mass scale. The CDF experiment therefore probed events with hadronic initial state radiation, and was also sensitive to extra events from non Standard Model invisible particles with higher masses.

Table 1.3: Combined values of the invisible width of the Z boson from measurements by the LEP experiments and the direct measurement made at CDF.

Measurement	Invisible Width (MeV)
LEP Indirect	499.1 ± 1.5
LEP Direct	503 ± 16
CDF Direct	466 ± 42

1.2 The Large Hadron Collider

The LHC is a proton-proton collider built at CERN to push back the energy frontier and to provide enough particle collisions to allow the study of rare interactions. The LHC also provides lead-lead and proton-lead collisions. The LHC was built in the 27 km circular tunnel under Switzerland and France that was previously occupied by the LEP collider. Whilst it was designed to collide two proton beams with a centre of mass energy of 14 TeV, the LHC ran at 7 TeV in 2010 and 2011 and at 8 TeV in 2012. In 2013 the LHC then shut down for an upgrade period, following which the initial operation is planned with proton-proton collisions at 13 TeV centre of mass energy. The LHC is designed to deliver the 14 TeV collisions with a luminosity of 10^{34} $\mathrm{cm}^{-2}\mathrm{s}^{-1}$. By the end of the 8 TeV run in 2012 a peak luminosity of 7.5×10^{33} $\mathrm{cm}^{-2}\mathrm{s}^{-1}$ had been achieved.

The LHC hosts four main experiments. ATLAS and CMS are both general purpose detectors, designed to identify and measure the particles created in the

proton-proton collisions. The ATLAS detector was used for the analysis presented in this thesis and will be explained in more detail in chapter 2. They both have almost full 4π coverage around the collision point (with only small uninstrumented volumes around the beams). They have silicon based trackers immersed in a strong magnetic field at their centres, surrounded by sufficient calorimeters to stop all hadrons from the collisions and finally muon detectors on the outside of the calorimeters.

The LHCb experiment is designed to CP violation in interactions containing b quarks. The experiment aims to identify hadronic interactions with containing b quarks that are boosted in the lab frame. The detector therefore covers only a small solid angle in the direction of one of the beams. It consists of a silicon tracker very close to the beam line, the VELO, that is optimised to locate the collision vertex and also the vertices of any b quarks which decay a small distance from the collision. LHCb also has two ring imaging Cerenkov (RICH) detectors, which allow particle identification by measuring the velocity of the charged particles passing through it. The velocity can be combined with momentum measurements made by the main tracker, located between the two RICH detectors, to estimate the mass and therefore identify charged particles. Beyond the RICH detectors sit a calorimeter and a muon detector.

The ALICE experiment is designed to study lead-lead collisions. The collision events create a vast number of particles, requiring a design that differs significantly from the general purpose detectors. A large time projection chamber is used for the tracking. A time of flight and a RICH detector are used for particle identification. Also, a number of silicon disks are placed close to the beam line to provide a measure of the multiplicity of particles in the forward region and the centrality of the collision.

For ATLAS, the main goal of the LHC is to provide as many proton-proton collisions as possible. This is achieved by creating bunches of protons that are injected into the LHC ring at 450 GeV. During the 8 TeV run each beam had bunches separated by 50 ns. Following the injection the energy of the beams is ramped up from 450 GeV to 4 TeV. Data taking can then begin, with each data run

generally lasting over 10 hours. During the run the number of protons contained in the beam, and therefore the instantaneous luminosity falls as protons are lost due to collisions and collimation. At the beginning of a run each time the two proton beams crosses over 40 proton-proton interactions happen. As the luminosity falls the number of interactions per crossing, the in time pile-up, falls below 10. Over the 8 TeV run the average number of interactions per crossing was 20.7.

The high rate of collisions and the fact that many proton-proton interactions occur per collision were difficult requirements that the detector designs had to handle. Since collisions occur every 50 ns (the LHC is designed for collisions every 25 ns) it is not possible to read out all the detector information for every collision event. The bandwidth and computing resources required to read out and analyse the data are not feasible. As such the experiments have to decide upon a small subset of events to store. They therefore have trigger systems that aim to store a subset of events containing interesting interactions. The ATLAS detector uses a multi-stage trigger that considers less events, but in more detail, in successive stages. The collision rate of 20 MHz is reduced to 75 kHz by the Level 1 trigger, which is implemented in electronics located close to the detector, using low granularity data from the calorimeters and and the muon system's trigger chambers. The Level 2 trigger is implemented in a computing farm. It reduces the event rate to 3.5 kHz by considering the data at full granularity but only in regions of the detector thought to contain information about particles to reconstruct. Finally the Event Filter, also implemented in the computing farm, selects events to store at 200 Hz. The Event Filter uses the complete set of data from the detector when deciding whether to keep an event. A number of different triggers are used in selecting interesting events requiring, for example, reconstructed electrons or muons, high transverse momentum jets or a high level of missing transverse energy.

The high number of interactions per collision requires precise determination of the collision vertex, so that the particles originating from each interaction can be separated. The pile-up also leads to a higher occupancy in the tracker and calorime-

try, increasing the complexity of reconstructing tracks and degrading the momentum measurements of particles and also the missing transverse energy.

The fact that the LHC is a proton-proton collider adds a further level of complexity to analysing the data. Since protons are composite particles the interactions are not really between one proton and another, they are instead collisions between two partons. The partons, quarks or gluons, that collide carry a fraction of the proton's momentum. As such, the total momentum of the collision is not known. Since the protons have essentially no momentum in directions transverse to the beam line, the total transverse momentum of each collision must be zero. However, since the momentum of particles produced close to the beam line is not measured and the momentum of the colliding particles parallel to the beam line is unknown, the total momentum of an event is not known. Balancing the transverse momentum of the reconstructed particles is used to infer the existence of neutrinos (which are not detected) in an event. Since only the transverse momentum is known to be zero, the (sum of) neutrino momentum is only known in the transverse plane.

The fraction of the proton's momentum carried by the different flavours of quarks and by gluons is expressed by the parton distribution function (PDF). The PDF for each parton gives the probability to find a parton of that type, with a fraction, x, of the proton's momentum when probed at a resolution scale Q^2. The resolution scale is the magnitude of the 4-momentum transfer between the proton and the particle that is colliding with it. At higher momentum transfers more of the structure of the proton is resolved. The PDFs are estimated by fitting a range of experimental results with theoretical models that determine how the PDFs evolve when extrapolated to higher Q^2 values. The data comes from electron-proton, proton-proton, antiproton-proton and neutrino deep inelastic scattering experiments. Together the PDFs describe the proton as having three valence quarks in a sea of virtual quarks and gluons. PDF sets for collisions at the LHC are provided by a number of groups, with the PDF sets from CTEQ [13] and MSTW [14] used most commonly. Along with the best fit PDFs these collaborations provide uncertainties on the PDF intro-

duced by the experimental uncertainties from the input data and from the theoretical methods used to fit this data and evolve through different ranges of Q^2. At the LHC the PDFs need to be taken into account when creating simulated data samples. The probability for a simulated collisions between two specific partons can be found by the product of the PDFs for each of the two colliding partons with the Q^2 of the collision.

1.3 Design of the invisible width measurement

An ideal measurement of the invisible width of the Z boson, and the differential cross section ratio would involve only $Z \to ee$ and $Z \to \nu\nu$ interactions. The leptons would be measured perfectly in their full decay phase space and the momentum of the Z boson would be calculated from the sum of the leptons' momenta. The ratio of the full distributions of the Z bosons' momenta could be calculated to find the desired results.

The measurement has been performed using the ATLAS detector at the Large Hadron Collider. Since this is a hadron collider the $Z \to ee$ and $Z \to \nu\nu$ interactions are a small minority of the events from the proton collisions. The neutrinos escape the ATLAS detector undetected, and can only be inferred by calculating the missing transverse energy, $E_{\mathrm{T}}^{\mathrm{miss}}$, as the negative vector sum of the energy deposits that are measured. The $E_{\mathrm{T}}^{\mathrm{miss}}$ has a resolution that comes from the combined resolutions of the energy depositions and only gives information on the sum of the momentum of the neutrinos in the transverse plane. The $E_{\mathrm{T}}^{\mathrm{miss}}$ must therefore be used as a model of the Z boson's transverse momentum, p_{T}, rather than its total momentum.

Since $Z \to \nu\nu$ decays at rest would give a very low $E_{\mathrm{T}}^{\mathrm{miss}}$ and no visible leptons they appear very similar to purely hadronic interactions, which occur at a rate much higher than Z interactions. The measurement therefore requires a boosted Z, such that the sum of the two neutrinos' transverse momentum is large. Even with this requirement there are several large backgrounds, mostly due to $W \to l\nu$ events, where the lepton is not correctly identified, requiring a number of selection criteria

on the $Z \to \nu\nu$ channel to reduce these backgrounds.

Some of the electrons from $Z \to ee$ decays can be detected, however they are required to be within the η and p_{T} acceptance of the detector. The reconstruction of electrons within this acceptance is not fully efficient. Whilst the momentum resolution of the electrons is much better than that of hadronic activity it is still not perfect. The electrons from the Z decay may also radiate some of their momentum as photons. Photons that are co-linear with the electron have their momentum reconstructed along with the electron, however large angle radiations will be missed. The reconstructed electron momentum can therefore be underestimated due to these radiations.

The measurement has been designed to minimise of the impact of the effects of using a real detector. By taking a ratio and selecting events carefully many of the detector effects should cancel. For example, the 4-vector sum of the two reconstructed electrons would give the best measurement of the Z boson's p_{T}. However the hadronic recoil, the sum of those electrons and the underlying $E_{\mathrm{T}}^{\mathrm{miss}}$, is used. In this way the resolution of the Z boson p_{T} is as similar as possible in the two channels. Also, whilst the background in the $Z \to ee$ channel is much less than the background in the $Z \to \nu\nu$ channel, modified versions of the $Z \to \nu\nu$ channel's background rejection criteria are used in the $Z \to ee$ channel. The criteria are only modified such that the electrons from the Z decay have a minimal effect.

Chapter 2

Event reconstruction

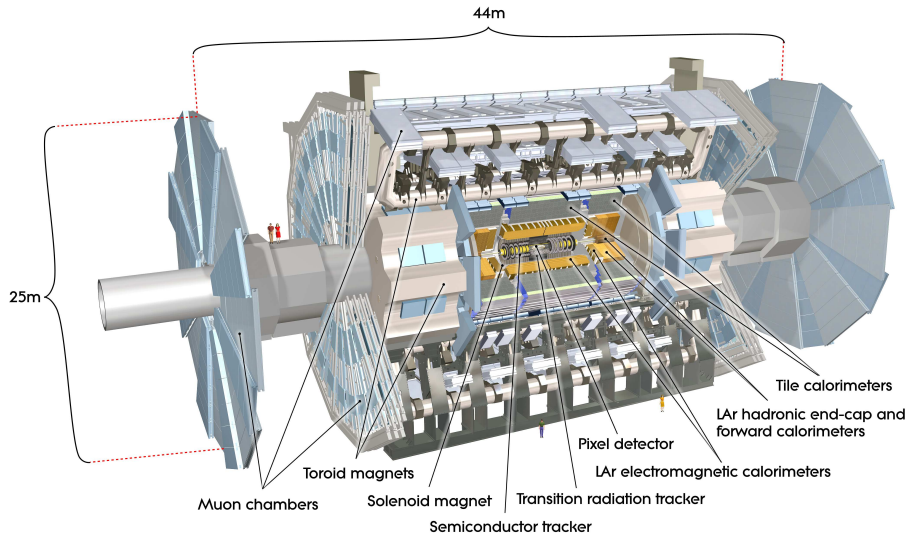


Figure 2.1: Diagram of the ATLAS detector [15].

The ATLAS detector is designed to detect, measure and classify particles emitted from the high energy proton-proton collisions provided by the LHC. The detector has three main components, shown in figure 2.1. The Inner Detector detects the paths of charged particles within the range $|\eta| < 2.5$, the calorimetry measures the energy of particles within the range $|\eta| < 4.5$ and the muon spectrometer measured the momentum of muons within the range $|\eta| < 2.7$. Using the measurements of these different detector components the electrons, photons, muons and hadronic jets coming from the collisions can be reconstructed. Neutrinos created in the collisions

cannot be directly detected, but can be inferred from an imbalance of the transverse momentum of the reconstructed particles. This analysis uses most of the physics objects that can be reconstructed from the data collected by the ATLAS detector. A detailed explanation of the detector and event reconstruction methods can be found elsewhere [16], however a brief explanation of the reconstruction of the objects used in this analysis is given here.

Closest to the collision, the Inner Detector (ID) measures the position coordinates of charged particles coming out of the collisions. The ID is constructed in layers. The innermost layers use silicon pixels, then there are layers of silicon strips and then finally straw tubes that are also capable of detecting transition radiation from electrons traversing layers with different refractive indices. The ID is immersed in a 2 T solenoidal field so that the charged particles follow curved paths, the trajectories of which can be used to measure the charge and momentum of these particles.

Outside of the ID the calorimeter stops most particles (except muons and neutrinos) and measures their energy. The calorimeter is realised in two technologies: liquid argon (LAr) and scintillator sampling calorimeters. The inner layer is a lead/liquid argon (LAr) sampling calorimeter commonly referred to as the electromagnetic calorimeter (ECAL) as its depth is sufficient to stop most electrons and photons. The inner layer of the LAr calorimeter consists of a barrel covering the range $|\eta| < 1.475$ and two end caps that cover $1.375 < |\eta| < 3.2$. The barrel region covers the η range of the silicon tracker and has high granularity that can be used to improve the matching of inner detector tracks to energy deposits in the calorimeter. Outside this calorimeter is the tile calorimeter in the central region of $|\eta| < 1.7$ that is segmented into a barrel and extended barrel regions. The tile calorimeter is a steel and scintillator sampling calorimeter that is 2 m thick. Outside the ECAL end caps there is a hadronic end cap LAr calorimeter using copper absorber, which extends over the region $1.5 < |\eta| < 3.2$. There is also a liquid argon forward calorimeter using copper and tungsten as absorbers extending over the range $3.1 < |\eta| < 4.9$. The large η coverage of the calorimeters and their depth is essential in measuring

the energy of outgoing particles with any significant transverse momentum. This is very important in this analysis, which relies on the measured imbalance of energy to infer the existence of neutrinos which do not interact with the detector.

Finally there is a muon spectrometer outside the calorimeter. This is used to identify and measure the momentum of the muons, which pass through the calorimeters since they are minimally ionising. The muon spectrometer includes both precision tracking elements (drift tubes and cathode strip chambers) and fast detection elements that can be used to trigger readout of the detector based on the presence of muons (resistive plate chambers and thin gap chambers). The muon spectrometer is immersed in a toroidal magnetic field of up to 3.5 T.

Tracks are reconstructed from the space points detected in the tracker. Using the inner pixel layers possible paths are extrapolated back to the beam line to find interaction vertices. Track seeds are created using the interaction vertices and hits in the inner pixel layers. The seeds are extrapolated outwards to find further hits in outer pixel or strip layers. If the hits in the other layers appear to fit a curve coming from the seed then they are added to form candidate tracks.

Individual hits may be assigned to multiple candidate tracks. This ambiguity is resolved by assigning scores to each track, where more hits add to the track's score and points are removed when a track passes through a tracker layer and no hit is identified. Shared hits are then assigned to the highest scoring track and the other tracks' scores are recalculated. Tracks whose scores fall below a threshold are discarded. Once the ambiguities are resolved the candidate tracks are extrapolated into the transition radiation tracker and matching hits from the straw tubes are added to the candidates to form the final tracks. Measurement of the final tracks' trajectories give the direction, momentum and charge of the charged particles coming from the collisions.

Jets are reconstructed as measurements of the energy of hadrons, electrons and photons measured in the calorimeters. The starting point of the jet reconstruction is the collection of energies measured in segments of the calorimeters. The energy

deposited in the calorimeter is measured by the drift of ionisation electrons in the liquid argon or the light produced in the plastic scintillators in the tile calorimeter and detected in photomultiplier tubes. The charge measured must first be calibrated to determine the amount of energy deposited by ionising particles in the argon or scintillator. This must be corrected by calibration for the energy deposited in the absorber layers of the calorimeter. This gives the so-called electromagnetic scale energy. For hadronic energy deposits this must be further calibrated by the Jet Energy Scale to account for the difference in energy deposited in the active calorimeter layers by neutral hadrons. Since the calorimeters are segmented and have different configurations of absorber and detector layers they must be calibrated based upon the position of the energy deposit and the longitudinal profile of the energy measured in different layers of the calorimeter.

Jets are formed from the energy deposits by first summing the energy clusters sharing the same angular locations, but in different radial layers to form towers. Neighbouring towers that are above a threshold are combined to form topological clusters. These are then classified as electromagnetic or hadronic based on the radial profile of the energy deposits (electromagnetic interactions deposit more energy in the liquid argon layers than the tile calorimeter, for example). The classified clusters are then calibrated to account for the energy lost to sampling, neutral interactions, dead material, etc. and for energy added by pileup. These calibrations have been determined from test-beam experiments, Monte Carlo simulations and data analyses such as balancing hadronic jets recoiling from photons [17]. The calibrations are measured for different locations in the calorimeter and different energy clusters.

The topological clusters are formed into jets using the anti-k_T algorithm [18] using a radius parameter, $R = 0.4$. This iterative algorithm takes a collection of trajectories and considers both a measure of the distance between each test trajectory and all other trajectories and a measure of the distance between the test trajectory and the beam. For each particle, i, the distance between the particle and

another particle, j, or the beam, B is defined as

$$d_{ij} = \min(1/k_{ti}^{-2}, 1/k_{tj}^{-2})\frac{\Delta R_{ij}^2}{R^2} \quad (2.1)$$

$$d_{iB} = 1/k_{ti}^{-2} \quad (2.2)$$

where k_{ti} is the transverse momentum of the ith particle, $\Delta R = \sqrt{(}\Delta\eta^2 + \Delta\phi^2)$ and R is the radius parameter used as an input for the algorithm. If the smallest of all the combinations of a distance is one of the d_{ij} then these two particles are combined into a single particle. If the smallest distance is a d_{iB} then the particle i is considered a finalised jet and removed from the collection. This algorithm is applied until all particles are combined into jets and removed. Importantly this algorithm's distance measurement depends on the inverse of the trajectories' momenta. This means that low momentum trajectories are much more likely to combine with a high momentum trajectory than another low momentum one. If a high momentum trajectory has no other high momentum trajectories within a distance of $2R$ then it will collect all low momentum trajectories within a circle of radius R. If there is another high momentum trajectory within $2R$, two jets will be formed that will share the nearby low momentum trajectories. The collection of jets that result from this algorithm is not greatly effected by particles radiating low energy particles or by a single particle splitting into two particles that are co-linear. As can be seen in figure 2.2 the uncertainty with which the jets can be calibrated to the Jet Energy Scale is below 4% and roughly 2% for jets with $100 < p_{\mathrm{T}} < 2000$ GeV. This figure shows the uncertainty arising from many sources in the jet energy scale calibration whilst only the total uncertainty is of interest.

The electron reconstruction is described in [20]. Electrons are reconstructed starting from seed liquid argon ECAL clusters. These clusters are found by summing the calorimeter clusters at the same angular coordinates, but in different layers, into towers. The clusters are calibrated based upon their local calorimeter response. The calorimeter is segmented in the $\eta - \phi$ space. For each segment a window of its 3×5 segment neighbours is inspected. If the sum of the energies of clusters within the

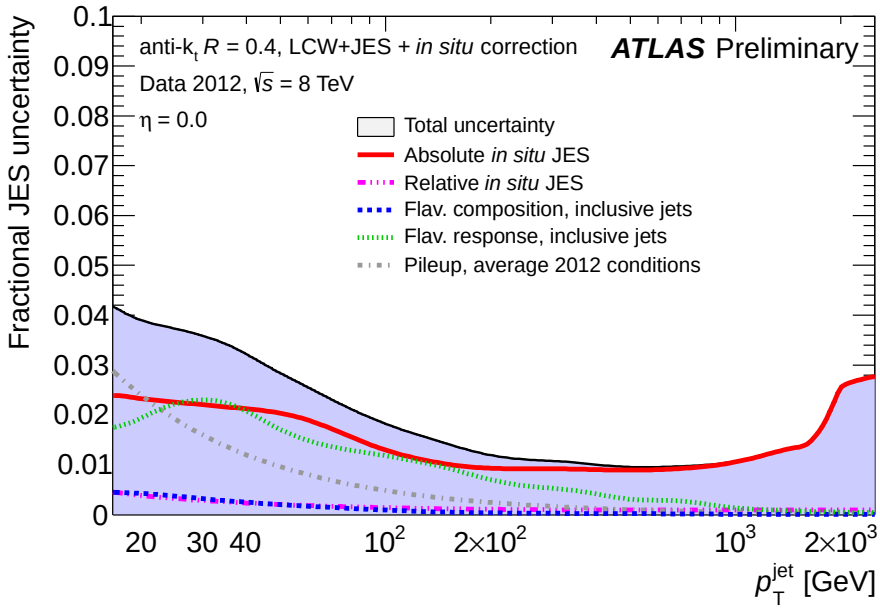


Figure 2.2: Fractional uncertainty on the Jet Energy Scale for central jets measured in 2012 data as a function of the jet p_T [19].

window is above a threshold then the cluster forms an electron candidate. If two such candidates are found in close proximity then the one with a lower energy is removed.

Inner detector hits found within a cone of $\Delta R < 0.3$ around the cluster candidates are used to search for track candidates. Tracks are reconstructed from these hits using an algorithm that takes into account bremmstraulung radiation from the electrons. The algorithm allows a loss of energy of the track when it traverses material in the detector. The electron identification then takes into account a number of parameters, such as the longitudinal energy deposition profile, the amount of leakage into the tile calorimeter, the track quality, the matching in direction and energy of the track and the cluster, the isolation of the track and the isolation of the energy deposited in the calorimeter. Using these parameters different levels of electron identification are made: loose, medium and tight identification. The loose electron identification is most efficient at identifying electrons, however it also misidentifies other objects, such as pions, as electrons at the highest rate. Tight electron identification is the least efficient at identifying electrons but has the lowest misidentification rate for other objects. Since the electron and jet reconstructions

are independent every reconstructed electron should also be reconstructed as a jet. The efficiency with which electrons are identified at different levels is shown in figure 2.3. The efficiencies have been measured in data and simulations by identifying Z boson decays, using one electron to tag the event and probing how often the other is identified using the different criteria [21]. The main class of electrons used in this analysis use the medium identification, but the loose identification is also used. The other identification methods that are also shown in the figure may be ignored.

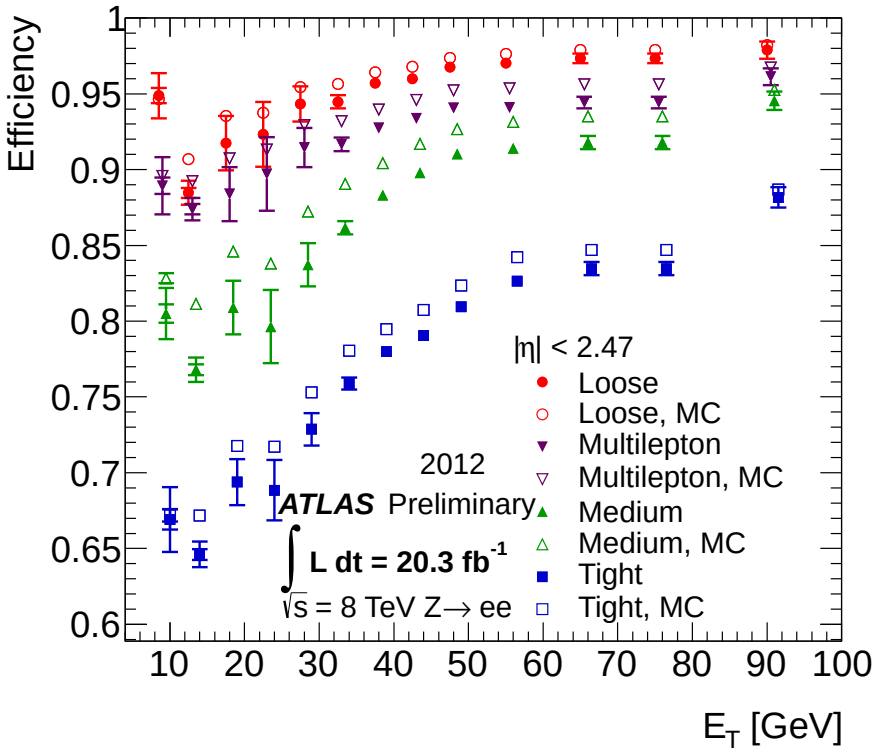


Figure 2.3: Measured and simulated efficiencies for electron identification as a function of the electron's transverse energy [21].

Muons are reconstructed using a track reconstruction in the muon spectrometer ($|\eta| < 2.7$) and/or inner detector ($|\eta| < 2.5$), as described in [22]. In this analysis 'combined' muons are used, where a track is reconstructed in both the muon system and the inner detector and these two tracks are matched to form the muon. Since the muon spectrometer extends over a larger range of η than the inner detector tracks outside the inner detector must come purely from the muon spectrometer. From the combined track the muon's momentum, charge and angular direction is found.

Two important quantities in determining the quality of the reconstructed muons are the track quality and the muon isolation. The track quality is a combination of the qualities of the inner detector and/or muon system tracks and how well they match. The tracks are assessed based upon the number of hits that form the track, any tracking layers that are passed where a hit is expected but not observed and the χ^2 of the procedure that matches the inner detector and muon system tracks. The isolation of the muon is defined as the ratio of the muon's transverse momentum to the sum of the transverse momenta of any tracks in a cone around the muon. By ensuring that a muon's momentum is significantly higher than the sum of the tracks around it, fake muons caused by hadronic jets where some particles are not absorbed in the calorimeter can be rejected.

The missing transverse energy, $E_{\mathrm{T}}^{\mathrm{miss}}$, is found to measure the sum of the transverse momentum of particles that do not interact with the detector. The 'RefFinal' version of the $E_{\mathrm{T}}^{\mathrm{miss}}$, explained in [23], is used in this analysis. The RefFinal $E_{\mathrm{T}}^{\mathrm{miss}}$ is first formed by taking the negative of the vector sum of calibrated energy deposits in the calorimeter. The jets, electrons and muons reconstructed in the event are then taken into account. The transverse energy of the deposits in the calorimeter associated with the reconstructed events are replaced by the transverse energy of the reconstructed particles. The $E_{\mathrm{T}}^{\mathrm{miss}}$ therefore depends on the reconstruction and identification of all other objects. The resolution of the $E_{\mathrm{T}}^{\mathrm{miss}}$, measured in $Z \to \mu\mu$ events ignoring the two muons, is shown in figure 2.4 [24]. The resolution increases from 5 to 15 GeV and is well modelled in the Monte Carlo. Importantly the $E_{\mathrm{T}}^{\mathrm{miss}}$ resolution is greatly improved by reducing the impact of pileup. The resolution is reduced due to the many soft proton-proton collisions that happen during the same bunch crossing as the collision of interest. These soft collisions contribute transverse momentum to the so-called 'soft term' in the $E_{\mathrm{T}}^{\mathrm{miss}}$ calculation. The impact due to pileup is reduced by scaling the soft term by the fraction of the momentum of the tracks in an event associated with the event's primary vertex, as explained in [24].

The hadronic recoil, $E_{\mathrm{T,had}}^{\mathrm{miss}}$, is also used in this analysis. It is used to mimic the

$E_{\mathrm{T}}^{\mathrm{miss}}$ in the $Z \to ee$ channel, by treating the electrons as if they were neutrinos. It is formed as the vector sum (in the transverse plane) of the $E_{\mathrm{T}}^{\mathrm{miss}}$ and the p_{T} of the two electrons identified as coming from the Z boson decay. The result is called the hadronic recoil since it is a measure of the hadronic activity left that is recoiling against the lepton system. The resolution with which the $E_{\mathrm{T}}^{\mathrm{miss}}$ and $E_{\mathrm{T,had}}^{\mathrm{miss}}$ measure the Z boson's p_{T} in this analysis is estimated using simulations in chapter 5.

The electron and missing transverse energy triggers are used in this analysis. Both triggers are seeded by the Level 1 calorimeter information. The electron trigger uses a combination of a low energy ($E_T > 24$ GeV) isolated electron or a high energy ($E_T > 60$ GeV) medium quality electron reconstructed at the event filter level. The choice of this trigger is explained in chapter 3. These are seeded by electromagnetic clusters of lower transverse energy at Level 1. Since the Level 1 measurement of the energy of the electron is less precise the lower Level 1 energy threshold avoids inefficiencies if the energy is underestimated at Level 1. The $E_{\mathrm{T}}^{\mathrm{miss}}$ trigger requires $E_{\mathrm{T}}^{\mathrm{miss}} > 80$ GeV at Event Filter level and $E_{\mathrm{T}}^{\mathrm{miss}} > 60$ GeV at Level 1, where the measurement is less precise. The efficiencies with which these triggers work to select events for this analysis are estimated in chapter 5, where they are both seen to be greater than 97% efficient.

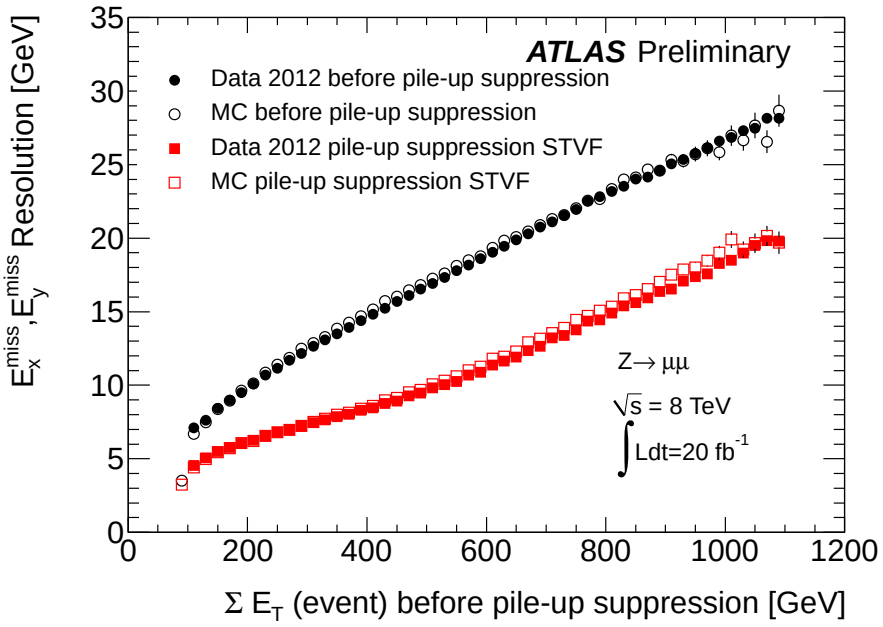


Figure 2.4: Measured and simulated $E_{\mathrm{T}}^{\mathrm{miss}}$ resolution as a function of the scalar sum of the transverse energy, using $Z \to \mu\mu$ events.

Chapter 3

Event selection

In order to measure the invisible width of the Z boson the ratio

$$R_{meas} = \frac{\sigma(\text{jet} + Z \to \text{inv})}{\sigma(\text{jet} + Z \to e^+e^-)} \tag{3.1}$$

is measured. This ratio requires events to be selected in the invisible (assumed to be neutrino in the SM) and electron channels.

The jet + $Z \to ll$ events have two components. Firstly, a parton-parton interaction produces a Z boson and a parton. Secondly, the Z boson decays into either a pair of neutrinos or an electron-positron pair. Events are selected in different channels based on the pair of final state particles from the Z decay. Care has been taken in the design of the measurement to minimise differences in the selection of events in the two channels. The measurement is designed to select events with the same hadronic activity, which is common to both channels. Events in the electron channel have a restricted Z decay phase space due to the limitations of detecting the electrons within the detector acceptance. The neutrinos (or non-Standard Model particles) in the invisible channel have a larger acceptance phase space since they are not directly detected, but only inferred from the missing momentum. However the difference in the Z boson phase space is minimised by treating the electrons as if they were invisible. This is done by ignoring the electrons identified as coming from the Z boson decay when performing lepton vetos, the isolated track veto, etc.

The selection for an initial state hadronic radiation is the same in both channels. This is made by requiring events to have a high transverse momentum (p_{T}), central jet. The selection for $Z \rightarrow$ inv is made by requiring the events to have large missing transverse energy ($E_{\mathrm{T}}^{\mathrm{miss}}$). The selection for $Z \rightarrow ee$ is made by requiring two electrons with an invariant mass consistent with the Z decay. Once the $Z \rightarrow ee$ selection has been made the electrons are treated as if they were invisible. As such a requirement on the hadronic recoil, $E_{\mathrm{T,had}}^{\mathrm{miss}}$, defined as the vector sum of the $E_{\mathrm{T}}^{\mathrm{miss}}$ and the p_{T} of the two Z decay electrons, is required to be above the same threshold set for the $E_{\mathrm{T}}^{\mathrm{miss}}$ in the invisible channel. A number of selection requirements are also made to reduce background events in the jet + $Z \rightarrow$ inv channel. The event selections for the two channels are discussed in detail in the following sections.

3.1 $Z \rightarrow$ inv specific selection criteria

In the invisible channel an imbalance of momentum transverse to the beam direction is used to infer the existence of the neutrinos (or other particles), which are not seen in the detector. The 'RefFinal' missing transverse energy, explained in chapter 2, is used to select transverse high momentum Z events which decay into neutrinos. The events are required to have $E_{\mathrm{T}}^{\mathrm{miss}} > 130$ GeV. Events are required to pass a $E_{\mathrm{T}}^{\mathrm{miss}}$ trigger with a threshold of 80 GeV explained in chapter 2. This trigger is highly efficient for the selected events, as can be seen in figure 3.1, where the estimation has been made using a Monte Carlo $Z \rightarrow \nu\nu$ sample. This threshold is set so that the reconstructed $E_{\mathrm{T}}^{\mathrm{miss}}$ is suitably higher than the trigger level estimation of the $E_{\mathrm{T}}^{\mathrm{miss}}$ such that the trigger should be highly efficient. The $E_{\mathrm{T}}^{\mathrm{miss}}$ threshold is also set high to reduce the QCD backgrounds introduced by badly measured jets. Since the estimation of this background is difficult the high $E_{\mathrm{T}}^{\mathrm{miss}}$ threshold avoids large uncertainties on the background estimation by reducing it to a low level.

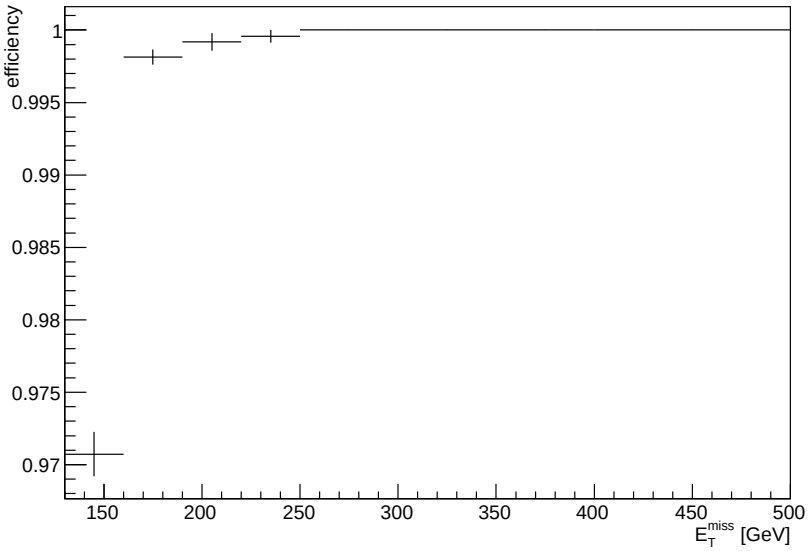


Figure 3.1: Estimated $E_{\mathrm{T}}^{\mathrm{miss}}$ trigger efficiency as a function of $E_{\mathrm{T}}^{\mathrm{miss}}$ found from Monte Carlo simulation.

3.2 $Z \to e^+e^-$ specific selection criteria

Events are required to pass one of two triggers. The first selects events with an isolated electron with $p_{\mathrm{T}} > 24$ GeV. The second selects events with an electron with $p_{\mathrm{T}} > 60$ GeV that may not be isolated. This is a standard ATLAS electron trigger combination, that provides high efficiency over a wide range of electron p_{T}. This combination trigger's efficiency, measured using a tag and probe method on $Z \to e^+e^-$ events [25], is shown in figure 3.2. This figure shows the efficiency at different trigger levels, only the Event Filter (EF) is relevant. The 'tag and probe' method involves identifying (tagging) one high quality electron from the Z decay and probing to see with which qualities the other electron is identified. The 'Event Filter' or EF level efficiency is of interest for this measurement. As can be seen the efficiency is above 90% for electrons with $p_{\mathrm{T}} > 30$ GeV and further increases to over 95% above 60 GeV. In this measurement the two selected electrons usually include one at high p_{T} (above 70 GeV) and at one low p_{T} (above 20 GeV). In this case the efficiency for either of the electrons to pass this trigger is above 98%. Electrons are selected requiring their calorimeter cluster to be either contained in the barrel of the electromagnetic calorimeter ($|\eta| < 1.37$) or in the endcap of the calorimeter ($1.52 < |\eta| < 2.47$) but not the overlap region where there is more inactive material and so the energy resolution is worse. Both electrons are required to have $p_{\mathrm{T}} > 20$ GeV and one is required to have $p_{\mathrm{T}} > 25$ GeV. The electrons are required to have been tagged as having 'medium' quality based on the calorimeter cluster shape, the number of hits that the track is reconstructed from and how well the track matches the calorimeter cluster [20].

To pass the jet + $Z \to e^+e^-$ selection each event is required to have exactly two such electrons. The electrons are required to have an invariant mass of $66 < m_{ee} < 116$ GeV. This provides a window of 50 GeV centred on the Z mass. Whilst a narrower window would keep most of the Z events and reduce the backgrounds in this channel a broad window means that the γ^* correction detailed in chapter 5 is small. Increasing the mass window further would allow this correction to be

minimised, however it would also impact the fit range for the QCD estimation performed in chapter 4. The two electrons are also required to be separated by $\Delta R(e^+, e^-) = \sqrt{\Delta\eta^2 + \Delta\phi^2} > 0.2$. This ensures that there is not a difficult to estimate loss of efficiency due to the shape requirements placed upon the electron's calorimeter shower if two electrons are in close proximity.

The event is required to have at least 130 GeV hadronic recoil to match the similar requirement on the neutrinos in the invisible channel.

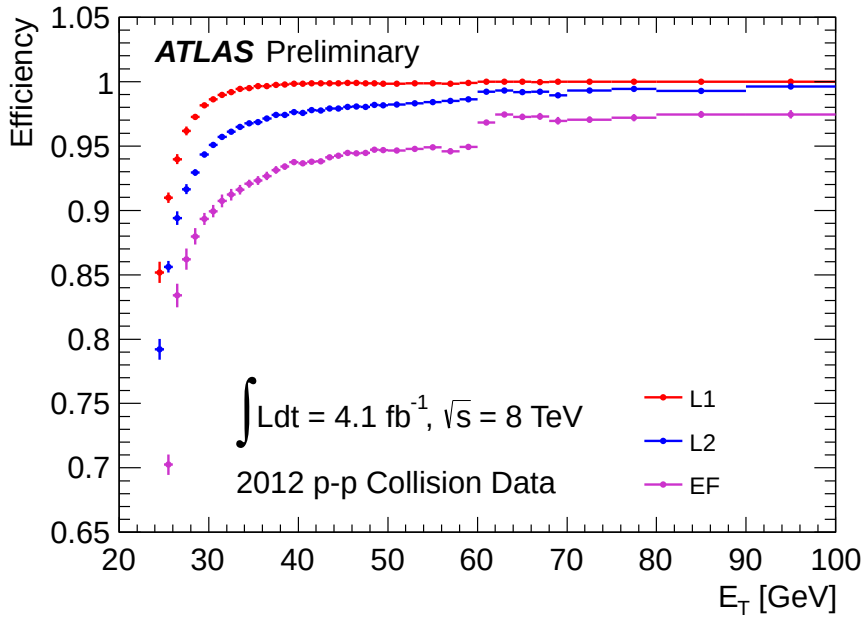


Figure 3.2: Measured electron trigger efficiency as a function of the electron's transverse energy [25]

3.3 Jet selection criteria

A collection of jets, as explained in chapter 2, is created for each event. For the jet$+Z \to e^+e^-$ channel any jet within $\Delta R(\text{jet}, e) < 0.2$ of a Z decay electron has its p_{T} reduced by the electron's p_{T}. In order to remove the correct amount of energy from the jet, the electron's energy is first scaled by the Jet Energy Scale used in forming the jet. The corrected momentum is then removed from the jet. This jet-electron overlap reduction attempts to remove the influence of the Z decay electrons

on the selection of the hadronic component of the events. In both channels jets are selected with $p_{\mathrm{T}} > 30$ GeV and $|\eta| < 4.5$. The η range is dictated by the coverage of the calorimeters, while the p_{T} threshold is required to have well reconstructed jet energy. Additionally, tracks in close proximity are associated with the jets. If any tracks are associated with the jet then the majority of the p_{T} of these tracks is required to come from tracks associated with the primary vertex in the event rather than any other vertices. This measurement is called the Jet Vertex Fraction (JVF). The primary vertex is defined to be the one with the largest scalar sum p_{T} of tracks associated with it.

The leading jet in each event is required to have $p_{\mathrm{T}} > 100$ GeV. The basic event topology of interest is a high p_{T} jet recoiling from a Z boson. Since the Z boson p_{T} measurement (either $E_{\mathrm{T}}^{\mathrm{miss}}$ or $E_{\mathrm{T,had}}^{\mathrm{miss}}$) is required to exceed 130 GeV a similarly high p_{T} jet is also required. However, whilst the leading jet p_{T} and the Z boson p_{T} are correlated the leading jet p_{T} is generally a little lower than the measured Z p_{T}. This is due to a contribution to the $E_{\mathrm{T}}^{\mathrm{miss}}$ from the underlying event and also the fact that the jet can radiate away some of its momentum. There is therefore a turn on effect in the $E_{\mathrm{T}}^{\mathrm{miss}}$ or $E_{\mathrm{T,had}}^{\mathrm{miss}}$ distribution due to the jet selection (which is detailed in chapter 5). The jet threshold of $p_{\mathrm{T}} > 100$ GeV has been selected so that this turn on does not have a large impact on the $E_{\mathrm{T}}^{\mathrm{miss}}$ or $E_{\mathrm{T,had}}^{\mathrm{miss}}$ distributions. No requirements are placed on the number of jets in an event in order to minimise the impact of the existence of the jets due to the Z decay electrons on the selection. Some backgrounds, particularly the $t\bar{t}$ background, could have been reduced by requiring a low number of jets, however the choice to minimise the jet phase space difference between the invisible and electron channels was made.

3.4 Background rejection criteria

There are a range of backgrounds in the two channels, predominantly in the invisible channel. Various selection criteria are required in order to minimise these backgrounds, as explained in the next sections.

3.4.1 Non collision backgrounds

Non collision backgrounds can come from spurious energy deposits in the calorimeters, from cosmic rays depositing energy in the calorimeters or from beams colliding with the beam pipe away from the detector causing showers hitting the detector from downstream. The main selection requirement for reducing non-collision backgrounds is that the leading jet is restricted to be in the range $|\eta| < 2$. This means that the leading jet is within the tracking acceptance and therefore has a measurable JVF. It is highly unlikely that any non collision background will have a high momentum jet with a large proportion of its associated tracks coming from the primary vertex. Additionally, events are required to have a primary vertex with at least three associated inner detector tracks. Also, two further requirements are placed on the leading jet in order to reduce the non collision backgrounds. The energy of the jet is measured in a number of layers of the calorimeter. The maximum fractional sampling, f_{max}, is the ratio of the maximum energy deposited in any one layer to the p_{T} of the jet itself. The charge fraction, ch_{frac}, of a jet is defined as the ratio of the sum of the p_{T} of the tracks associated with a jet to the p_{T} of the jet itself. The leading jet is required to have less than 85% of its energy measured in any single layer of the calorimeter ($f_{\mathrm{max}} < 0.85$). The charge fraction is required to be greater than one tenth of the maximum fractional sampling ($ch_{\mathrm{frac}} > 0.1 f_{\mathrm{max}}$).

3.4.2 Bad events

'Bad' events are removed by requiring that events are from running periods where all detector subsystems were performing correctly. Additionally events are rejected if there are errors reported by the liquid argon calorimeters or tile calorimeter. Events where the data is corrupted are also removed. Jet reconstruction quality is ensured by requiring that all jets with $p_{\mathrm{T}} > 20$ GeV meet the ATLAS 'looser' jet quality definition [26]. This definition is designed to veto events which contain jets from noise spikes in the hadronic endcap, noise in the liquid argon calorimeter, non collision events or cosmic rays. The definition takes into account the shapes of calorimeter

clusters, the fractions of the jet energy in the electromagnetic calorimeter, the charge fraction (ch_{frac}), maximum fractional sampling (f_{max}) and the amount of negative energy in the clusters the jet is formed from. Such negative energy clusters occur after pedestal removal, where the electronic noise has fluctuated the signal below the pedestal level.

3.4.3 QCD backgrounds

QCD backgrounds are introduced by mismeasurements of jets that contribute a fake $E_{\text{T}}^{\text{miss}}$. These events are removed by rejecting events with any jet (meeting p_{T}, η and vertex association requirements) which is pointed in a direction close to the $E_{\text{T}}^{\text{miss}}$. This is done by rejecting events for which any of these jets has $\Delta\phi(\text{jet}, E_{\text{T}}^{\text{miss}} \text{ or } E_{\text{T,had}}^{\text{miss}}) < 0.5$.

3.4.4 Electroweak backgrounds

Electroweak backgrounds come mostly from jet $+ W \to l\nu$ events. The number of such events is reduced by having a veto on electrons (except the two from the Z decay) or muons. Electrons are identified for the veto as specified in the jet $+ Z \to e^+e^-$ selection, however the full $|\eta| < 2.47$ range is used. Events with combined muons with $p_{\text{T}} > 7$ GeV and $|\eta| < 2.4$ that are isolated with a good quality track are vetoed. The isolation and track quality are explained in chapter 2. Additionally, in order to remove events with low p_{T} electrons, hadronically decaying taus, or leptons that were not reconstructed a veto is made on isolated tracks. Events with a good quality track with $p_{\text{T}} > 10$ GeV without another track with $p_{\text{T}} > 3$ GeV within a cone of $\Delta R(trk, trk) < 0.4$ are removed. The quality of the track is assessed by considering the position of the track, the number of hits the track is formed from and the χ^2 of the track fit to the hits. Tracks matched with electrons from the Z decay (using $\Delta R(e, \text{trk}) < 0.3$) are not included in this veto.

3.5 Data reduction

The events from the full 2012 ATLAS data set were selected in two steps. First an initial reduction of the data set was made, followed by an event selection for this reduced data set. Whilst the full data set is distributed around the world in many data centres, the reduced data set was sufficiently small to download a copy locally. This local copy could then be analysed more efficiently.

In the invisible channel the data reduction requirements were a combination of the $E_{\mathrm{T}}^{\mathrm{miss}}$ trigger and a lowered $E_{\mathrm{T}}^{\mathrm{miss}}$ requirement of 80 GeV. In the electron channel the electron trigger was required, along with a leading jet with $p_{\mathrm{T}} > 90$ GeV.

3.6 Number of selected events

The events used in this analysis were selected from 20.34 fb^{-1} of data taken with the ATLAS detector. Tables 3.1 and 3.2 show the number of events passing the various selection criteria for the jet + $Z \rightarrow$ inv and jet + $Z \rightarrow e^{+}e^{-}$ selections respectively. Figures 3.3 and 3.4 show the $E_{\mathrm{T}}^{\mathrm{miss}}$ and $E_{\mathrm{T,had}}^{\mathrm{miss}}$ distributions of the events passing the selection criteria. The tables give the relative percentage of events passing a given cut, compared to the number before that cut. The ATLAS data is split into different streams formed by collections of various triggers. The invisible channel and the electron channel come from different data streams, and so the initial number of events differs between the channels.

A number of distributions have been plotted for the events passing these selections to check that no obvious sources of unexpected events exist, as explained below. In plots showing distributions for both selection channels the number of events have been scaled to have the same integrated area. Figure 3.5 shows the ϕ direction of the $E_{\mathrm{T}}^{\mathrm{miss}}$ and $E_{\mathrm{T,had}}^{\mathrm{miss}}$ from the jet + $Z \rightarrow$ inv and jet + $Z \rightarrow e^{+}e^{-}$ channels. This distribution is flat, showing that there are no significant problems with the calorimeter that may bias the $E_{\mathrm{T}}^{\mathrm{miss}}$ or $E_{\mathrm{T,had}}^{\mathrm{miss}}$ direction. This also shows that the beam based backgrounds, which are likely to introduce $E_{\mathrm{T}}^{\mathrm{miss}}$ in the beam

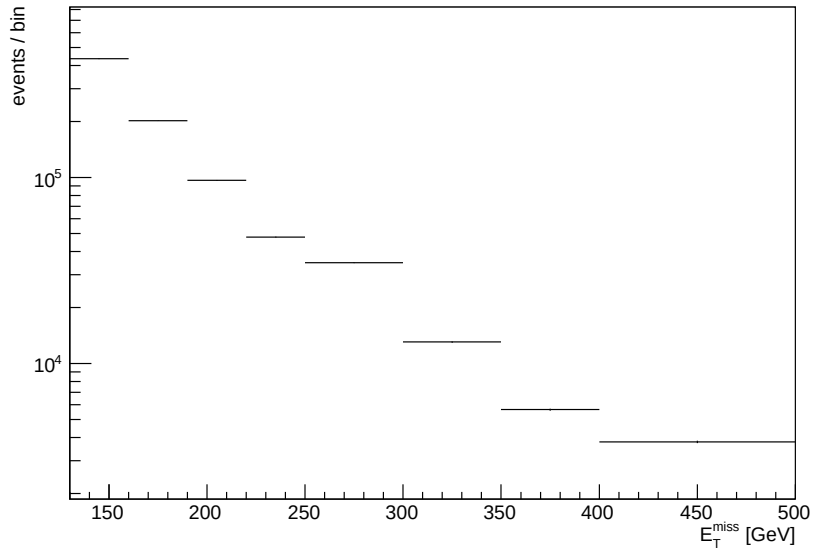


Figure 3.3: Missing transverse energy distribution in events passing the invisible channel selection.

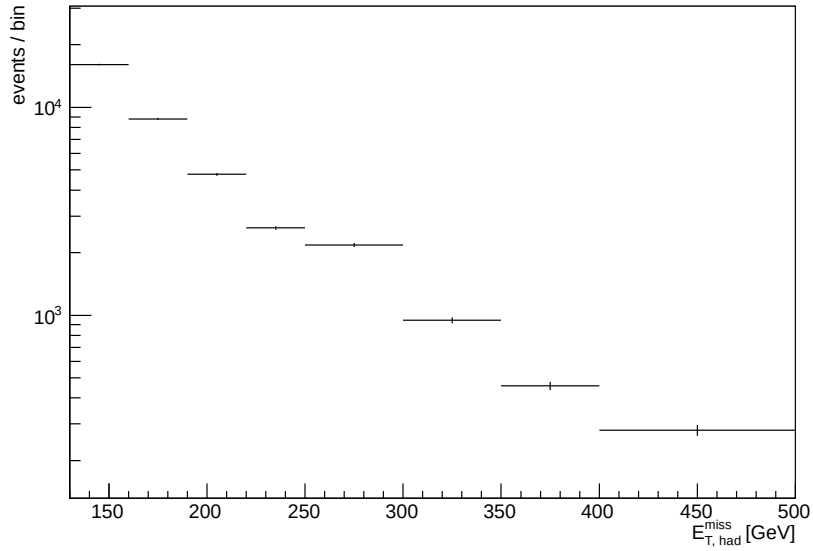


Figure 3.4: Hadronic recoil distribution in events passing the electron channel selection.

Table 3.1: Events passing the selection criteria in the $Z \rightarrow$ inv channel.

Criteria	Events	% passing
data reduction		
Initial	747882538	
$E_{\mathrm{T}}^{\mathrm{miss}}$ Trigger	39364669	2.56
$E_{\mathrm{T}}^{\mathrm{miss}} > 80$ GeV	17978741	45.67
event selection		
Initial	17978741	
Good Runs List	16819981	93.55
MET Trigger	16819981	100
Leading Jet	7964161	47.35
Vertex	7962123	99.97
Cleaning	7946538	99.80
Bad Events	7928113	99.77
Electron Veto	7526122	94.93
Muon Veto	6709241	89.15
Isolated Track Veto	5846832	87.15
$\delta\phi(\mathrm{jet}, E_{\mathrm{T}}^{\mathrm{miss}})$	2110437	36.10
MET	840154	39.81

plane are not significant. Figure 3.6 shows the p_{T} distributions of the leading jet in each event. Above 130 GeV a steeply falling p_{T} distribution is seen in both channels. Below this threshold a turn on effect due to the $E_{\mathrm{T}}^{\mathrm{miss}}$ or $E_{\mathrm{T,had}}^{\mathrm{miss}}$ requirement is seen. The leading jet threshold that is lower than the $E_{\mathrm{T}}^{\mathrm{miss}}$ or $E_{\mathrm{T,had}}^{\mathrm{miss}}$ thresholds was chosen in part so that this turn on effect would be seen in the leading jet p_{T} distribution, rather than a turn on due to the jet threshold in the observables used in the ratio. Figure 3.7 shows the distributions of the number of jets meeting the analysis requirements in each event. This plot indicates that the electron-jet overlap reduction method applied in the electron channel removes a small amount of jets compared to the neutrino channel. This difference in the jet phase space forms part of the correction applied in chapter 5. Figures 3.8 and 3.9 shows the η and ϕ distributions of the leading jet. The jets are distributed symmetrically in η and have a flat distribution in ϕ. This shows that the non collision background (which is unlikely to be symmetric in leading jet ϕ) must be small. It also shows, as confirmed in the three $\eta - \phi$ distributions shown in figures 3.10 and 3.11 that there are no spurious jets due to particularly noisy areas in the calorimeter, and no dead

Table 3.2: Events passing the selection criteria in the $Z \to ee$ channel.

Criteria	Events	% passed
data reduction		
Initial	519392027	
Electron trigger	319630662	61.54
Leading jet $p_{\mathrm{T}} > 90$ GeV	29547337	9.24
event selection		
Initial	29547337	
Good Runs List	28351550	95.95
Electron Trigger	28351550	100
Electron p_{T}	374568	1.32
Two electrons	373657	99.76
Electron separation	368426	98.60
Invariant mass	278374	75.56
Leading jet	106209	38.15
Electron veto	106134	99.93
Muon veto	105768	99.66
Vertex	105761	99.99
Cleaning	105618	99.86
Bad events	105407	99.80
Isolated track veto	98761	93.69
$\delta\phi(\mathrm{jet}, E^{\mathrm{miss}}_{\mathrm{T,had}})$	83826	84.88
Hadronic recoil	36196	43.18

areas in the calorimeter where jets are not seen. Figure 3.12 shows the invariant mass distribution in the $Z \to ee$ channel. The clear peak due to the Z boson shows that the events must have small background contributions. This is confirmed in the background estimation performed in chapter 4. Figure 3.13 shows the p_{T} distributions of the leading and sub-leading electrons from the Z decay. This confirms that the events mostly contain a high p_{T} electron and a lower p_{T} one, and so the electron trigger used should be highly efficient.

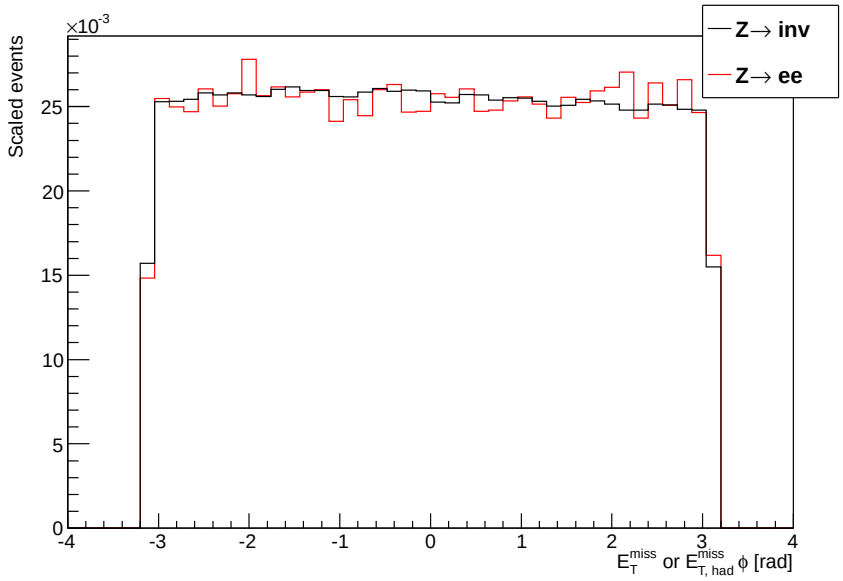


Figure 3.5: Hadronic recoil and missing transverse energy ϕ distributions in events passing the electron and invisible channel selections.

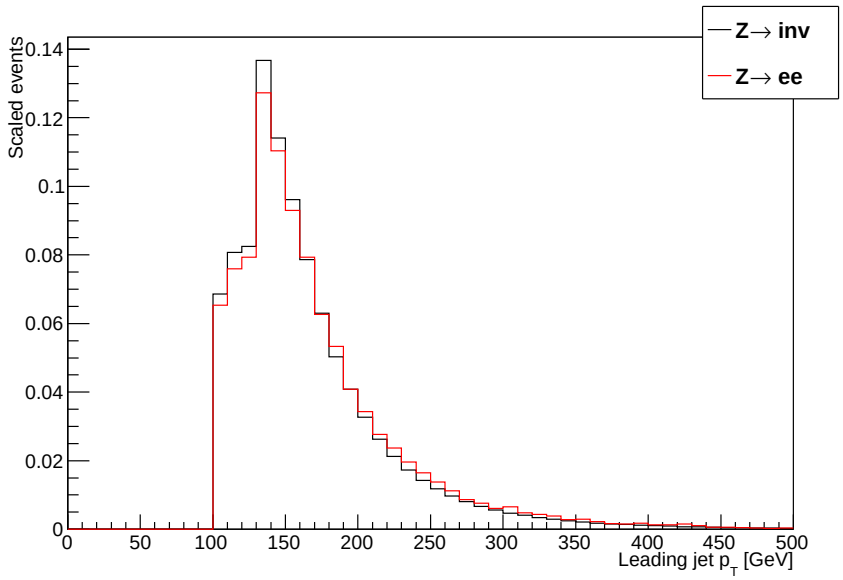


Figure 3.6: Leading jet p_{T} distribution in events passing the electron and invisible channel selections.

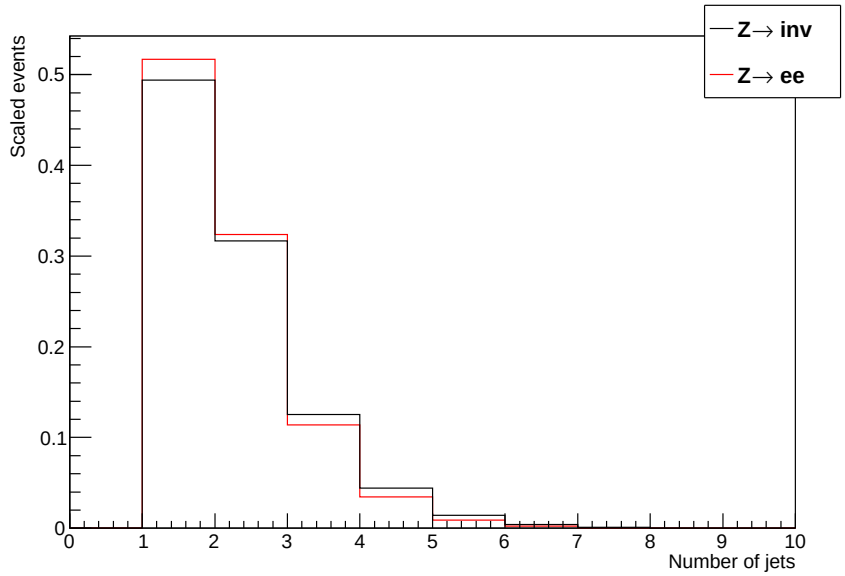


Figure 3.7: The number of jets in events passing the jet+$Z \to$ inv and jet+$Z \to e^+e^-$ selections.

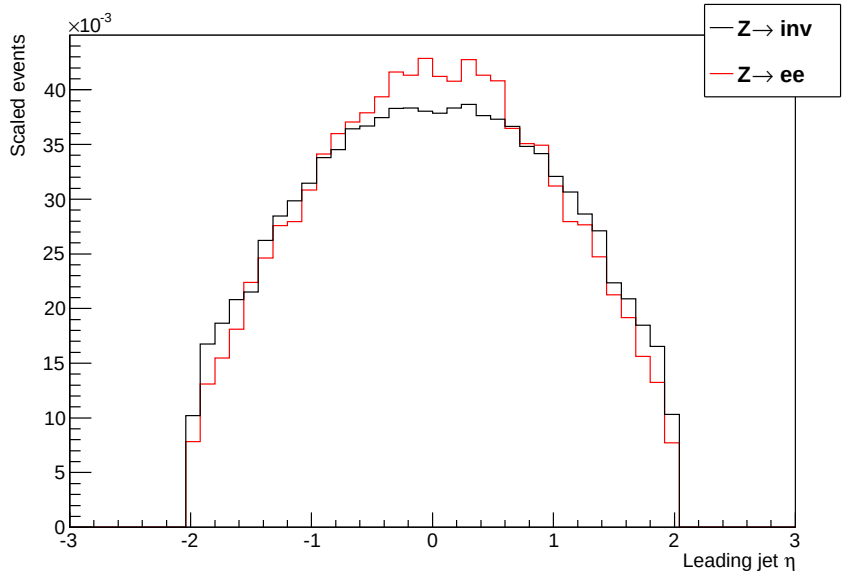


Figure 3.8: Leading jet η distribution in events passing the electron and invisible channel selections.

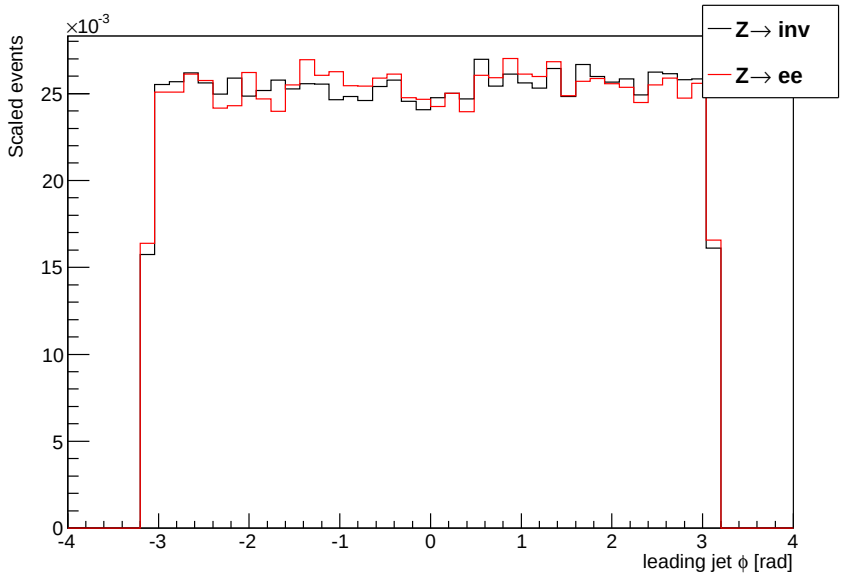


Figure 3.9: Leading jet ϕ distribution in events passing the electron and invisible channel selections.

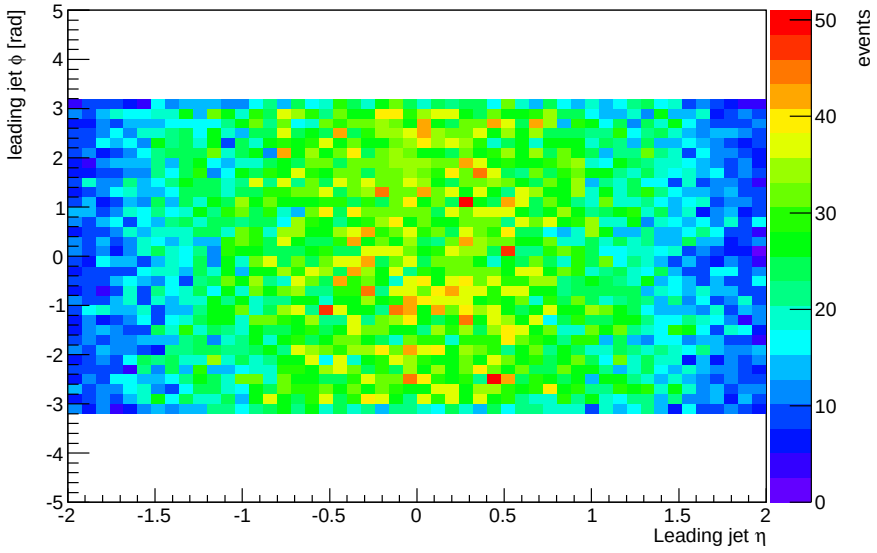


Figure 3.10: Leading jet $\eta - \phi$ distribution in events passing the electron channel selection.

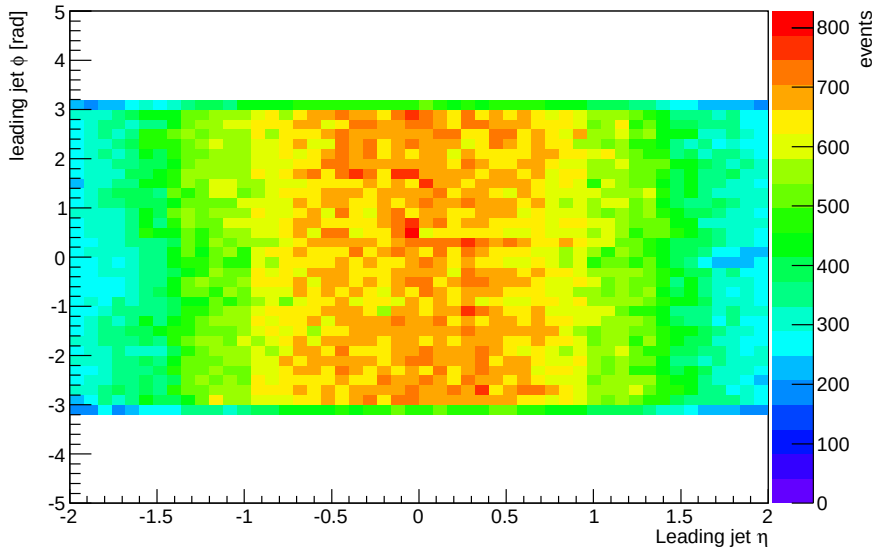


Figure 3.11: Leading jet $\eta - \phi$ distribution in events passing the invisible channel selection.

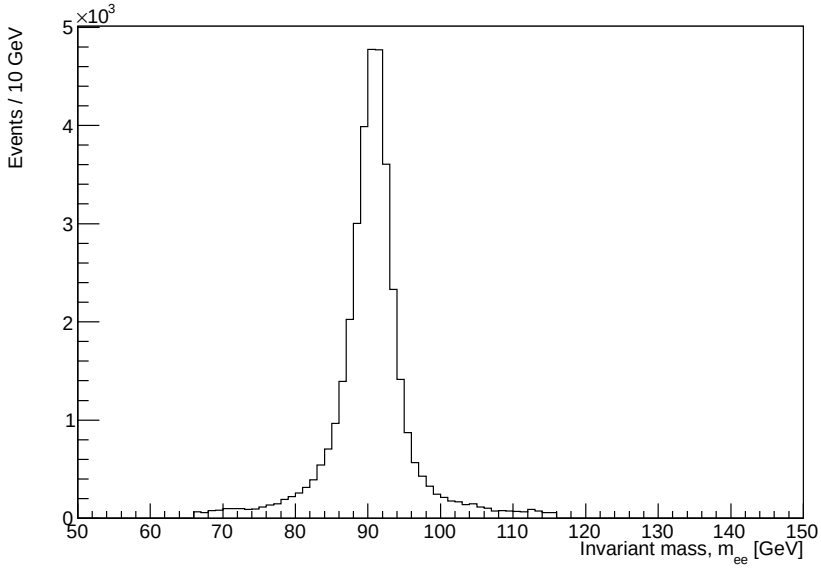


Figure 3.12: Invariant mass of the electrons from the Z decay in events passing the jet + $Z \to e^+e^-$ selection.

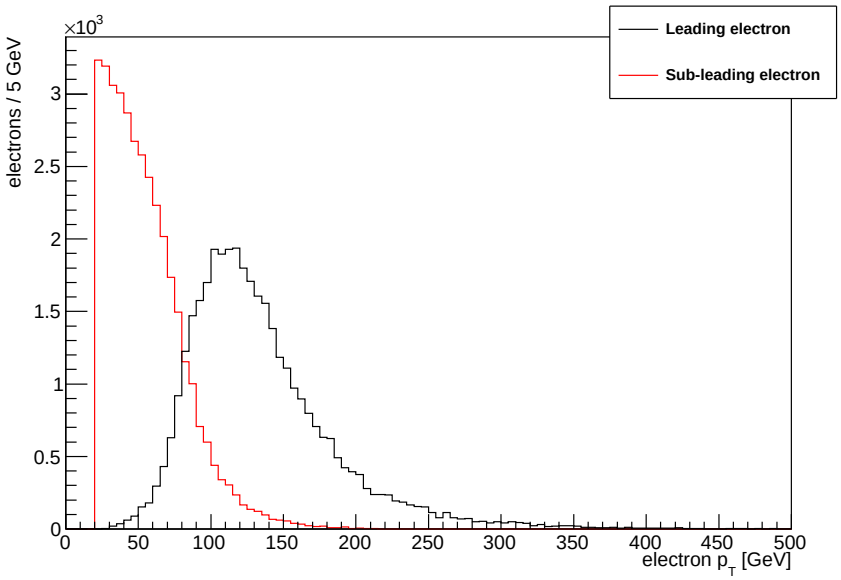


Figure 3.13: p_{T} distributions of the two electrons from the Z decay.

Chapter 4

Background estimations

The jet $+ Z \to e^+e^-$ and jet $+ Z \to$ inv event selections do not provide pure samples of events. The invisible channel, in particular, has large backgrounds since the neutrinos are only inferred, rather than directly measured. The electron channel has only a small background contamination since the requirement to have two electrons consistent with a Z boson decay reduces the chance that non Z interactions are accidentally selected. This section gives details of the background estimations in the two channels.

4.1 Background estimations in the jet $+ Z \to$ inv channel

The main backgrounds in the jet $+ Z \to$ inv channel come from other electroweak processes with charged leptons in the final state where the lepton was not reconstructed. Other significant background sources are events with two weak bosons or $t\bar{t}$ events, where there is true $E_{\mathrm{T}}^{\mathrm{miss}}$ and any leptons are missed. The background estimation for these sources has been calculated using Monte Carlo simulated samples. The Monte Carlo based background estimations are made in section 4.1.1. In order to avoid theoretical uncertainties in scaling the simulated events to the luminosity of the data collected, data driven estimations of Monte Carlo scaling factors are

calculated in section 4.1.2.

Another, although smaller, background comes from QCD events where jets have been mismeasured to introduce fake $E_{\mathrm{T}}^{\mathrm{miss}}$, or where heavy flavour quarks have decayed and final state leptons have not been identified. For QCD events to be selected in the invisible channel they require jets that have been badly mismeasured to produce $E_{\mathrm{T}}^{\mathrm{miss}} > 130$ GeV. Whilst the mismeasurement of jets can be modelled in the MC simulations such extreme events are rare. Relying on simulations to estimate the QCD background would have resulted a large uncertainty since it would have relied on small statistics in the tails of the mismeasured jet distributions. Instead the event selection has been designed so that this background should be small, and a data driven technique for estimation is explained in section 4.1.3.

4.1.1 Monte Carlo estimations

Monte Carlo background estimations were made mostly using simulated samples created using SHERPA [27]. SHERPA is a MC event generator using a tree-level matrix element generator and parton showering with a matching scheme to accurately estimate multi-jet final states. The matching scheme is needed to avoid, for example, double counting an event with n + 1 jets from the matrix element as well as a similar event with n jets from the matrix element and an additional jet from parton showering. SHERPA also takes into account initial and final state radiation, collisions with multiple parton interactions, and the proton PDF. The samples used in this analysis use the CT10 PDF[28]. The single top quark backgrounds do not use SHERPA, but instead were generated using POWHEG BOX[29] (or, in the case of the t-channel AcerMC[30]) interfaced to PYTHIA[31]. The different generators were used in the single top channels since validated SHERPA samples were not available. Additionally, since a data driven scaling of the single top background is not possible the estimation is improved by using next to leading order (NLO) generators. The single top samples use the CTEQ6.1 PDF set [13]. A list of the simulation samples used is given in table 4.1.

During the 2012 ATLAS data run the beam conditions changed significantly. The beam intensities increased over the year, increasing the number of collision interactions in each beam crossing. The number of simultaneous collisions, known as the pileup, affects the detector performance. The simulated events were weighted such that they match the pileup conditions experienced in the full year's data set. Some of the SHERPA samples have weights for each event, which were applied. The electrons and muons have their energy scaled and smeared to match the energy reconstructed in data. Other than this the backgrounds have been estimated by selecting events from the simulated sample using the same selection criteria used for the data sample.

The $E_{\mathrm{T}}^{\mathrm{miss}}$ distribution has been found for each sample and this has been scaled to represent the luminosity of 20.34 fb^{-1} that was collected in the year's data taking. The scaling for each sample was calculated using SHERPA's estimation of the sample's cross section, the efficiency with which generated events met the requirements for generating events, the number of events generated and a k-factor scaling of the cross section. The k-factor is a calculated correction to scale the cross section to the NLO level. The $t\bar{t}$ and $W \to l\nu$ samples have been scaled by measured data/MC ratios detailed in section 4.1.2. The $E_{\mathrm{T}}^{\mathrm{miss}}$ distributions of the background samples are shown in figure 4.1, where the different distributions have been stacked. The $t\bar{t}$, diboson and $Z \to \ell\ell$ distributions were in fact estimated using a number of samples with different final states, which have then been summed. A Monte Carlo estimation of the $Z \to \nu\nu$ signal has also been stacked with the backgrounds to provide a comparison with the $E_{\mathrm{T}}^{\mathrm{miss}}$ distribution measured in the data, which is also shown in the figure. The number of events in each sample passing the selection are given in table 4.2. The proportion of the MC estimation from the different sources is shown in figure 4.2.

The largest component of the MC estimated background comes from the $W \to \tau\nu$ events. These events include at least two neutrinos and therefore have large real $E_{\mathrm{T}}^{\mathrm{miss}}$. Additionally the taus either decay hadronically or into low p_{T} electrons or

Table 4.1: Monte Carlo samples used in the background estimation for the invisible channel.

Sample	Events (10^6)	Estimated luminosity (fb^{-1})
$Z \to ee$	29.8	24.0
$Z \to \mu\mu$	30.0	24.2
$Z \to \nu\nu$	4.9	0.7
$Z \to \tau^+\tau^-$	15.0	12.1
$W \to e\nu$	40.0	3.3
$W \to \mu\nu$	40.0	3.3
$W \to \tau\nu$	9.0	0.6
$t\bar{t} \to ll$	1.8	152.4
$t\bar{t} \to l\tau_l$	0.6	144.3
$t\bar{t} \to \tau_l\tau_l$	0.1	150.4
$t\bar{t} \to lh$	8.8	118.4
$t\bar{t} \to l\tau_h$	1.1	143.9
$t\bar{t} \to \tau_l h$	1.8	137.0
$t\bar{t} \to \tau_l\tau_h$	0.2	147.9
$t\bar{t} \to hh$	5.5	47.5
$t\bar{t} \to h\tau_h$	3.2	133.7
$t\bar{t} \to \tau_h\tau_h$	0.2	145.2
$t \to l(t-chan)$	9.0	315.7
$t \to l(s-chan)$	1.2	660.1
$Wt \to inc(t-chan)$	1.0	44.7
$Wt \to ll(t-chan)$	1.0	425.8
diboson $\to eeqq$	0.2	117.5
diboson $\to e\nu qq$	0.9	93.1
diboson $\to \mu\mu qq$	0.2	118.6
diboson $\to \mu\nu qq$	1.0	104.7
diboson $\to \tau\tau qq$	0.2	117.5
diboson $\to \tau\nu qq$	1.0	104.6
diboson $\to \nu\nu qq$	0.3	54.1

muons. These are more likely to be below the lepton veto p_{T} thresholds. The $W \to e\nu$ background is larger than the $W \to \mu\nu$ background due to the higher p_{T} threshold on the electron veto.

The total estimated MC (including the simulated signal) is approximately 7% larger than the number of events selected in the data sample. This discrepancy is probably due to a combination of the uncertainty on the luminosity of the data sample and also on the estimated cross sections of the unscaled background or the signal MC samples.

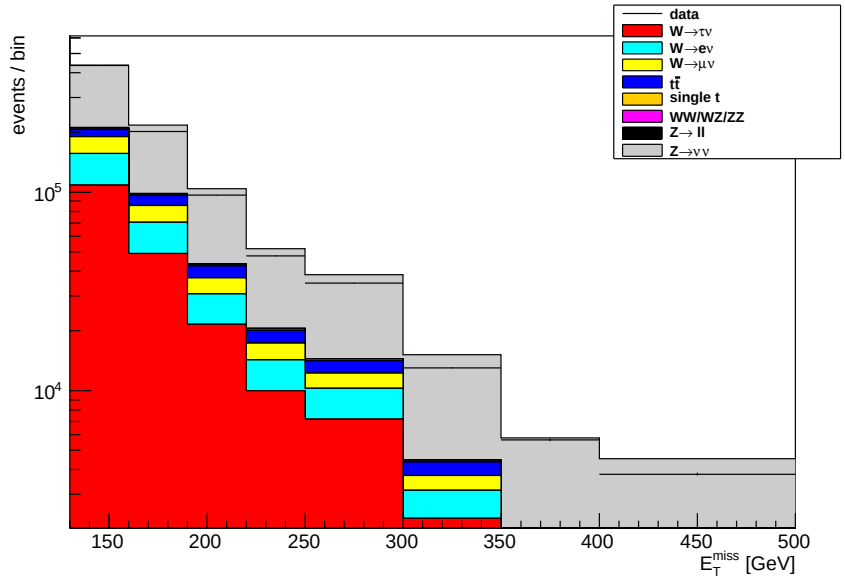


Figure 4.1: Monte Carlo estimated $E_{\mathrm{T}}^{\mathrm{miss}}$ distributions in the invisible channel.

Table 4.2: Comparison between data and Monte Carlo background estimations in the $Z \to$ inv channel.

Sample	Events	% of data
jet + $Z \to$ inv data	840154	
Monte Carlo:		
Sum MC	901963 ± 6744	107.4
$Z \to \nu\nu$	479173 ± 5199	57.0
$W \to \tau\nu$	217780 ± 4045	25.9
$W \to e\nu$	95217 ± 1114	11.3
$W \to \mu\nu$	66515 ± 916	7.9
$t\bar{t}$	33686 ± 73	4.0
$Z \to \ell\ell$	3655 ± 105	0.4
single top	5619 ± 35	0.7
diboson	318 ± 11	0.0

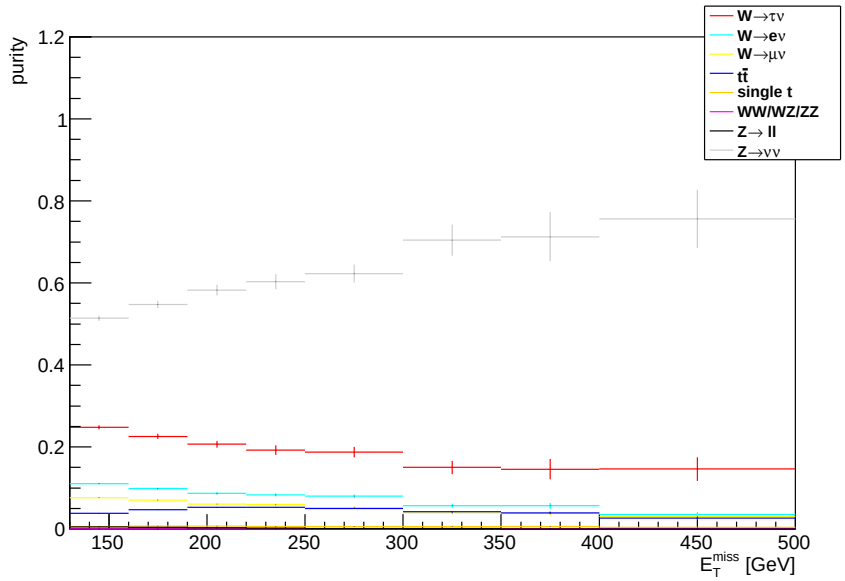


Figure 4.2: Proportion of Monte Carlo estimated backgrounds from different sources as a function of $E_{\mathrm{T}}^{\mathrm{miss}}$ in the invisible channel.

4.1.2 Scaling MC estimations

Some of the MC based background estimations can be improved by using scaling factors derived from the ratio of data to MC simulations. The event selection criteria were changed to select events where the background in question is the dominant signal and where the jet + $Z \to \nu\bar{\nu}$ or jet + $Z \to e^+e^-$ signals are negligible. This procedure is performed for the $t\bar{t}$ and $W \to l\nu$ backgrounds. In the case of the $W \to l\nu$ backgrounds the scaling factor is derived for both $W \to e\nu$ and $W \to \mu\nu$. Since the two scaling factors agree well with each other the average of the two is applied to both those backgrounds and also the $W \to \tau\nu$ background. Using a data/MC scaling removes an uncertainty due to the estimated cross sections of the simulated samples and the luminosity of the data sample.

For the $t\bar{t}$ scaling factor events with a final state electron or muon are used. Events were selected using the jet$+Z \to e^+e^-$ channel selection criteria, but instead of selecting events using two electrons they were selected using an electron and a muon. 'Combined' muons (as defined in chapter 2) were selected with $p_{\mathrm{T}} > 25$ GeV and $|\eta| < 2.4$. The muons were required to be isolated by summing the momentum of tracks in a cone of $\Delta R(\mathrm{trk}, \mu) < 0.2$, and requiring this to be less than one tenth of the momentum of the muon. Electrons were also selected using the same requirement as in the jet + $Z \to e^+e^-$ channel selection. Events were required to have exactly one electron and one muon and they were required to have the same invariant mass, separation and p_{T} requirements as are enforced in the jet$+Z \to e^+e^-$ selection.

This selection is applied to the data and selects a $t\bar{t}$ enriched data sample. From Monte Carlo estimations the only background to the $t\bar{t} \to e\mu$ sample comes from events where a single top quark is produced. Figure 4.3 shows the proportion of the MC estimated events coming from the two different sources. The same selection is applied to the $t\bar{t}$ MC samples. The single top $E^{\mathrm{miss}}_{\mathrm{T,had}}$ distribution is removed from the data distribution. The ratio of the background removed data $E^{\mathrm{miss}}_{\mathrm{T,had}}$ distribution to the MC $t\bar{t}$ distribution is shown in figure 4.4. The ratio is largely independent

of the hadronic recoil, and so a single scaling factor was found as the ratio of the number of events in data and MC passing the $t\bar{t} \to e\mu$ selection. The scale factor applied to the $t\bar{t}$ MC background estimations was 1.13 ± 0.03.

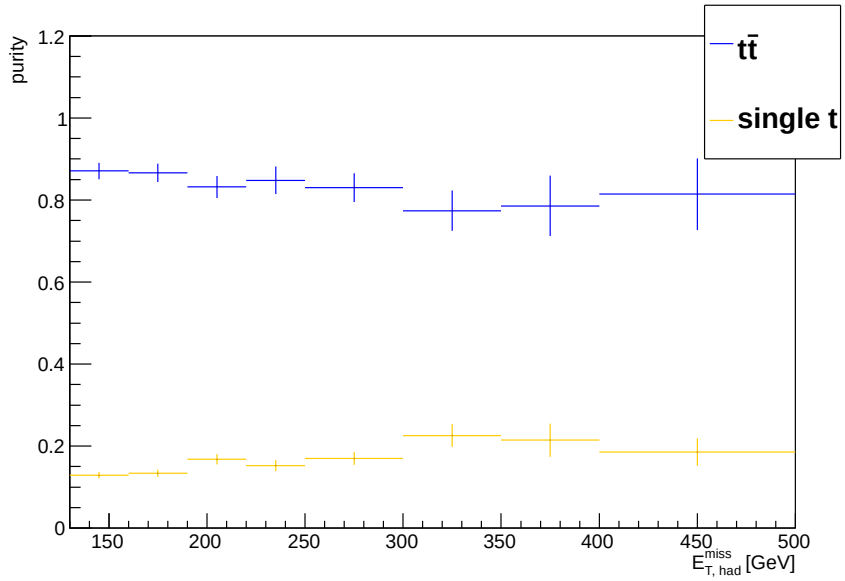


Figure 4.3: Proportion of the MC estimated events passing the $t\bar{t} \to e\mu$ selection coming from $t\bar{t}$ or single top samples as a function of $E^{\text{miss}}_{\text{T,had}}$.

The $W \to l\nu$ scaling factor was calculated using two different selections. In the $W \to e\nu$ selection the $Z \to \nu\nu$ channel selection was modified to select a single electron using the same criteria as in the jet + $Z \to e^+e^-$ channel. The electron's p_{T} was required to be above 25 GeV. The transverse mass was calculated as

$$m_T = \sqrt{2p^e_T E^{\text{miss}}_{\text{T}}(1 - \cos\Delta\phi)}, \tag{4.1}$$

where p^e_{T} is the electron's p_{T} and $\Delta\phi$ is the angular distance between the electron's p_{T} and the $E^{\text{miss}}_{\text{T}}$ in the transverse plane. The transverse mass was required to be over 40 GeV in order to select W events.

The $W \to \mu\nu$ channel selection mirrors that of the $W \to e\nu$ channel, but with a required single muon rather than a single electron. The muon was selected using the same criteria as in the $t\bar{t} \to e\mu$ selection. The requirements on the lepton p_{T} and transverse mass were equivalent to those in the $W \to e\nu$ selection.

The two selection criteria were applied to data and MC samples. In both channels there is a high purity of the relevant $W \to l\nu$ signal of roughly 80%. Additionally there is a $W \to \tau\nu$ contribution in each of the channels. The significant backgrounds in the $W \to l\nu$ events come from $t\bar{t}$, single top and diboson events. The proportion of events coming from the different MC samples are shown in figure 4.5.

Since there are significant backgrounds in both channels their Monte Carlo estimations were removed from the $E_{\mathrm{T}}^{\mathrm{miss}}$ distribution measured in data. The $t\bar{t}$ sample was scaled using the scaling factor given above. The background removed data distributions were then compared to the MC estimated distributions given by the sum of either $W \to e\nu$ or $W \to \mu\nu$ and the $W \to \tau\nu$ $E_{\mathrm{T}}^{\mathrm{miss}}$ distribution. The two ratios are shown in figure 4.6.

The scale factors calculated in both channels agree well. Since the scale factor has a $E_{\mathrm{T}}^{\mathrm{miss}}$ dependence the scale factor was applied to the $W \to l\nu$ background estimations bin by bin.

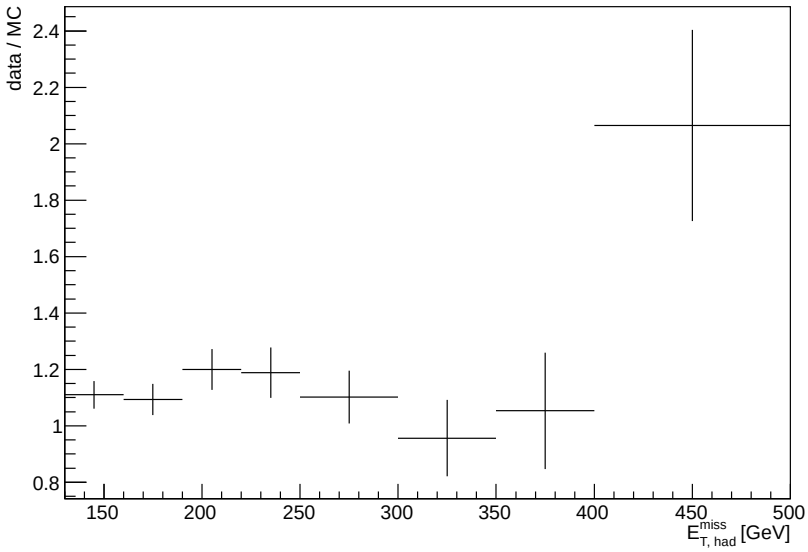


Figure 4.4: Ratio of the hadronic recoil distribution in data and MC events passing the $t\bar{t} \to e\mu$ selection.

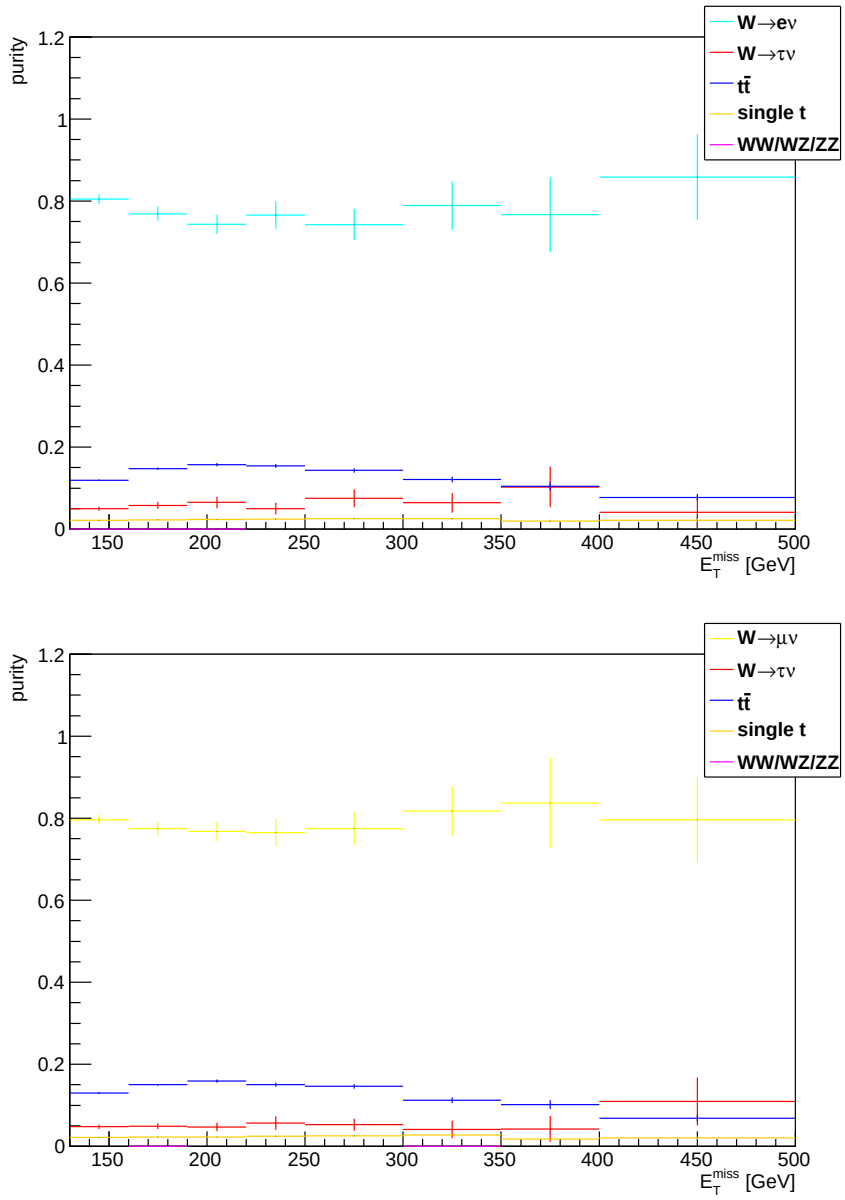


Figure 4.5: Purity of events from the MC simulations passing the $W \to e\nu$ and $W \to \mu\nu$ selection criteria.

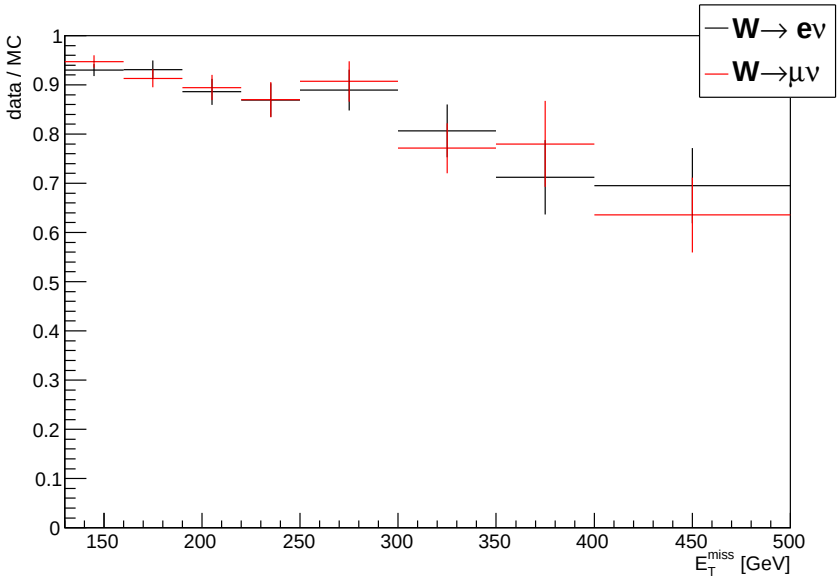


Figure 4.6: The ratios of data and MC $E_{\mathrm{T}}^{\mathrm{miss}}$ distributions in events passing the $W \to e\nu$ or $W \to \mu\nu$ selection criteria.

4.1.3 QCD background estimation

The QCD background to the jet$+Z \rightarrow$ inv channel comes from events where a jet is mismeasured such that fake missing transverse energy is introduced into the event. This could occur either by a jet's p_{T} being reconstructed too low, introducing $E_{\mathrm{T}}^{\mathrm{miss}}$ in the direction of this jet, or reconstructed too high, introducing $E_{\mathrm{T}}^{\mathrm{miss}}$ in the opposite direction. In order to reduce this background the jet$+Z \rightarrow$ inv selection has a veto on any events with a jet with $\Delta\phi(\mathrm{jet}, E_{\mathrm{T}}^{\mathrm{miss}}) < 0.5$. The distribution of $\Delta\phi(\mathrm{jet}, E_{\mathrm{T}}^{\mathrm{miss}})$ for the jet nearest to the $E_{\mathrm{T}}^{\mathrm{miss}}$ is shown in figure 4.7. The distributions are made for the data sample and the $Z \rightarrow \nu\nu$ MC sample after the neutrino channel selection with the $\Delta\phi(\mathrm{jet}, E_{\mathrm{T}}^{\mathrm{miss}})$ criteria relaxed. The two distributions have been scaled to have the same area. The $Z \rightarrow \nu\nu$ sample has a flat $\Delta\phi$ distribution at low values due to the accidental alignment of a jet with the $E_{\mathrm{T}}^{\mathrm{miss}}$. The data sample has a large peak at low $\Delta\phi$ due to QCD (and other) backgrounds where a jet is aligned with the $E_{\mathrm{T}}^{\mathrm{miss}}$. The veto on events with any jet exhibiting $\Delta\phi(\mathrm{jet}, E_{\mathrm{T}}^{\mathrm{miss}}) < 0.5$ therefore removes some $Z \rightarrow \nu\nu$ events, but also removes a large number of background events. The peak at $\Delta\phi \approx \pi$ comes from events where there is a single jet, which is therefore in the opposite direction to the $E_{\mathrm{T}}^{\mathrm{miss}}$.

The selection also requires $E_{\mathrm{T}}^{\mathrm{miss}} > 130$ GeV, which leads to a small QCD background since the probability that mismeasured jets can produce high $E_{\mathrm{T}}^{\mathrm{miss}}$ falls rapidly. In events where a jet's p_{T} is overestimated, the most likely scenario is a jet in the direction opposite to the mismeasured one that is therefore pointing towards the $E_{\mathrm{T}}^{\mathrm{miss}}$ and fails this veto. In the case where the jet's p_{T} is underestimated, the under-reconstructed jet is pointing towards the $E_{\mathrm{T}}^{\mathrm{miss}}$ and also fails this veto. However, if the jet's p_{T} is underestimated so much that it has reconstructed $p_{\mathrm{T}} < 30$ GeV then it will not be counted as a jet in the jet$+Z \rightarrow$ inv selection and will enter as a background. The QCD estimation attempts to quantify the rate at which such events occur.

A QCD enriched data sample is selected from events that pass the jet$+Z \rightarrow$ inv selection with the $\Delta\phi(\mathrm{jet}, E_{\mathrm{T}}^{\mathrm{miss}})$ selection reversed (i.e. requiring at least one jet

pointing towards the $E_{\mathrm{T}}^{\mathrm{miss}}$). This QCD enriched data sample is used to make the QCD background estimation. However, there is a large non-QCD component to this control region, and so the same selection is made on electroweak and top Monte Carlo samples. The samples are split into the bins of $E_{\mathrm{T}}^{\mathrm{miss}}$ used in the analysis. In the QCD control region events are selected with only a single jet pointing towards the $E_{\mathrm{T}}^{\mathrm{miss}}$, and the p_{T} distribution of this 'bad' jet is made. Since the background estimation is based on extrapolation of the 'bad' jet p_{T} below threshold, events with multiple jets pointing towards the $E_{\mathrm{T}}^{\mathrm{miss}}$ would not be selected if only one of the jets was below threshold. The p_{T} distribution of the jet pointing towards the $E_{\mathrm{T}}^{\mathrm{miss}}$ is also made in the MC samples. The MC sample distributions are scaled to the data luminosity and summed. The MC distribution is shown in figure 4.8 for the lowest $E_{\mathrm{T}}^{\mathrm{miss}}$ bin ($130 < E_{\mathrm{T}}^{\mathrm{miss}} < 160$ GeV). As can be seen, the largest contribution to the background in the QCD control region comes from $W \to \tau\nu$. $Z \to \nu\nu$ also forms a significant background. Figure 4.9 compares the shapes of the distributions in the data QCD control region and the MC estimation of the backgrounds in this control region. The electroweak backgrounds have a p_{T} spectrum for the 'bad' jet that is rapidly falling. This contrasts with the p_{T} distribution for the QCD events, which is rising. The shape of the electroweak background in this sample has a strong impact on the QCD background estimation.

This combined MC background distribution is removed from the data distribution and what remains is an estimation of the p_{T} distribution from QCD events. A linear fit is made of the low p_{T} end of this distribution and the integral below the 30 GeV jet threshold (to the point where it reaches 0 events) is considered the estimation of the number of events where the jet p_{T} was mismeasured such that its p_{T} fell below threshold. Figure 4.10 shows this distribution, with the linear fit, in the lowest $E_{\mathrm{T}}^{\mathrm{miss}}$ bin. In this bin there is an estimated 2639 QCD events. This is approximately 0.6% of the events in the lowest bin of the $Z \to \nu\nu$ selection.

A good estimation is possible in the second $160 < E_{\mathrm{T}}^{\mathrm{miss}} < 190$ GeV also. In higher $E_{\mathrm{T}}^{\mathrm{miss}}$ bins, however, the estimation becomes difficult. The MC background

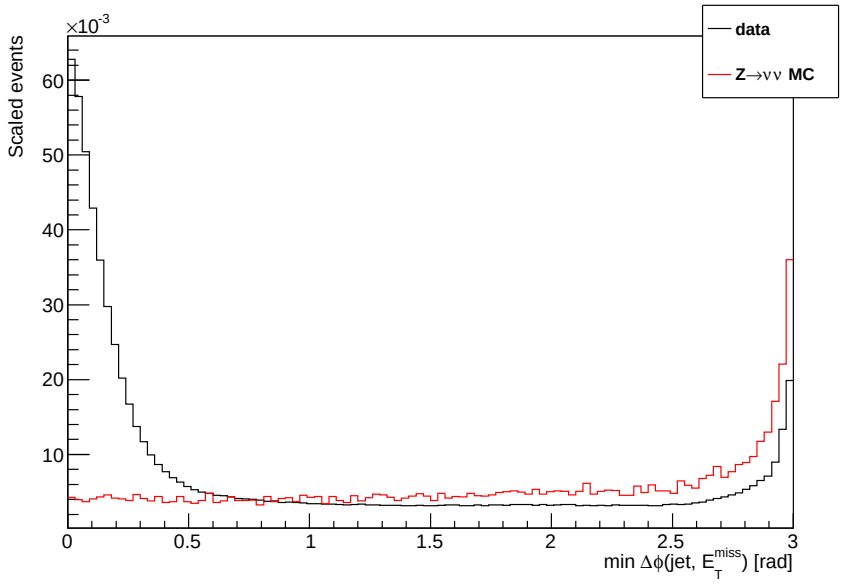


Figure 4.7: $\Delta\phi(\text{jet}, E_{\text{T}}^{\text{miss}})$ distribution for the jet closest to the $E_{\text{T}}^{\text{miss}}$ in the data and $Z \to \nu\nu$ MC samples with the $\Delta\phi$ veto relaxed.

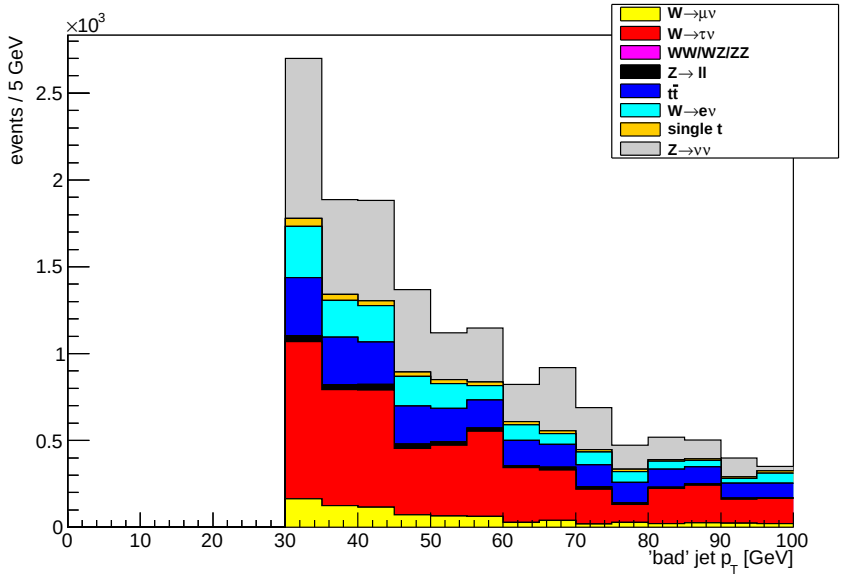


Figure 4.8: p_{T} distribution of the jet pointing towards the $E_{\text{T}}^{\text{miss}}$ in the MC background estimations in the lowest $E_{\text{T}}^{\text{miss}}$ bin.

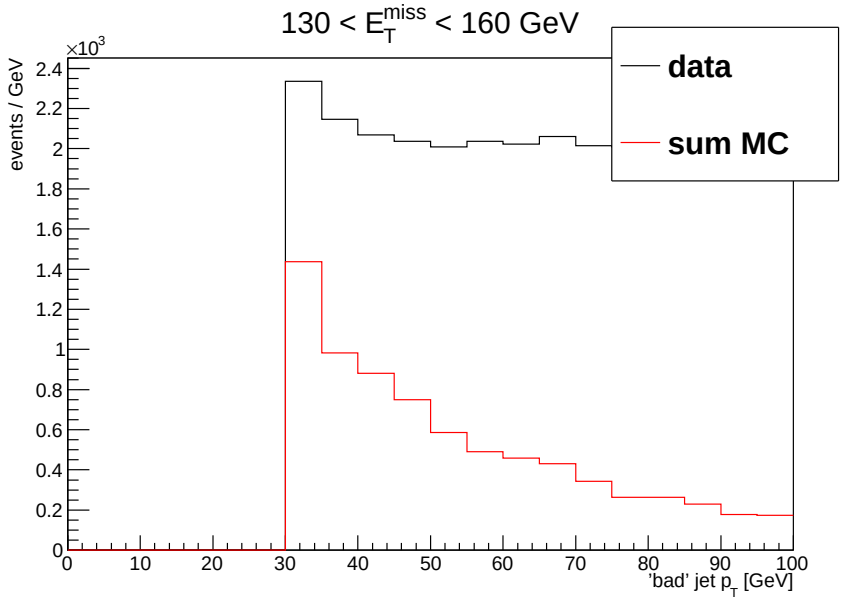


Figure 4.9: p_{T} distribution of the jet pointing towards the $E_{\mathrm{T}}^{\mathrm{miss}}$ in the QCD control region in data and MC background estimations in the lowest $E_{\mathrm{T}}^{\mathrm{miss}}$ bin.

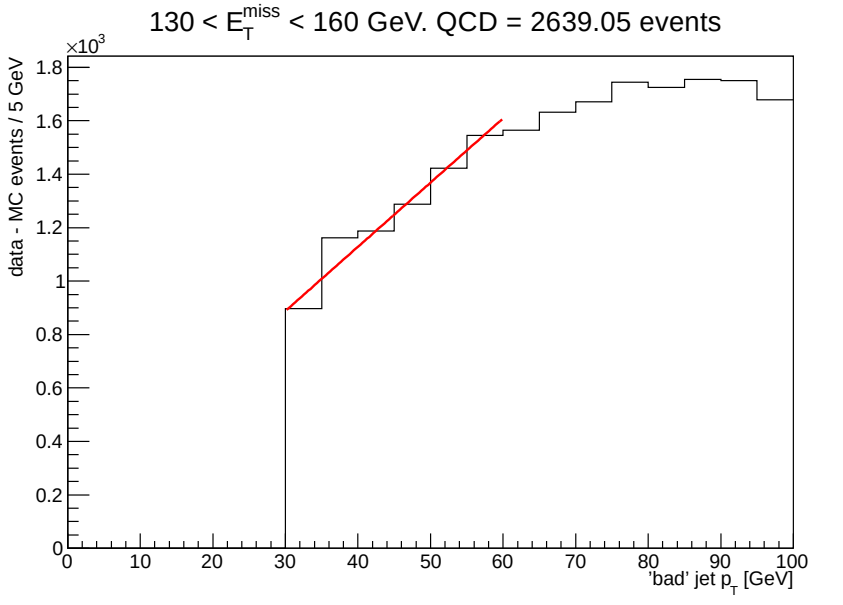


Figure 4.10: p_{T} distribution of the jet pointing towards the $E_{\mathrm{T}}^{\mathrm{miss}}$ in the QCD control region with the MC background estimations removed, in the lowest $E_{\mathrm{T}}^{\mathrm{miss}}$ bin.

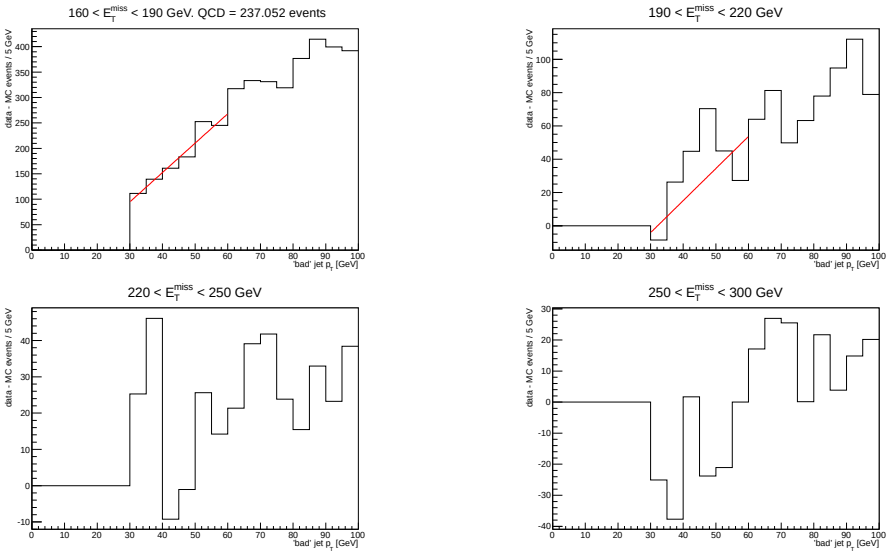


Figure 4.11: p_{T} distribution of the jet pointing towards the $E_{\mathrm{T}}^{\mathrm{miss}}$ in the QCD control region with the MC background estimations removed, in higher $E_{\mathrm{T}}^{\mathrm{miss}}$ bin.

estimations become a similar magnitude to the control region. There are only low statistics available in the MC samples, such that statistical fluctuations in their shape impact the fit of the bad jet p_{T}. Figure 4.11 shows the attempted fits in some of the higher $E_{\mathrm{T}}^{\mathrm{miss}}$ bins. However, it is thought that the QCD backgrounds become negligible at higher $E_{\mathrm{T}}^{\mathrm{miss}}$, and so estimations in these bins are not required. In figure 4.12, where the $130 < E_{\mathrm{T}}^{\mathrm{miss}} < 170$ GeV region has been split into more bins, the estimation quickly falls with rising $E_{\mathrm{T}}^{\mathrm{miss}}$, and so the QCD estimation for the bins with $E_{\mathrm{T}}^{\mathrm{miss}} > 190$ GeV is assumed to be negligible. Table 4.3 shows how the fraction of the data events estimated to come from the QCD background falls in the different bins of $E_{\mathrm{T}}^{\mathrm{miss}}$. While the whole 130 - 160 GeV bin has a QCD estimation of 0.6%, the first 10 GeVof this bin has an estimated 1.1% QCD, falling to 0.2% for the highest 10 GeV of the bin.

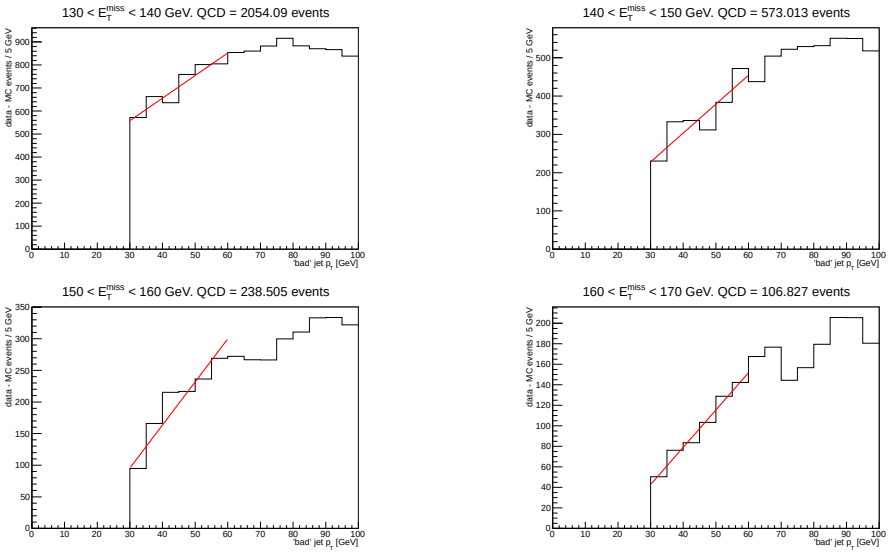


Figure 4.12: p_{T} distribution of the jet pointing towards the $E_{\mathrm{T}}^{\mathrm{miss}}$ in the QCD control region with the MC background estimations removed, in the sections of the lowest $E_{\mathrm{T}}^{\mathrm{miss}}$ bin.

Table 4.3: Size of estimated QCD background in different $E_{\mathrm{T}}^{\mathrm{miss}}$ bins.

$E_{\mathrm{T}}^{\mathrm{miss}}$	estimated QCD events	% of data
130 - 160	2639	0.6
130 - 140	2054	1.1
140 - 150	573	0.4
150 - 160	239	0.2
160 - 190	237	0.1
160 - 170	107	0.1
170 - 180	83	0.1
180 - 190	40	0.1

4.2 Background estimations in the jet + $Z \to e^+e^-$ channel

The jet + $Z \to e^+e^-$ channel has much smaller background contamination than the $Z \to \nu\nu$ channel. The requirement of identifying two good quality electrons that are consistent with a Z boson decay makes it harder for other events to fake the signal. The dominant backgrounds come from $t\bar{t}$ events and single top events with leptonic decays and also events with a Z boson which decays to electrons with an additional weak boson. Additionally a small background is possible from QCD events, where two hadronic jets are misidentified as electrons.

4.2.1 Monte Carlo background estimations

MC based background estimations were also performed in the jet + $Z \to e^+e^-$ channel. The only significant backgrounds come from $t\bar{t}$ events, single top events and from events with two weak bosons. The estimation used the same samples used in the $Z \to \nu\nu$ channel. The events were again weighted to take into account the pileup conditions during the 2012 data taking periods. The electrons' energy and the muons' momenta were corrected to better match the distributions seen in data. Additionally, the events were weighted so that the efficiency of identifying the two electrons from the Z decay is scaled to match the measured efficiency in the data. The $t\bar{t}$ and $W \to l\nu$ events were scaled by the factors given in section 4.1.2. Figure 4.13 shows a comparison of the hadronic recoil distributions between the MC backgrounds, summed with a MC estimate of the jet + $Z \to e^+e^-$ signal, compared to the distribution measured in data. The numbers of events in the significant samples are shown in table 4.4. The total MC estimation is about 1% larger than the number of events in the data sample.

Table 4.4: Comparison between data and Monte Carlo background estimations in the jet + $Z \to e^+e^-$ channel.

Sample	Events	% of data
jet + $Z \to e^+e^-$ data	36196	
Monte Carlo:		
Sum MC	36370 ± 265	100.5
$Z \to ee$	35224 ± 258	97.3
$t\bar{t}$	833 ± 11	2.6
single top	151 ± 6	0.4
diboson	18 ± 2	0.1
$W \to l\nu$	101 ± 50	0.2
$Z \to \tau^+\tau^-$	42 ± 12	0.1

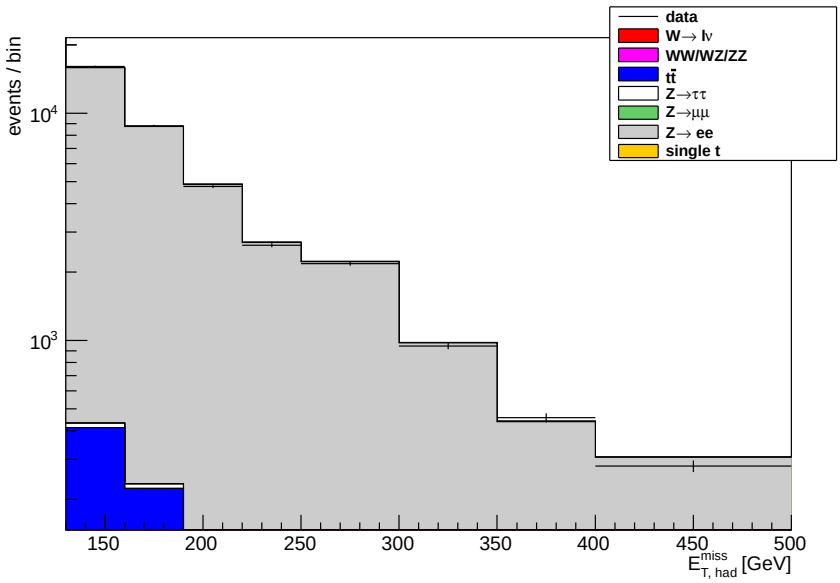


Figure 4.13: $E^{\text{miss}}_{\text{T,had}}$ distribution in Monte Carlo estimated backgrounds to the electron channel.

4.2.2 QCD background estimation

The QCD background in the jet + $Z \to e^+e^-$ channel comes from events where two jets have been misidentified as electrons and the pair identified as a Z decay. The background is estimated by selecting a QCD enriched control region. This is done by first selecting electrons that pass the 'loose' identification requirements but fail the 'medium' requirements used in the jet + $Z \to e^+e^-$ channel selection explained in chapter 2. Using these electrons, which are often hadronic jets faking electrons, the jet + $Z \to e^+e^-$ channel selection is performed without the invariant mass cut. This produces a QCD enriched control sample. The invariant mass distribution of the events in the QCD control region is shown in figure 4.14. However there is still a jet + $Z \to e^+e^-$ contribution to this sample as evidenced by the fact that there is a small Z peak in the invariant mass distribution. The sample is further enriched in QCD by requiring that the two identified 'electrons' have the same charge. No Z peak is visible in this sample following this requirement. The QCD control region's invariant mass distribution can be compared to the invariant mass distribution in the MC jet + $Z \to e^+e^-$ sample, also shown in figure 4.14. This MC sample is selected using the jet + $Z \to e^+e^-$ channel selection criteria with the invariant mass requirement relaxed.

The m_{ee} distribution in the MC estimated $t\bar{t}$, single top and diboson backgrounds to the jet + $Z \to e^+e^-$ channel are also found over an extended m_{ee} range. The $t\bar{t}$ events are scaled to the data luminosity using the data driven ratio found in section 4.1.2. The diboson sample is simply scaled using the MC estimate of the luminosity, as in section 4.2.1. Data events are selected using the jet + $Z \to e^+e^-$ channel criteria with the invariant mass requirement relaxed. The QCD control region template, the jet + $Z \to e^+e^-$ MC template and the m_{ee} distribution from the $t\bar{t}$ and diboson MC background estimations were fitted to the jet + $Z \to e^+e^-$ channel's data distribution. The fit was performed in the signal and high m_{ee} regions ($66 < m_{ee} < 166$ GeV). The $t\bar{t}$ and diboson (WW, WZ or ZZ) contributions are fixed based upon their previous estimation while scaling factors for the jet + $Z \to$

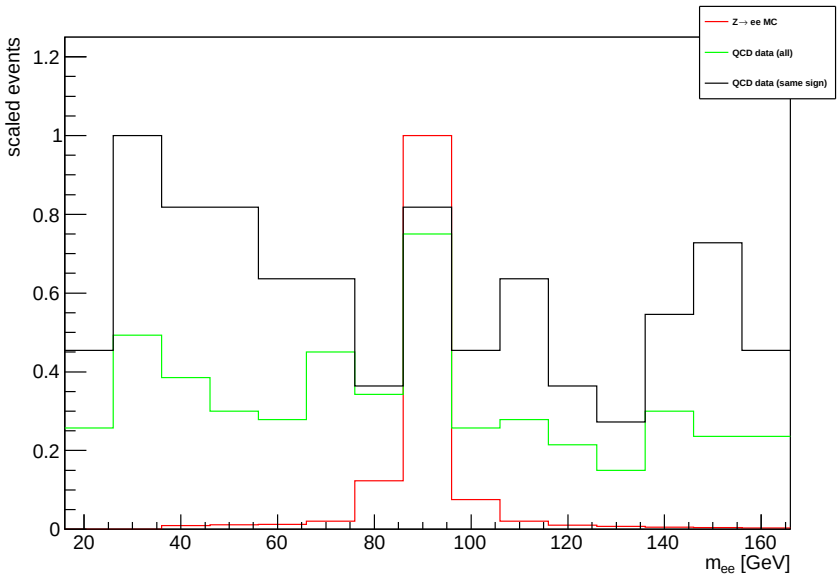


Figure 4.14: Invariant mass distributions in the jet + $Z \to e^+e^-$ MC sample and the QCD control region data sample, with and without a same sign 'electron' requirement.

e^+e^- and QCD templates were determined by the fit. The result of the fitting procedure is shown in figure 4.15. Using this fit the estimated number of QCD events passing the $66 < m_{ee} < 116$ GeV requirement was found to be 119, which is 0.33% of the events. The templates were fit with a $\chi^2/\text{NDF} = 3.7$. In order to estimate the $E^{\text{miss}}_{\text{T,had}}$ distribution of the 102 QCD events, the $E^{\text{miss}}_{\text{T,had}}$ distribution of the events contained in the QCD enriched sample was scaled to the correct number. The QCD estimation is shown in figure 4.16.

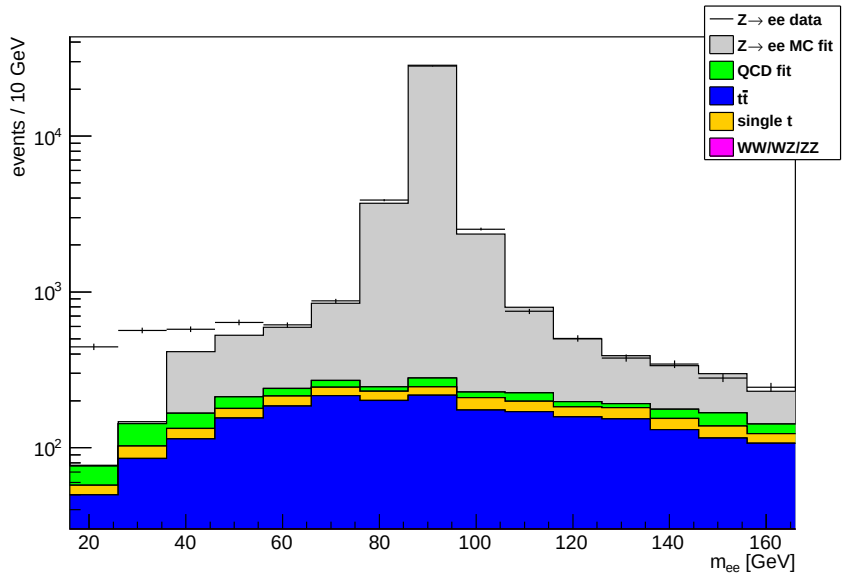


Figure 4.15: Result of fitting QCD and jet + $Z \to e^+e^-$ m_{ee} templates to the m_{ee} distribution of events passing the jet + $Z \to e^+e^-$ channel selection, where the scale of the $Z \to ee$ MC and QCD template distributions has been set by the fitting procedure.

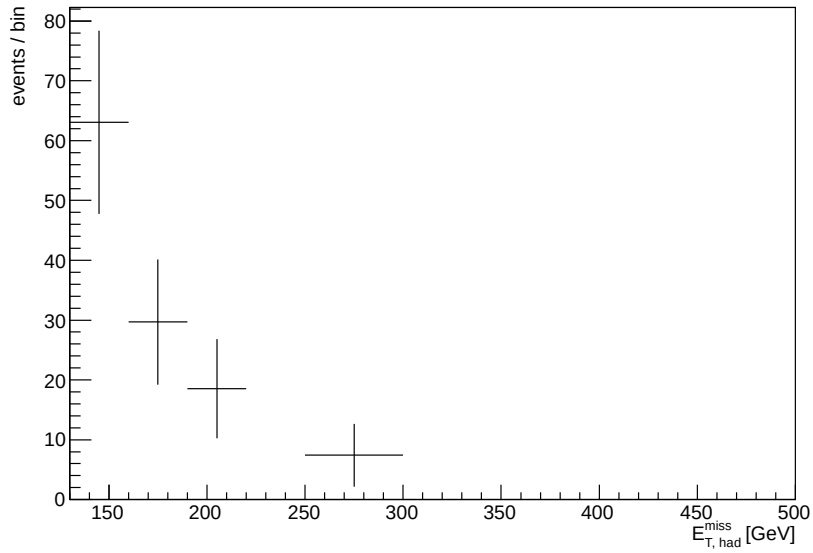


Figure 4.16: $E^{\mathrm{miss}}_{\mathrm{T,had}}$ distribution of estimated QCD background to the jet+$Z \to e^+e^-$ channel.

4.3 Background removed $E_{\mathrm{T}}^{\mathrm{miss}}$ and $E_{\mathrm{T,had}}^{\mathrm{miss}}$ distributions

The full background estimations are given in table 4.5 and table 4.6 for the invisible and electron channels respectively. The sum of all estimated backgrounds was removed from both the $Z \to \nu\nu$ and jet + $Z \to e^+e^-$ channel data $E_{\mathrm{T}}^{\mathrm{miss}}$ or $E_{\mathrm{T,had}}^{\mathrm{miss}}$ distributions. These are shown in figure 4.17. Figure 4.18 shows the ratio of the background removed $E_{\mathrm{T}}^{\mathrm{miss}}$ and $E_{\mathrm{T,had}}^{\mathrm{miss}}$ distributions. The measured ratio falls from approximately 15 to approximately 9 as the $E_{\mathrm{T}}^{\mathrm{miss}}$ or $E_{\mathrm{T,had}}^{\mathrm{miss}}$ increases from 130 GeV to 500 GeV. In chapter 5 a number of corrections for the measured ratio are estimated that convert this measured ratio into a measurement of the invisible width of the Z boson.

Table 4.5: Comparison between data and full background estimations in the $Z \to$ inv channel.

Sample	Events	% of data
jet + $Z \to$ inv data	840154	
Backgrounds:		
Sum of backgrounds	399882 ± 5102	47.6
$W \to \tau\nu$	200294 ± 4645	23.8
$W \to e\nu$	87693 ± 1496	10.4
$W \to \mu\nu$	61247 ± 1151	7.3
$t\bar{t}$	38180 ± 934	4.5
$Z \to \ell\ell$	3655 ± 105	0.4
single top	5619 ± 35	0.7
QCD	2876 ± 54	0.3
diboson	318 ± 11	0.0

Some of the distributions shown at the end of section 3.6 were remade following a background subtraction. This subtraction did not include the QCD backgrounds, where the small number of events are expected to have a small impact and the estimation methods could not simply be converted to estimations in the desired variables. The ϕ distribution of the $E_{\mathrm{T}}^{\mathrm{miss}}$ or $E_{\mathrm{T,had}}^{\mathrm{miss}}$, shown in figure 4.19, is again flat. The leading jet p_{T} distribution now exhibits a slightly larger shape difference between the invisible and electron channels, as shown in figure 4.20, as does the

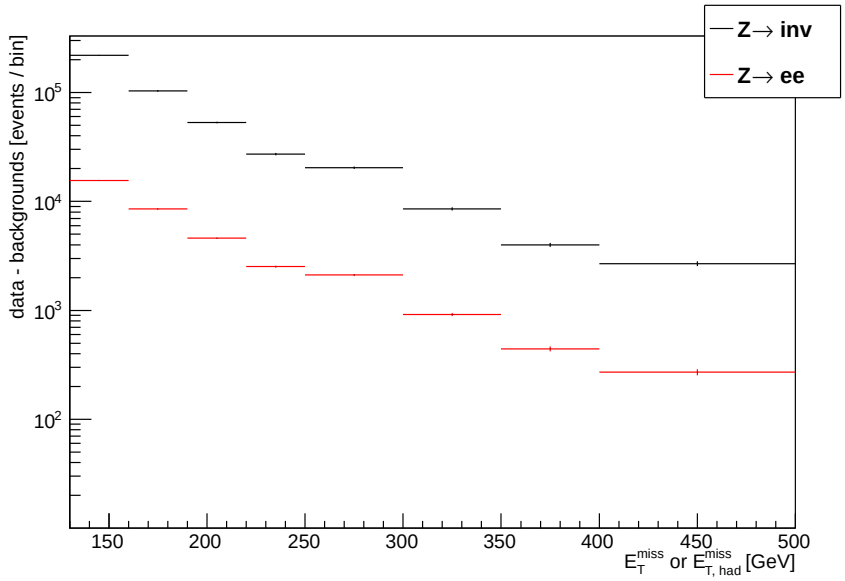


Figure 4.17: Distribution of the $E_{\mathrm{T}}^{\mathrm{miss}}$ or $E_{\mathrm{T,had}}^{\mathrm{miss}}$ measured in the data samples after the subtraction of the background estimations.

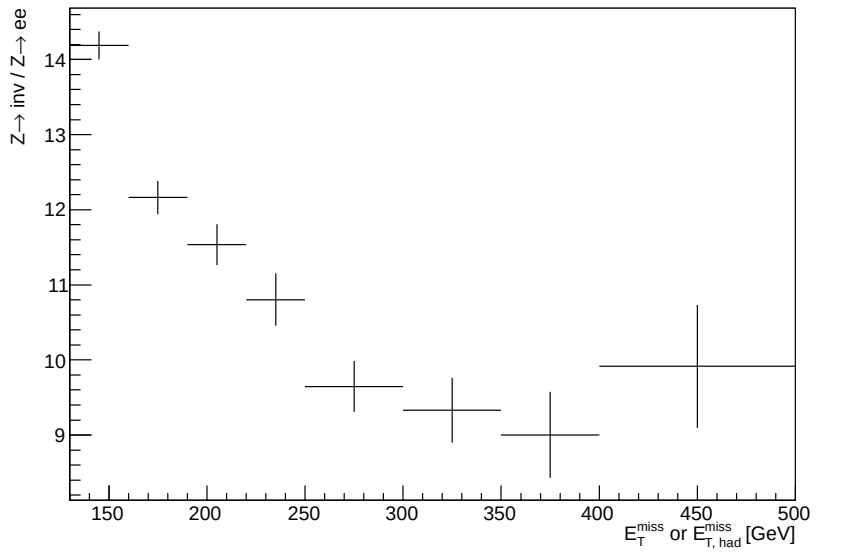


Figure 4.18: Ratio of the (background removed) $E_{\mathrm{T}}^{\mathrm{miss}}$ / $E_{\mathrm{T,had}}^{\mathrm{miss}}$ distributions measured in data.

Table 4.6: Comparison between data and full background estimations in the jet + $Z \to e^+e^-$ channel.

Sample	Events	% of data
jet + $Z \to e^+e^-$ data	36196	
Monte Carlo:		
Sum of backgrounds	1264 ± 265	3.5
$t\bar{t}$	834 ± 26	2.3
single top	151 ± 6	0.4
diboson	18 ± 2	0.0
QCD	119 ± 11	0.3
$W \to l\nu$	101 ± 50	0.3
$Z \to \tau^+\tau^-$	42 ± 12	0.1

distribution of the number of jet shown in figure 4.21. The invisible channel now has a lower number of jets than the electron channel since many of the background sources typically contribute additional jets (for example $W \to l\nu$ events with a forward electron that is not correctly identified but still reconstructed as a jet). The leading jet η and ϕ distributions, shown in figure 4.22 and figure 4.23, are similar to their previous versions.

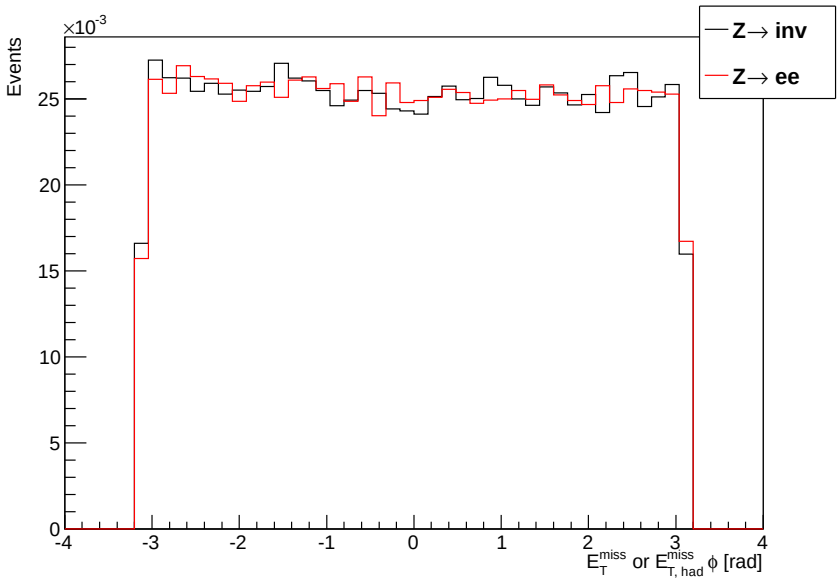


Figure 4.19: Hadronic recoil and missing transverse energy ϕ distributions in events passing the electron and invisible channel selections after background subtraction.

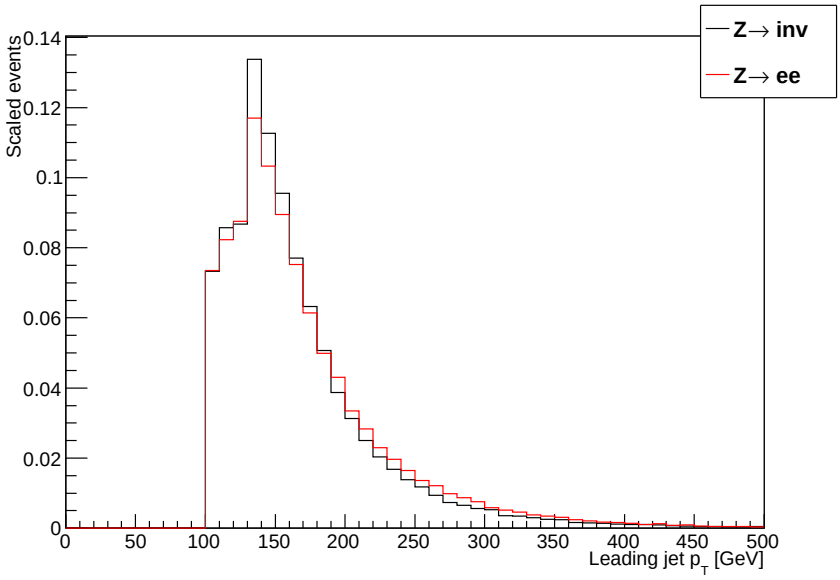


Figure 4.20: Leading jet p_{T} distribution in events passing the electron and invisible channel selections after background subtraction.

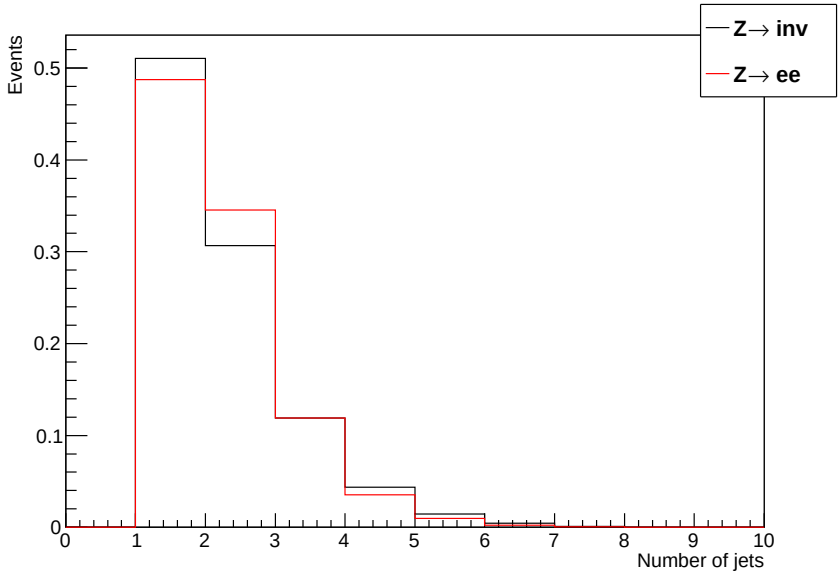


Figure 4.21: The number of jets in events passing the jet + $Z \to$ inv and jet + $Z \to$ e^+e^- selections after background subtraction.

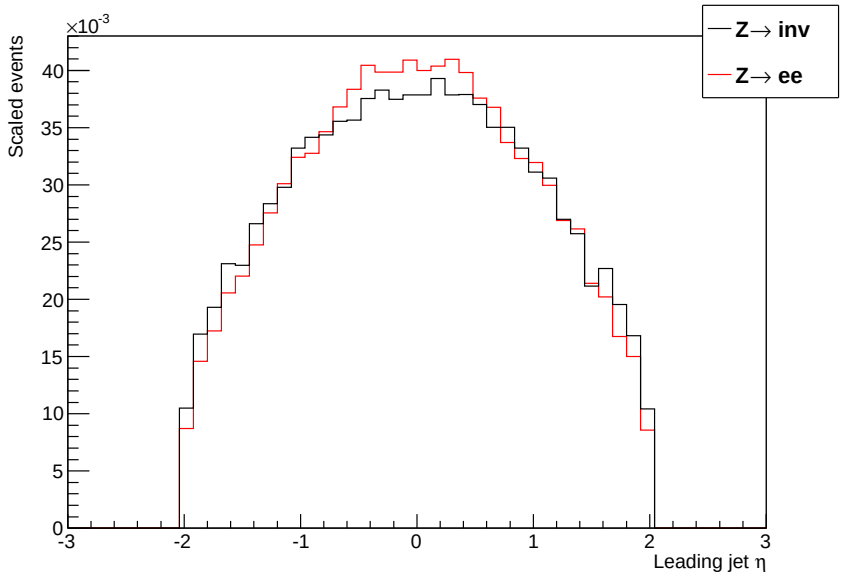


Figure 4.22: Leading jet η distribution in events passing the electron and invisible channel selections after background subtraction.

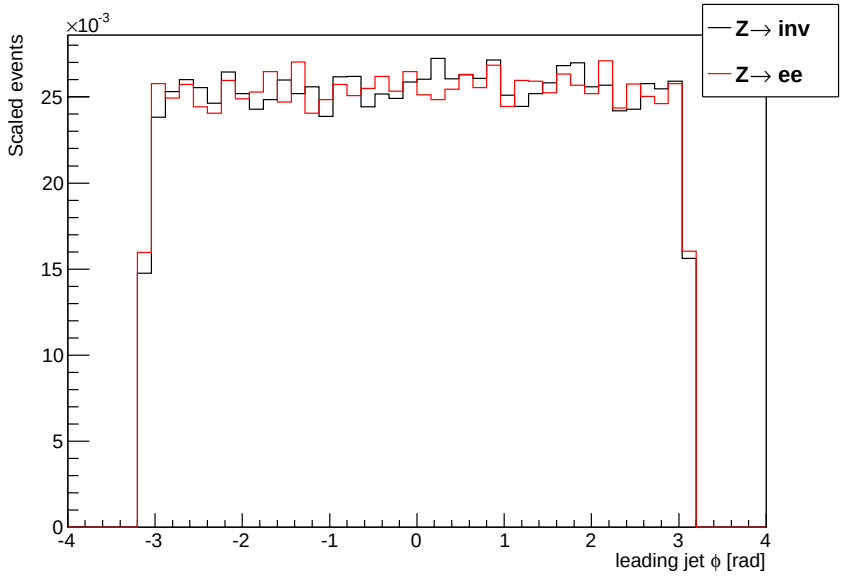


Figure 4.23: Leading jet ϕ distribution in events passing the electron and invisible channel selections after background subtraction.

Chapter 5

Corrections to the measured ratio

Whilst the measurement design, explained in section 1.3, minimises the differences between the two channels, a number of corrections need to be made for the remaining differences that cannot be avoided. Firstly, background estimations were made in the previous section and removed from the measured $E_{\mathrm{T}}^{\mathrm{miss}}$ and $E_{\mathrm{T,had}}^{\mathrm{miss}}$ distributions. In this section a number of corrections are explained. In section 5.1 comparisons of the Z boson's p_{T} distribution in data and Monte Carlo are made and the $E_{\mathrm{T}}^{\mathrm{miss}}$ and $E_{\mathrm{T,had}}^{\mathrm{miss}}$ resolutions are investigated. The first correction is calculated in section 5.2 to take into account differences in trigger efficiencies between the $Z \to \nu\nu$ and $Z \to ee$ channels. Then, in section 5.3, a correction is made to account for the reconstruction of electrons, and the fact that the electron resolution forms a small part of the Z boson's p_{T} resolution. In section 5.4 a correction is made for any difference in the impact of the $E_{\mathrm{T}}^{\mathrm{miss}}$ resolution on the Z boson's p_{T} between the two channels, as well as any difference introduced by the background rejecting selection criteria. Then a correction is made, in section 5.5, to account for the fact that while neutrinos are inferred in a full phase space, the electrons can only be detected within the detector's acceptance. Finally, in section 5.6, a correction is made since the $Z \to \nu\nu$ channel is a pure Z interaction, whereas the $Z \to ee$ channel is a Z/γ^* interaction where a di-electron invariant mass cut around the Z peak is used. With all the above corrections made, the invisible width and the differential cross section ratio are extracted from the measured ratios in section 5.7. Each of the corrections

has been calculated as either a constant value, or a function of the Z boson's p_{T} such that the measurement is extracted as a product of the ratio measured in the data and each of the corrections. In this section only statistical uncertainties will be considered. Systematic uncertainties on the measurement will be evaluated in chapter 6.

Some terminology is used in this section to refer to some precise meanings in a concise way. Some terms were previously defined in chapter 3, others will be defined in the following sections of this chapter. For reference, table 5.1 gives a summary of the definitions of these terms.

Table 5.1: Summary of the definitions of terms used in the correction.

reco $E_{\mathrm{T}}^{\mathrm{miss}}$	Reconstructed `MetRefFinal`
reco $E_{\mathrm{T,had}}^{\mathrm{miss}}$	Reconstructed hadronic recoil, the vector sum of reco $E_{\mathrm{T}}^{\mathrm{miss}}$ and the reco electrons identified as Z decay products
hybrid $E_{\mathrm{T,had}}^{\mathrm{miss}}$	The vector sum of the reco $E_{\mathrm{T}}^{\mathrm{miss}}$ and the truth (dressed) electrons
truth Z	4-vector sum of the born leptons from the hard scattering
truth Z boson's p_{T}	p_{T} of the truth Z
reco electrons	A number of selection criteria on the reconstructed electrons
truth fiducial electrons	The same criteria as above required of the truth (dressed) electrons
truth full phase space electrons	An invariant mass cut on the truth electrons
background cuts	A number of selection criteria designed to remove non $Z \to ee$ or $Z \to \nu\nu$ events
`AntiKt4LCTopo` jets	Jets reconstructed as explained in [17]
reco jets	`AntiKt4LCTopo` jets, with the leading jet required to be central and high p_{T}
truth jets	Jets reconstructed from simulated final state visible particles, with the same requirements as above
pileup reweighting	The MC events are reweighted to have the same pileup experienced over the year of data taking
MC event weighting	The SHERPA samples are reweighted by a factor estimated by SHERPA
dressed matrix element electrons	The electrons created in the hard interaction are identified. The final state electrons corresponding to these electrons are found. They are dressed by adding the 4-momentum of final state photons with $\Delta R(e, \gamma) < 0.1$
overlap reduction	Jets near Z decay electrons (within $\Delta R(\mathrm{jet}, e) < 0.2$) are identified. The jets have the 4-momentum reduced by the jet energy scaled 4-momentum of the nearby electron.

5.1 Z boson's p_{T} distributions and resolutions

A number of the corrections have been calculated using SHERPA jet+$Z \to e^+e^-$ and jet + $Z \to \nu\bar{\nu}$ samples. The SHERPA generator estimates the cross section for the samples, as well as assigning relative weights to the generated events. During each LHC run a number of proton bunches are injected into the accelerator, which then cycle around the LHC ring and collide at the interaction points. The same proton bunches are kept in the collider for each run, which spans a number of hours. During each run the proton collisions lead to beam losses and so the collision rate drops with time over the run. The term 'pileup' is used to refer to the number of collisions that are concurrently detected. As the protons are lost over a run the instantaneous luminosity falls and the pileup reduces as fewer collisions occur. Additionally, over the year of data taking, the instantaneous luminosity the accelerator was capable of delivering changed, as did the timing profile of the bunches injected into the accelerator. The pileup conditions therefore changed considerably over both the long and short term. Since the detector performance is dependent upon the pileup conditions the Monte Carlo samples have been reweighted, using an official ATLAS tool, so that they match the conditions experienced in the detector over the year's data taking. The SHERPA event weights, and the pileup reweighting have been applied to the SHERPA samples used in the corrections.

The Z boson's p_{T} distributions in data and MC samples have been compared. This has been done by selecting events passing the $Z \to ee$ channel selection in both data and MC. The Z in each event is constructed as the 4-vector sum of the two reconstructed electrons. The p_{T} of the Z bosons in data and MC are compared in figure 5.1. The MC samples have been scaled to represent the full 2012 data sample. Figure 5.2 shows the ratio of the MC spectrum to the data one. At high Zp_{T} the MC models the shape of the data spectrum well, with a small scaling offset. At low Z boson's p_{T}, where there are few MC events, there is a large discrepancy due to a contribution from background events on top of the small number of $Z \to ee$ events. Evidence for the low Z boson's p_{T} region being background dominated can be seen

in figure 5.3, where the invariant mass distribution of the two electrons is shown in different segments of Z boson's p_{T}. At high p_{T} the data has a clear Z peak in the invariant mass distribution which closely matches the $Z \to ee$ MC shape. However in the low region more events are seen outside the Z peak, indicating that there is also a contribution from non Z boson events. No event weighting to reshape the Zp_{T} spectrum is required since the shape is well modelled in the MC simulation.

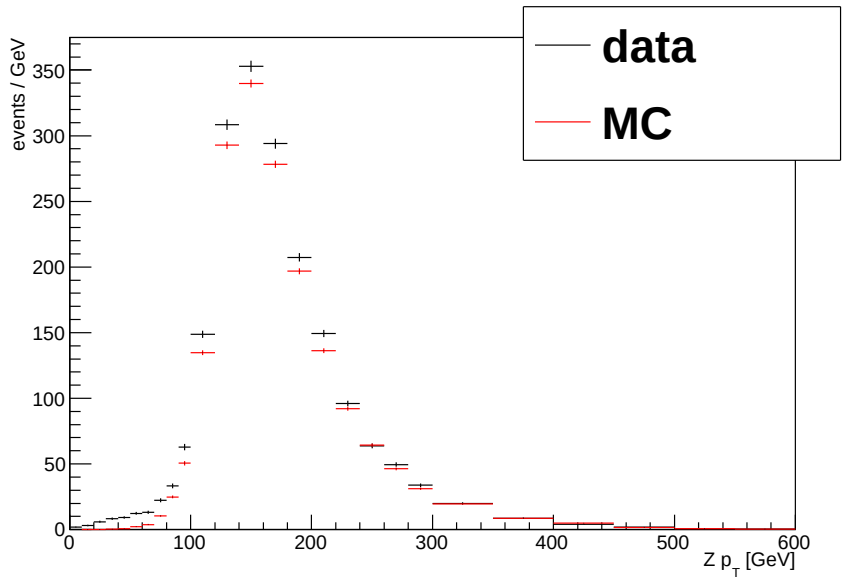


Figure 5.1: Data-MC comparison of Z boson's p_{T} distribution in the SHERPA $Z \to ee$ channel.

The resolution with which $E_{\mathrm{T}}^{\mathrm{miss}}$ and $E_{\mathrm{T,had}}^{\mathrm{miss}}$ model the Z boson's p_{T} has been found. Events in the $Z \to \nu\nu$ sample were found that pass the same jet requirement as in the data selection. The truth Z was constructed by the 4-momentum sum of the two neutrinos from the Z decay in the Monte Carlo truth event record. For each selected event the truth Z boson's p_{T} and direction, the reconstructed $E_{\mathrm{T}}^{\mathrm{miss}}$ and its direction and the event weight were found.

Similarly, events were selected from the jet$+Z \to e^+e^-$ MC sample which passed the electron selection criteria as well as the leading jet criteria. As in the data event selection an electron-jet overlap reduction was performed. The reconstructed $E_{\mathrm{T,had}}^{\mathrm{miss}}$ was calculated and the truth Z was constructed in the same way as the $Z \to \nu\nu$ channel, although with the 'born' electrons. The born electrons are the simulated

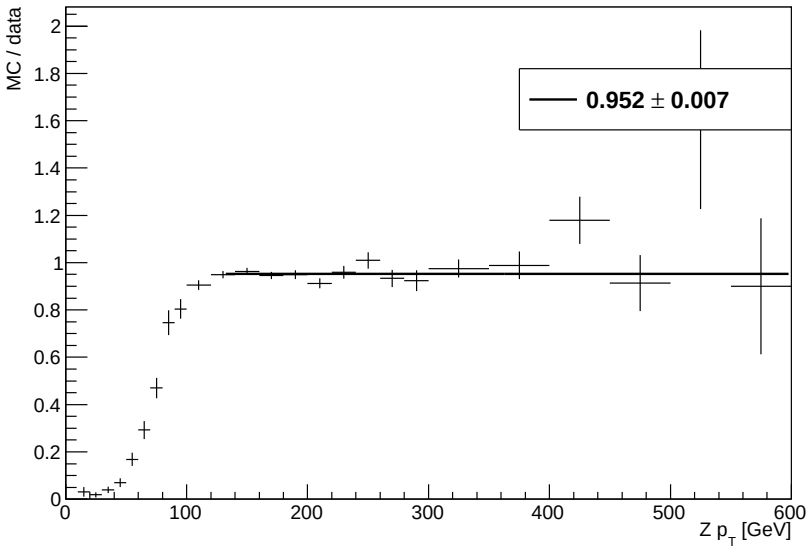


Figure 5.2: Ratio of data and SHERPA MC Z boson's p_{T} distributions.

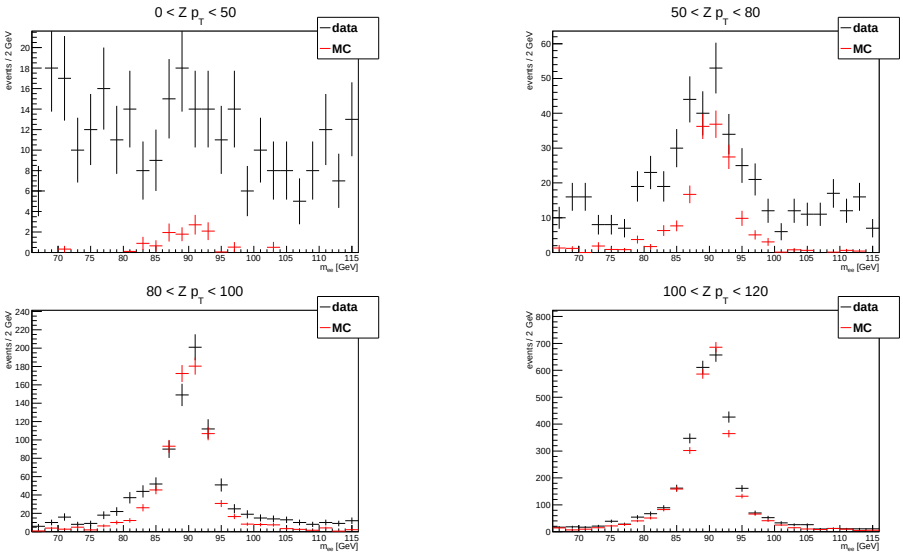
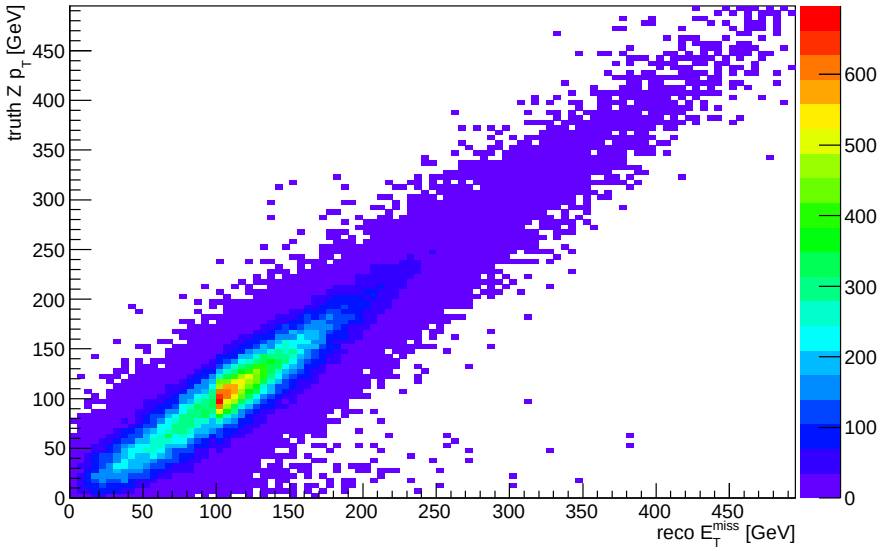


Figure 5.3: Invariant mass distributions in different bins of Zp_{T}.

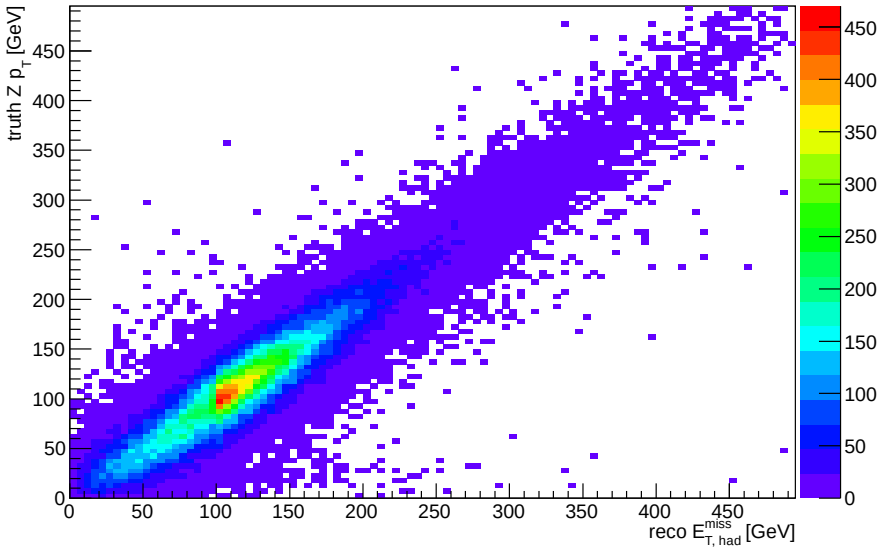
particles coming from the initial Z decay, before any radiative effects are modelled. These were used to show the worst case scenario for the Z p_{T} resolution. The $E_{\mathrm{T,had}}^{\mathrm{miss}}$ and its direction, the Z p_{T} and its direction and the event weight were found for all selected events. The reconstructed $E_{\mathrm{T}}^{\mathrm{miss}}$ and $E_{\mathrm{T,had}}^{\mathrm{miss}}$ were compared to the truth Z boson's p_{T} on an event by event basis. Figure 5.4 shows a comparison of the $E_{\mathrm{T}}^{\mathrm{miss}}$ with the Z boson's p_{T} and also the $E_{\mathrm{T,had}}^{\mathrm{miss}}$ with the Z boson's p_{T}.

A profile of both the $E_{\mathrm{T}}^{\mathrm{miss}}$ and the $E_{\mathrm{T,had}}^{\mathrm{miss}}$ was found for bins of truth Z boson's p_{T}. Additionally profiles were found for the $E_{\mathrm{T}}^{\mathrm{miss}}$ and $E_{\mathrm{T,had}}^{\mathrm{miss}}$ components parallel and perpendicular to the Z boson's p_{T}. In each bin the resolution of the $E_{\mathrm{T}}^{\mathrm{miss}}$ or $E_{\mathrm{T,had}}^{\mathrm{miss}}$ was found as the RMS of the profile in that bin. Figure 5.5 shows the resolution of both the $E_{\mathrm{T}}^{\mathrm{miss}}$ and $E_{\mathrm{T,had}}^{\mathrm{miss}}$ and figure 5.6 shows the same in parallel and perpendicular components. As can be seen in figure 5.5, the $E_{\mathrm{T}}^{\mathrm{miss}}$ resolution is the dominant effect in both channels, with the $E_{\mathrm{T,had}}^{\mathrm{miss}}$ resolution being slightly larger due to the additional electron resolution. The resolution at values of $Zp_{\mathrm{T}} < 100$ GeV is effected by the requirement of having a leading jet with $p_{\mathrm{T}} > 100$ GeV. Above this value the resolution increases with increasing Z boson's p_{T}. As can be seen when the resolution is resolved into components, the increase is in the parallel component, while the perpendicular component remains roughly constant. The resolution rises from approximately 20 GeV at a Z boson's p_{T} of 100 GeV, up to 30-40 GeV at a Z boson's p_{T} of 500 GeV.

With bins of 30 GeV used in the low $E_{\mathrm{T}}^{\mathrm{miss}}$ or $E_{\mathrm{T,had}}^{\mathrm{miss}}$ region of this analysis there is some migration of events from bin to bin. Since the $E_{\mathrm{T}}^{\mathrm{miss}}$ and $E_{\mathrm{T,had}}^{\mathrm{miss}}$ distributions are rapidly falling, this migration is biased towards the direction of larger $E_{\mathrm{T}}^{\mathrm{miss}}$ or $E_{\mathrm{T,had}}^{\mathrm{miss}}$. However, since the dominant resolution effect is that of the $E_{\mathrm{T}}^{\mathrm{miss}}$, rather than the electrons that are used in the $E_{\mathrm{T,had}}^{\mathrm{miss}}$ calculation, the effect of migration should be very similar in the two channels. The measured ratio should therefore not be greatly impacted by any migration effects. Any such impact will be taken into account in the correction calculated in section 5.4.



(a) $E_{\mathrm{T}}^{\mathrm{miss}}$



(b) $E_{\mathrm{T,had}}^{\mathrm{miss}}$

Figure 5.4: Comparisons of the $E_{\mathrm{T}}^{\mathrm{miss}}$ (a) and $E_{\mathrm{T,had}}^{\mathrm{miss}}$ (b) with the truth Z boson's p_{T} after $Z \to ee$ or $Z \to$ inv and leading jet selection.

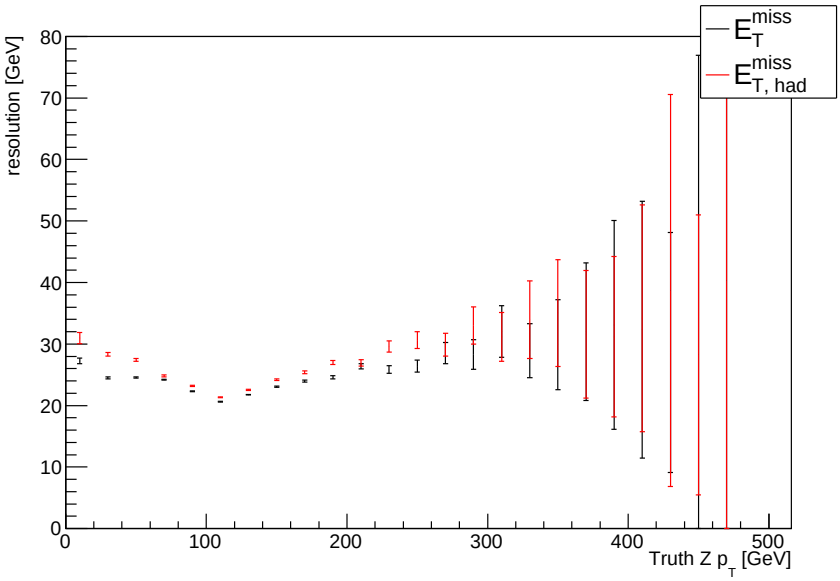
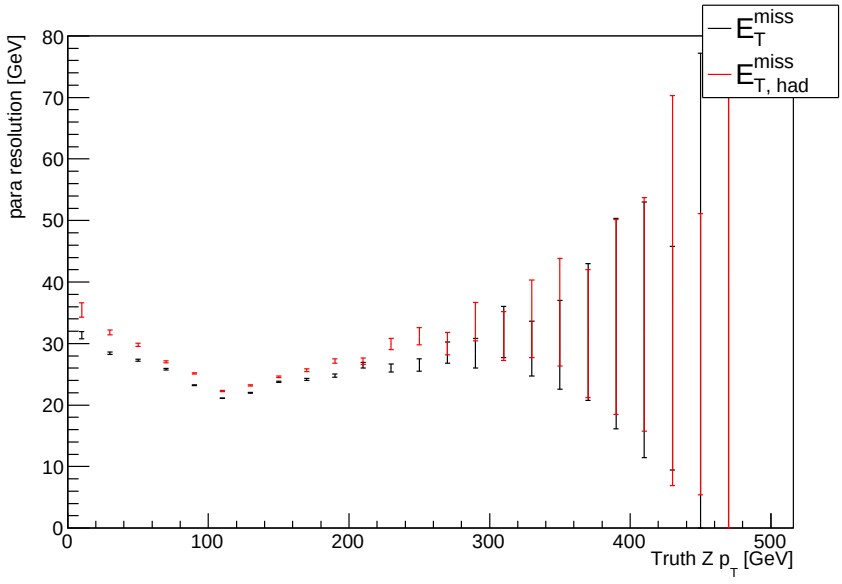
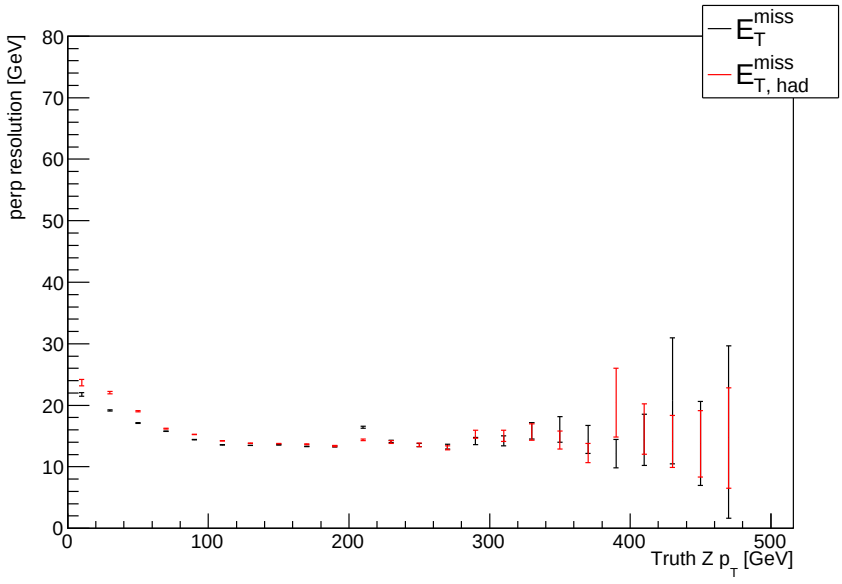


Figure 5.5: $E_{\mathrm{T}}^{\mathrm{miss}}$ and $E_{\mathrm{T,had}}^{\mathrm{miss}}$ resolutions as a function of truth Z boson's p_{T}.



(a) parallel



(b) perpendicular

Figure 5.6: Comparisons of the $E_{\mathrm{T}}^{\mathrm{miss}}$ and $E_{\mathrm{T,had}}^{\mathrm{miss}}$ resolutions parallel to (a) and perpendicular to (b) the truth Z boson's p_{T}.

5.2 Trigger correction

This correction takes into account the difference between the trigger efficiencies in the two channels. The efficiencies were estimated in each channel using MC simulated signal samples. The full jet + $Z \rightarrow \nu\bar{\nu}$ or jet + $Z \rightarrow e^+e^-$ selection, other than the trigger requirement, was made on each channel. The distributions of $E_{\mathrm{T}}^{\mathrm{miss}}$ or $E_{\mathrm{T,had}}^{\mathrm{miss}}$ were then made before and after the respective trigger requirements. The ratio of the post- and pre-trigger distributions were used to estimate the trigger efficiency in each channel. The efficiencies in the two channels are shown in figure 5.7. The requirements on two electrons with a high Z p_{T} means that the electron trigger efficiency was high and fairly uniform in $E_{\mathrm{T,had}}^{\mathrm{miss}}$. The $E_{\mathrm{T}}^{\mathrm{miss}}$ trigger was also highly efficient, especially above 160 GeV.

The trigger efficiency correction, C^{trig}, is estimated as the ratio of the efficiencies in each channel, as shown in figure 5.8. The relative correction is 2.5% in the lowest bin, and then very small in higher bins where the $E_{\mathrm{T}}^{\mathrm{miss}}$ trigger is almost fully efficient. The overall trigger correction was found to be

$$C^{\mathrm{trig}} = 1.01 \tag{5.1}$$

with an uncertainty of less than 0.001.

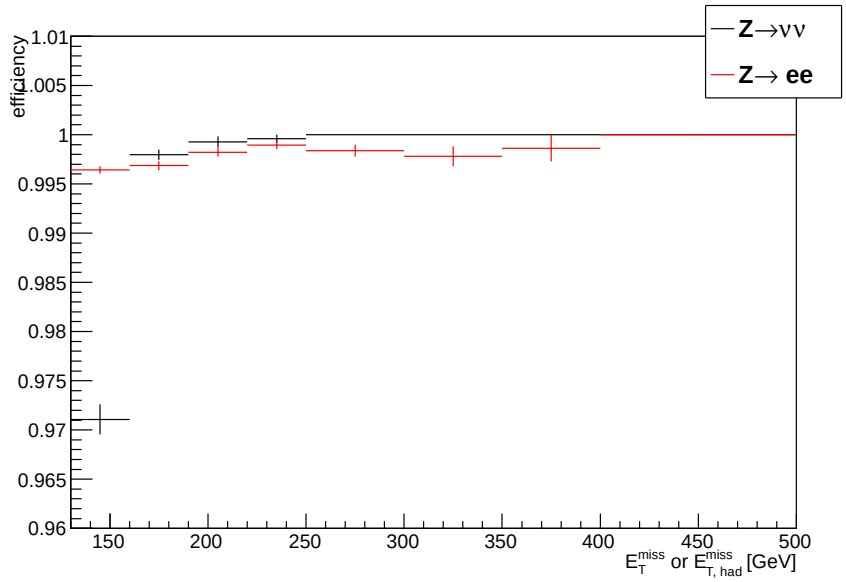


Figure 5.7: Estimated $E_{\mathrm{T}}^{\mathrm{miss}}$ and electron trigger efficiencies as a function of $E_{\mathrm{T}}^{\mathrm{miss}}$ or $E_{\mathrm{T,had}}^{\mathrm{miss}}$ in events used in this analysis.

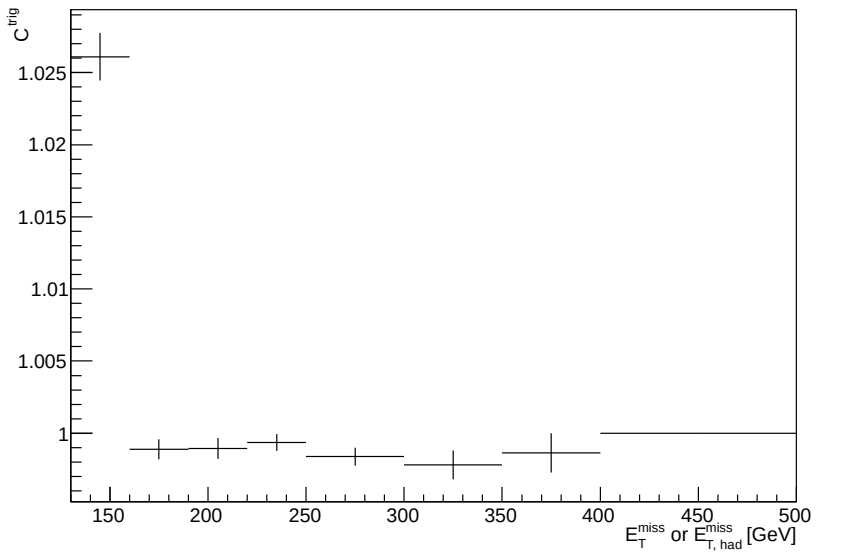


Figure 5.8: Trigger efficiency correction as a function of $E_{\mathrm{T}}^{\mathrm{miss}}$ or $E_{\mathrm{T,had}}^{\mathrm{miss}}$.

5.3 Electron correction

There is a small discrepancy between the electron reconstruction efficiency in the MC simulations and the measured data. The electron reconstruction efficiency difference is provided by an ATLAS. This provides a scale factor for the reconstruction efficiency in the MC to correct it to the data reconstruction efficiency. The efficiency provided depends upon the p_{T} and η of the electron. The $p_{\mathrm{T}} - \eta$ efficiency maps have been calculated using MC studies that produce efficiency maps in small η and p_{T} bins. These are created by simulating $Z \to ee$ events. If one of the electrons is identified then efficiency with which the second electron is also identified can be measured. This is the so called 'tag and probe' method. These maps are then corrected using tag and probe measurements performed on data. Since the data statistics are much lower than the MC statistics that can be generated the data sample measures the map using larger η and p_{T} bins. However this coarser grained map can then be used to scale the MC derived map to the efficiency seen in data. In the correction explained in this section a weighting is assigned for each event as the product of the identification efficiency scale factors for the two electrons from the Z decay. Figure 5.9 shows the distributions of the event weights in MC events passing the $Z \to ee$ channel selection criteria used in the measurement. Figure 5.10 shows the ratio of the distribution of $E_{\mathrm{T,had}}^{\mathrm{miss}}$ in $Z \to ee$ MC events passing the selection criteria with and without this scale factor applied. The event weight is generally slightly below 1.0. The uncertainty is correlated from bin to bin, due to the strong correlation between the electron p_{T} and the $E_{\mathrm{T,had}}^{\mathrm{miss}}$.

The electron correction is made to account for the rate at which truth electrons meeting the measurement's selection criteria are reconstructed to also meet the selection criteria. The correction, C^e, is calculated from the $Z \to ee$ MC sample. The correction is calculated as the ratio of two hadronic recoil distributions.

$$C^e(\text{hybrid } E_{\mathrm{T,had}}^{\mathrm{miss}}) = \frac{Z \to ee^{\mathrm{reco}}(\text{reco } E_{\mathrm{T,had}}^{\mathrm{miss}})}{Z \to ee^{\mathrm{truth}}(\text{hybrid } E_{\mathrm{T,had}}^{\mathrm{miss}})}, \tag{5.2}$$

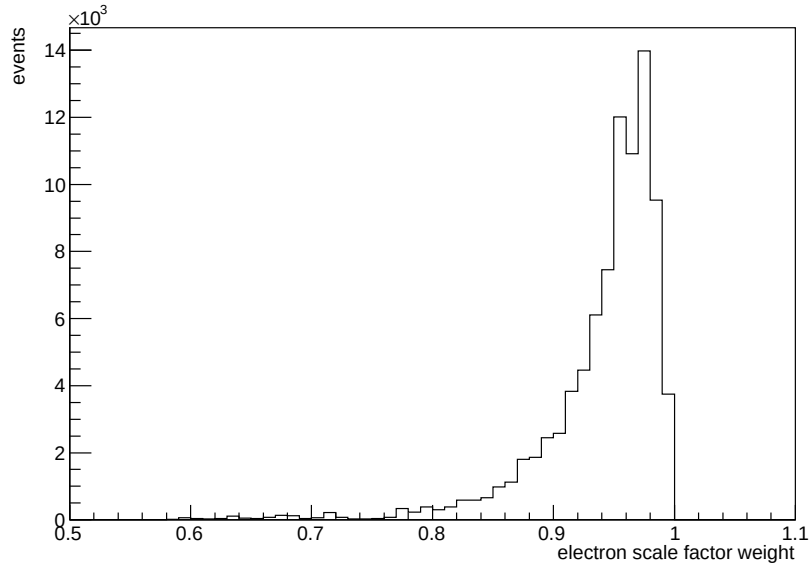


Figure 5.9: Electron reconstruction efficiency scale factor distribution.

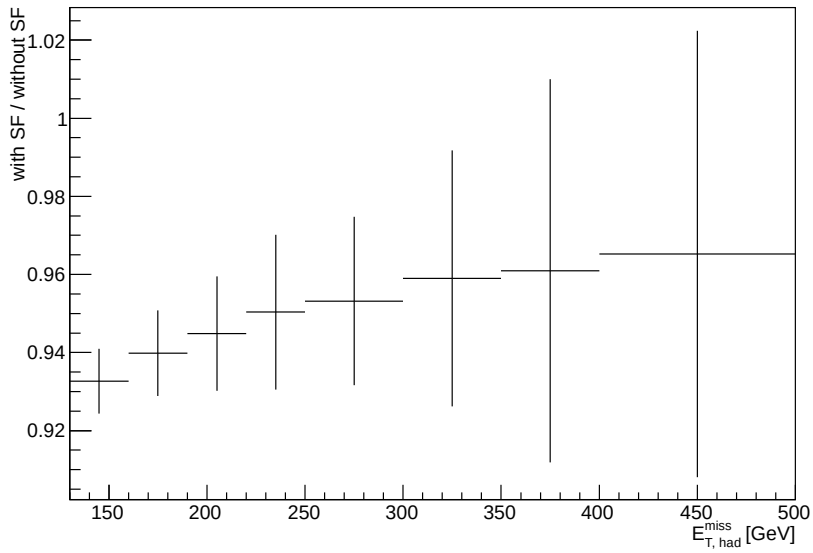


Figure 5.10: Ratio of $E_{\mathrm{T,had}}^{\mathrm{miss}}$ distributions as a function of $E_{\mathrm{T,had}}^{\mathrm{miss}}$, with and without the electron efficiency scale factor applied.

where $Z \to ee^{\text{reco}}$ refers to events selected using the reconstructed electrons, whilst $Z \to ee^{\text{truth}}$ uses truth electrons for the selection. Both are formed from events passing the selection criteria used in the $Z \to ee$ channel of the measurement. One is formed from events where the reconstructed electrons pass the selection criteria whilst the other is from from events where the truth electrons pass equivalent criteria. The truth electrons are found by identifying the final state electrons from the Z decay in the Monte Carlo event record. These electrons are 'dressed' by summing them with the photons radiated by the electrons within a cone of $\Delta R < 0.2$. In the selection using truth electrons the hybrid $E_{\text{T,had}}^{\text{miss}}$ is used. This is the sum of the reconstructed $E_{\text{T}}^{\text{miss}}$ with the momentum of the two truth electrons identified as coming from the Z decay. The correction is found in the hadronic recoil bins used in the measurement. The two hadronic recoil distributions are shown in figure 5.11.

Since the events passing the reconstructed and truth electron selections are highly correlated the sample is split into $N = 10$ slices by event number. For each hadronic recoil bin the correction is calculated as the average of the corrections measured in each slice, with a statistical uncertainty on the mean given by $\text{RMS}/\sqrt{N}$. The correction is shown in figure 5.12. The correction is of order 0.8. It rises as a function of Z boson's p_{T} since the electrons' p_{T} increases with that of the Z boson, and the higher momentum electrons have a higher reconstruction efficiency. The overall value for the correction was found by the same method with a single $E_{\text{T,had}}^{\text{miss}}$ bin to be

$$C^{e} = 0.77 \tag{5.3}$$

with an uncertainty less than 0.002.

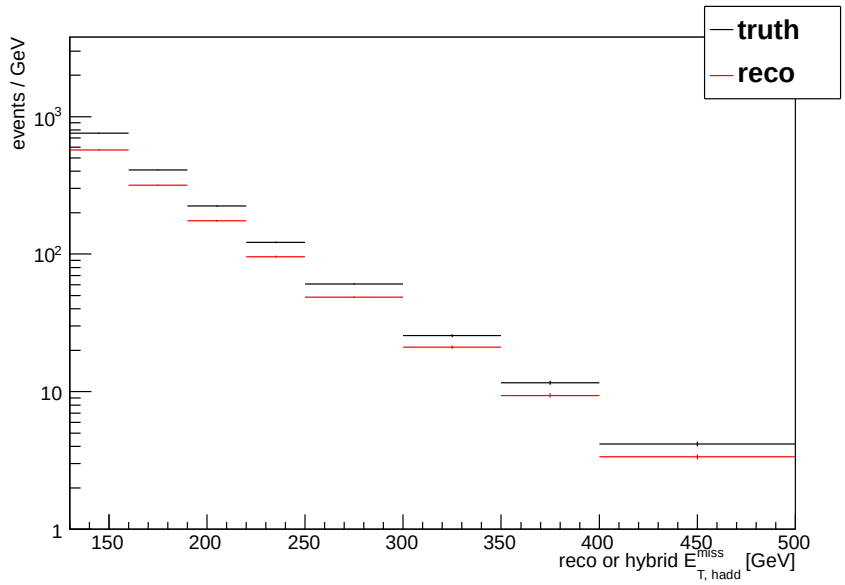


Figure 5.11: Hadronic recoil distributions using truth and reco electron selections.

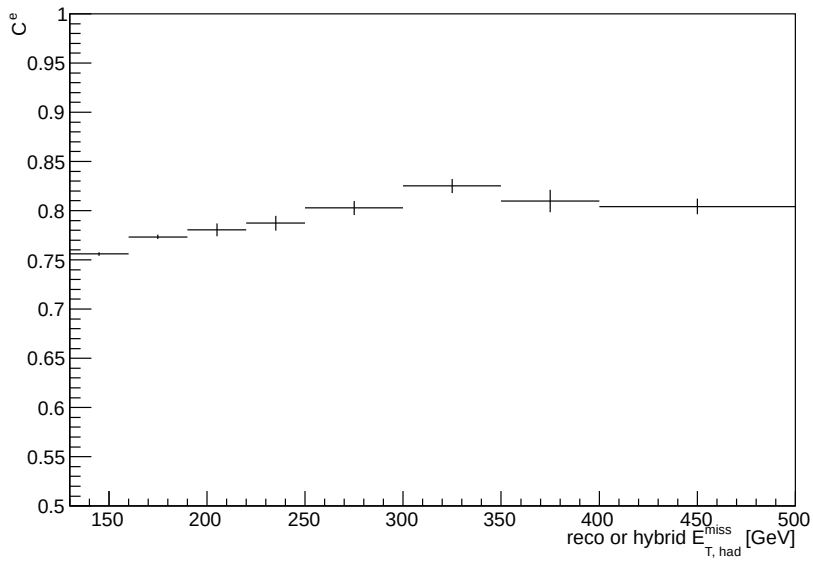


Figure 5.12: The electron selection correction as a function of $E^{\mathrm{miss}}_{\mathrm{T,had}}$.

5.4 Z boson's p_{T} correction

This correction takes into account the small differences in jet reconstruction between the two channels as well as any differences between $E_{\mathrm{T}}^{\mathrm{miss}}$ and $E_{\mathrm{T,had}}^{\mathrm{miss}}$ in measuring the observables of this analysis. The correction also takes into account differences in the efficiencies of the background rejection criteria between the two channels. The measurement has been designed such that this correction should be small and independent of the Z boson's p_{T}. The selection criteria for the $Z \to ee$ and $Z \to \nu\nu$ channels have been carefully selected such that the only major differences are the requirements made upon the electrons in the $Z \to ee$ channel as corresponding selection criteria cannot be made on the neutrinos since they are not detected. For example, the hadronic recoil, $E_{\mathrm{T,had}}^{\mathrm{miss}}$, has been used to model the Z boson's p_{T} in the electron channel even though simply taking the 4-vector sum of the electrons better models the Z. This has been done since the $E_{\mathrm{T,had}}^{\mathrm{miss}}$ also includes the smearing of the Z boson's p_{T} that is introduced in using the $E_{\mathrm{T}}^{\mathrm{miss}}$ in the neutrino channel.

The correction is calculated using a double ratio

$$C^{Zp_{\mathrm{T}}}(Zp_{\mathrm{T}}) = \frac{R_{\mathrm{truth}}^{MC}(Zp_{\mathrm{T}})}{R_{\mathrm{reco}}^{MC}\left(\text{reco } E_{\mathrm{T}}^{\mathrm{miss}} \text{ or hybrid } E_{\mathrm{T,had}}^{\mathrm{miss}}\right)}, \tag{5.4}$$

with the two ratios

$$R_{\mathrm{truth}}^{\mathrm{MC}}(Zp_{\mathrm{T}}) = \frac{Z \to \nu\nu_{\mathrm{truth}}^{\mathrm{MC}}}{Z \to ee_{\mathrm{truth}}^{\mathrm{MC}}} \tag{5.5}$$

and

$$R_{\mathrm{reco}}^{\mathrm{MC}}(Zp_{\mathrm{T}}) = \frac{Z \to \nu\nu_{\mathrm{reco}}^{\mathrm{MC}}}{Z \to ee_{\mathrm{reco}}^{\mathrm{MC}}}. \tag{5.6}$$

The reconstructed ratio uses reconstructed jets, $E_{\mathrm{T}}^{\mathrm{miss}}$ and the background rejection criteria used in the measurement. The reconstructed $Z \to ee$ channel used the hybrid $E_{\mathrm{T,had}}^{\mathrm{miss}}$ defined in the electron correction. The truth ratio uses truth jets and the truth Z boson's p_{T} in place of either $E_{\mathrm{T}}^{\mathrm{miss}}$ or $E_{\mathrm{T,had}}^{\mathrm{miss}}$ and does not use the background rejection criteria. The truth jets are made from the final state particles in the Monte Carlo event record. The visible particles are clustered using the anti-k$_T$

algorithm to form 'truth' jets. The truth Z boson's p_{T} is found from the sum of the 4-momenta of the truth neutrinos or born electrons identified in the event record as coming from the Z decay. Since the corrections due to the electrons were calculated separately, both the truth and reco $Z \to ee$ selections are made on truth electrons. Due to the Z selection on truth electrons in the reconstructed $Z \to ee$ selection the isolated track veto and the electron veto have to be modified in this channel to ignore tracks or electrons matched to the truth electrons identified as coming from the Z boson.

After the events have been selected the truth Z boson's p_{T}, reconstructed $E_{\mathrm{T}}^{\mathrm{miss}}$ and hybrid $E_{\mathrm{T,had}}^{\mathrm{miss}}$ distributions are used to calculate the double ratio that forms the correction. The hybrid $E_{\mathrm{T,had}}^{\mathrm{miss}}$ uses the reconstructed $E_{\mathrm{T}}^{\mathrm{miss}}$ summed with the truth electrons used in the selection as the electron correction handles the correction due to electron reconstruction. Since the truth and reco selection are highly correlated in both the $Z \to ee$ and $Z \to \nu\nu$ channels the sample is split into a number of slices, $N = 10$. The correction for each Z boson's $p_{\mathrm{T}}/E_{\mathrm{T}}^{\mathrm{miss}}/E_{\mathrm{T,had}}^{\mathrm{miss}}$ bin used in the measurement is found in each slice. The final correction for the bin is then found as the mean of these values and its statistical uncertainty is estimated as the error on this mean as the RMS$/\sqrt{N}$. The correction is shown in figure 5.13, which shows a flat relative correction of 1.5%. Below the Z boson's p_{T} threshold the correction diverges from unity due the turn on of the 100 GeV leading jet cut. This can be seen in figure 5.14, where the correction is compared with a correction performed with a lower leading jet threshold of 60 GeV, and also with all events in the $Z \to ee$ and $Z \to \nu\nu$ MC samples. In the low jet threshold correction the turn on in the 70 - 130 GeV region is no longer evident and a similar turn on (not shown) can bee seen in the 60 GeV region. As these events in the jet turn on region are not used in the analysis, where 130 GeV $E_{\mathrm{T}}^{\mathrm{miss}}$ or $E_{\mathrm{T,had}}^{\mathrm{miss}}$ is required, the shape in this region does not effect the measurement. The similarity between the full selection correction and the no selection comparison shows that the measurement does indeed minimise the differences due to detector effects other than due to electrons, as it was designed to

do. A single value of the correction was found by the same method using a single p_{T} bin as

$$C^{Zp_{\mathrm{T}}} = 1.01 \tag{5.7}$$

with an uncertainty less than 0.004.

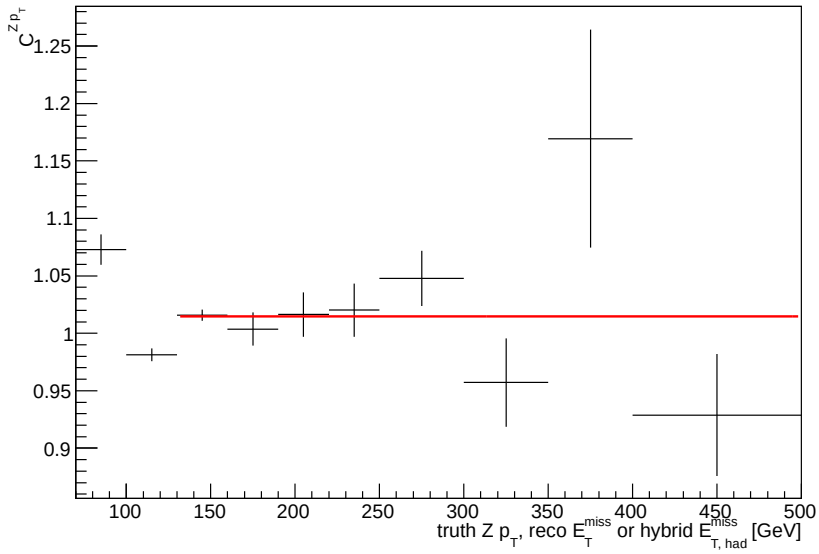


Figure 5.13: Correction for the Z momentum, jet reconstruction and background rejection cuts as a function of Z boson's p_{T}.

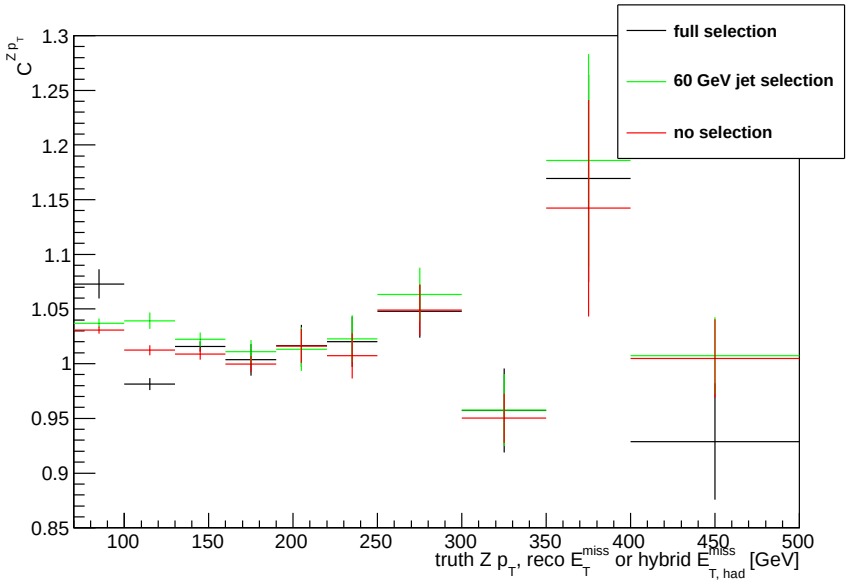


Figure 5.14: Comparison of Z boson's p_{T} correction as a function of truth Z boson's p_{T} with different selection criteria.

5.5 Electron acceptance correction

This correction takes account of the difference due to the fact that the neutrinos (or any non-SM invisible particles) are inferred, while the electrons must be detected. The electrons must therefore be within the decay phase space where detection is possible, while the neutrino events can be selected in the full neutrino phase space. A sample of 7.45 million jet$+Z \to e^+e^-$ events was generated using PYTHIA 8.160. Events were selected that had a truth leading jet with $p_{\mathrm{T}} > 100$ GeV and $|\eta| < 2.0$ after the jet-electron overlap reduction, as is required in the measurement. The truth level Z was required to have $p_{\mathrm{T}} > 130$ GeV to mimic the $E^{\mathrm{miss}}_{\mathrm{T,had}}$ requirement in the measurement. Using this sample, an estimation of the proportion of events with electrons outside of the acceptance used in the measurement was made.

Electrons have three main factors dictating whether the are within the measurement's acceptance. The electrons are both required to have $p_{\mathrm{T}} > 20$ GeV and at least one is required to have $p_{\mathrm{T}} > 25$ GeV. They are both required to be within $|\eta| < 1.37$ or $1.52 < |\eta| < 2.47$. The two electrons in an event are required to be separated by $\Delta R = \sqrt{\Delta\eta^2 + \Delta\phi^2} > 0.2$. Figures 5.15 to 5.17 show the distributions of these factors as well as indicating those electrons or events that fall outside of the acceptance in each.

The number of events where both electrons pass the p_{T} and η requirements, and where the pair pass the ΔR requirement are shown in table 5.2. As can be seen in the figures and in the table, the p_{T} cut has the largest impact on the acceptance. The electron criteria selected 1.1 of the 1.9 million $Z \to ee$ events that had passed the jet and $E^{\mathrm{miss}}_{\mathrm{T,had}}$ requirements. This results in an estimated lepton acceptance, $a_e = 0.589 \pm (4 \times 10^{-4})$, where the binomial uncertainty is purely statistical. The statistical uncertainty is negligible. The number of electron events should therefore be corrected as

$$N'_{Z\to ee} \propto \frac{1}{a_e} N^{\mathrm{meas}}_{Z\to ee} \tag{5.8}$$

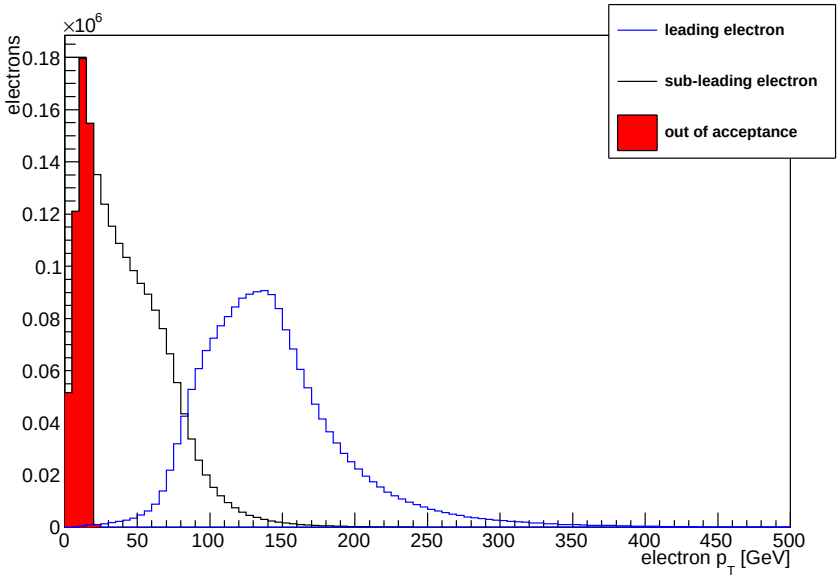


Figure 5.15: p_{T} distribution of electrons in jet + $Z \to e^+e^-$ events.

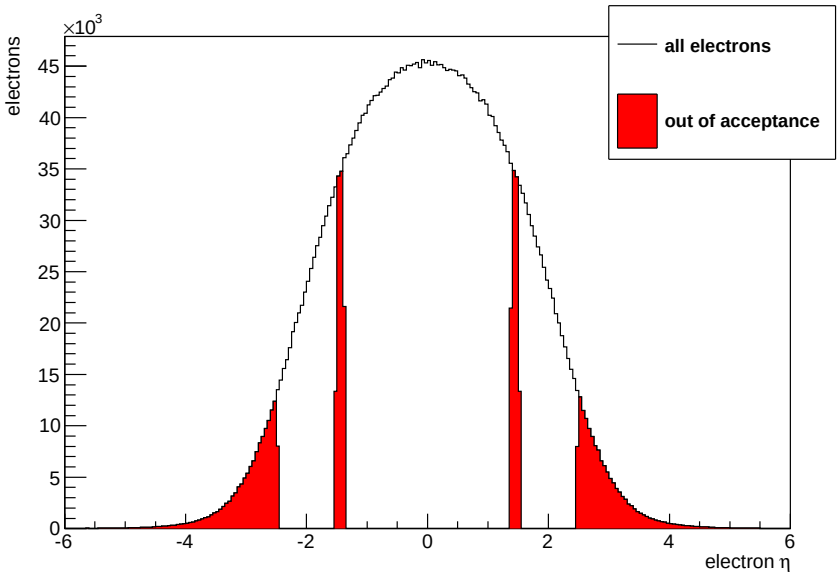


Figure 5.16: η distribution of electrons in jet + $Z \to e^+e^-$ events.

leading to a correction on the measured ratio of

$$\delta_a = a_e = 0.578. \tag{5.9}$$

As can be seen in figure 5.18, the acceptance factor increases as a function of Z boson's p_{T} from approximately 0.55 to 0.75. This is due to the fact that events with higher Z boson's p_{T} have electrons with higher p_{T} electrons, which are more likely to be within the detector's acceptance.

Table 5.2: Events passing the electron requirements.

Requirement	Events [million]
Initial	7.45
Leading jet	3.85
Z boson's p_{T}	1.86
$p_{\mathrm{T}} > 20, 25$ GeV	1.09
$\lvert\eta\rvert < 1.37$ or $1.52 < \lvert\eta\rvert < 2.47$	1.09
$\Delta R(e, e) > 0.2$	1.07

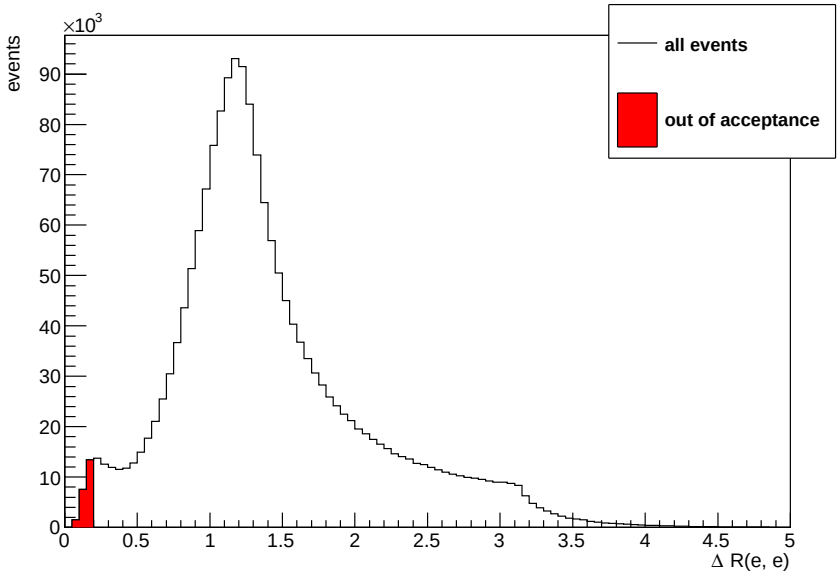


Figure 5.17: $\Delta R(e, e)$ distribution in jet $+ Z \to e^+e^-$ events.

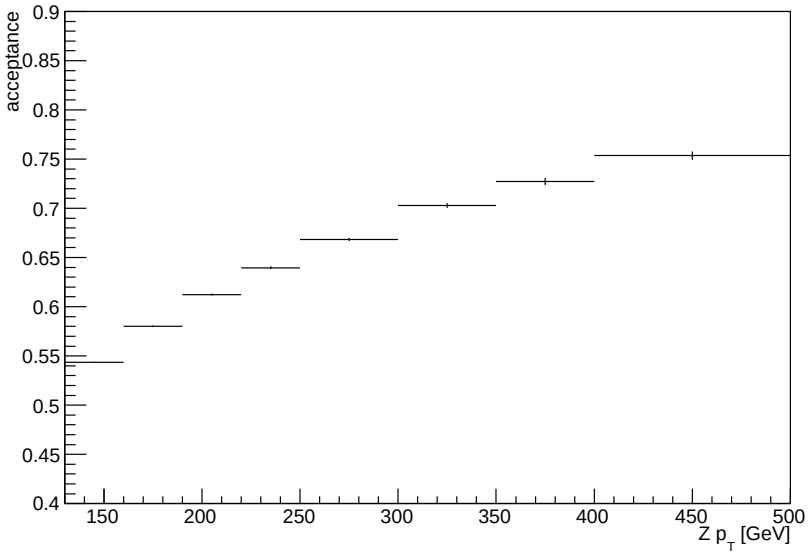


Figure 5.18: Acceptance correction as a function of Z boson's p_{T}.

5.6 γ^* interference correction

The $Z \to ee$ channel measures the Z/γ^* interaction. A cut on the invariant mass of the electron pair around the Z mass is used to select predominantly Z-like interactions. The $Z \to \nu\nu$ channel has no such invariant mass cut, however it measures only a pure Z interaction. The γ^* interference correction is used to treat the $Z \to ee$ channel as if it were purely a Z interaction with no invariant mass cut.

The correction was calculated using a PYTHIA 8.160 sample. Two separate $Z \to ee$ + jets samples were generated. The difference between the two samples is that one sample has the full Standard Model Z/γ^* interaction, whereas the other has an artificial purely Z interaction. In the Z/γ^* sample a m_{ee} mass window in the measurement is required, whereas in the pure Z sample no such requirement is made. The ratio of the number of events in each channel then gives a correction factor to be applied to the measured jet + $Z \to e^+e^-$ channel.

The number of events generated in the Z/γ^* and the pure Z samples were 7.45 million and 7.4 million, respectively. Events were selected by requiring that the leading truth jet was central ($|\eta| < 2.0$) and with $p_{\mathrm{T}} > 100$ GeV after jet-electron overlap reduction, as is required in the measurement. No requirements were placed on the electrons so that the correction is measured with full phase space electrons. The truth level Z boson was required to have $p_{\mathrm{T}} > 130$ GeV to mimic the measurement's $E_{\mathrm{T,had}}^{\mathrm{miss}}$ requirement. Figure 5.19 shows the Z boson's invariant mass distributions in the pure Z and the Z/γ^* samples.

Using these events a correction factor can be calculated by comparing the number of events where the di-electron invariant mass falls into a window of width 50 GeV, $66 < m_{ee} < 116$ GeV, in the Z/γ^* sample, to the total number of events in the pure Z sample. Table 5.3 shows the number of events in each sample passing the selection criteria. In order for the correction to be valid the number of events in the pure Z sample is scaled to the same luminosity as was generated in the Z/γ^* sample. The

correction factor for the number of electron events is therefore

$$\delta_e = \frac{N_Z}{N_{Z/\gamma^*}^{66<m_{ee}<116 \text{ GeV}}} \tag{5.10}$$

and so the correction on the ratio is

$$\delta_\gamma = \delta_e^{-1}. \tag{5.11}$$

The resulting correction is found to be

$$\delta_\gamma = 0.992 \tag{5.12}$$

with a negligible statistical uncertainty.

Table 5.3: Events passing the analysis criteria in the pure Z and Standard Model $Z \to ee$ samples.

Cut	Pure Z events		SM Z/γ^* events	
	Total	$1fb^{-1}$	Total	$1fb^{-1}$
Initial	7400000	11898.7	7450000	13617.8
Leading jet	4831598	7768.85	4809006	8790.36
Hadronic recoil	1937496	3115.35	1911793	3494.56
Z mass	N/A	N/A	1691033	3091.03

Figure 5.20 shows the correction ratio as a function of the Z boson's p_{T}. A linear fit has been made that shows that the correction factor is constant in Z boson's p_{T} and so the correction is applied to the measured ratio simply as a multiplication factor.

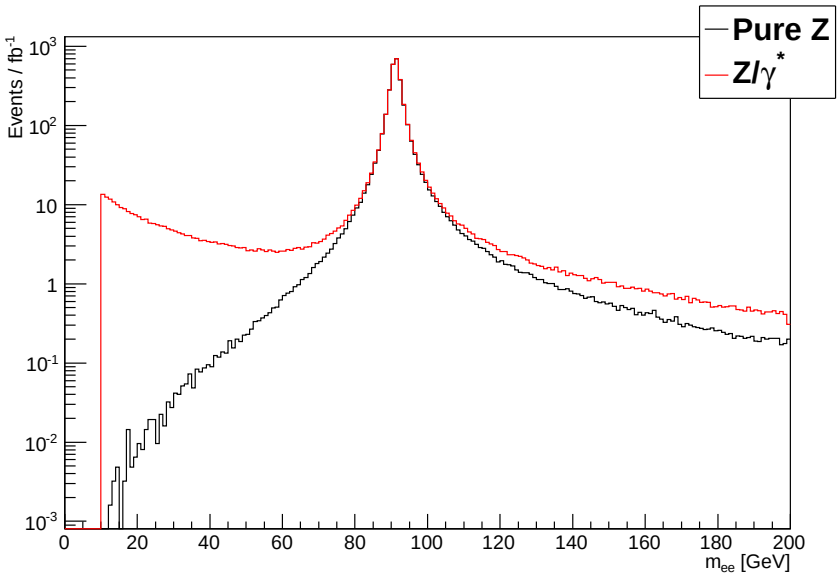


Figure 5.19: Invariant mass distribution in both channels, scaled to the same luminosity.

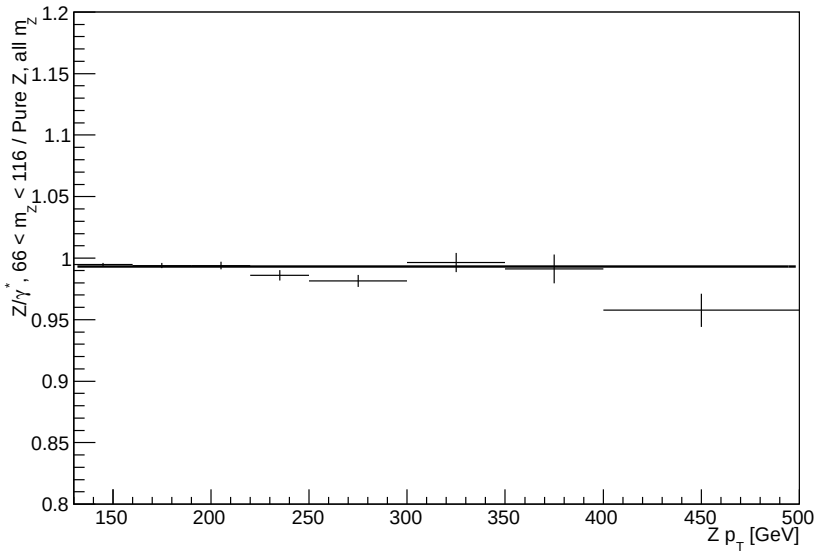


Figure 5.20: Correction factor, δ_γ, as a function of the Z boson's p_{T}.

5.7 Invisible width extraction

With the corrections calculated in this section it is possible to extract a measurement of the invisible width from the measured ratio. The measured ratio is corrected to a ratio of branching ratios as

$$\frac{BR(Z \to \nu\nu)}{BR(Z \to ee)} = \frac{N^{\text{meas}}_{Z\to\nu\nu} - N^{\text{bkg, est.}}_{Z\to\nu\nu}}{N^{\text{meas}}_{Z\to ee} - N^{\text{bkg, est.}}_{Z\to ee}} \times C^{\text{trig}} \times C^{e} \times C^{Z} \times C^{a} \times \delta^{\gamma}, \qquad (5.13)$$

where the terms are all as a function of Z p_{T}, $E^{\text{miss}}_{\text{T}}$ or $E^{\text{miss}}_{\text{T,had}}$ other than the δ^{γ} correction, which is a constant value. The product of the various corrections is shown in figure 5.21. The differential measurement of the invisible width comes from the product of of the combined corrections, the measured ratio that was shown in figure 4.18 and the world average of the Z's partial width to electrons, which is $\Gamma(Z \to ee) = 83.91 \pm 0.12$ MeV. The measured invisible width is shown in figure 5.22.

A single value for the invisible width was found by fitting a constant value to the differential result. The invisible width and its statistical uncertainty was

$$\Gamma(Z \to \text{inv}) = 480.5 \pm 5.0 \text{ MeV}. \qquad (5.14)$$

This value was found with $\chi^2/\text{NDF} = 3.8$ for the resulting fit. The systematic uncertainty in the measurement is estimated in chapter 6.

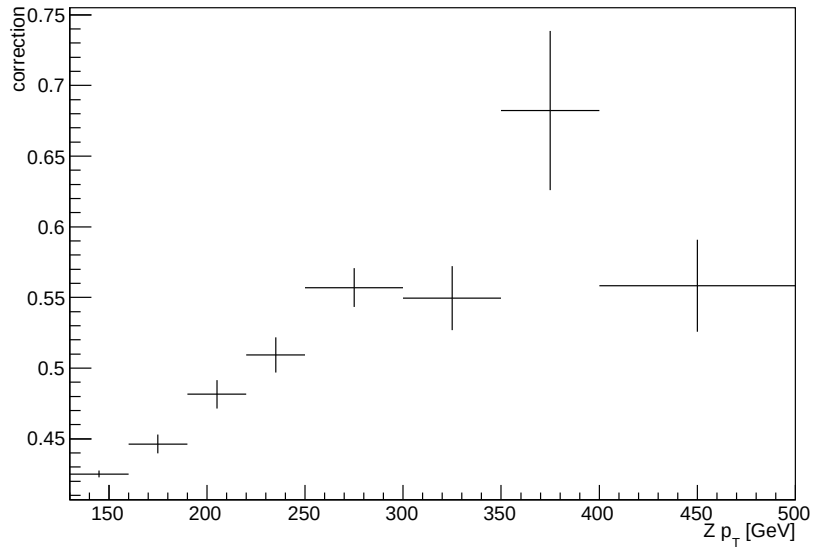


Figure 5.21: Product of different corrections as a function of Z boson's p_{T}.

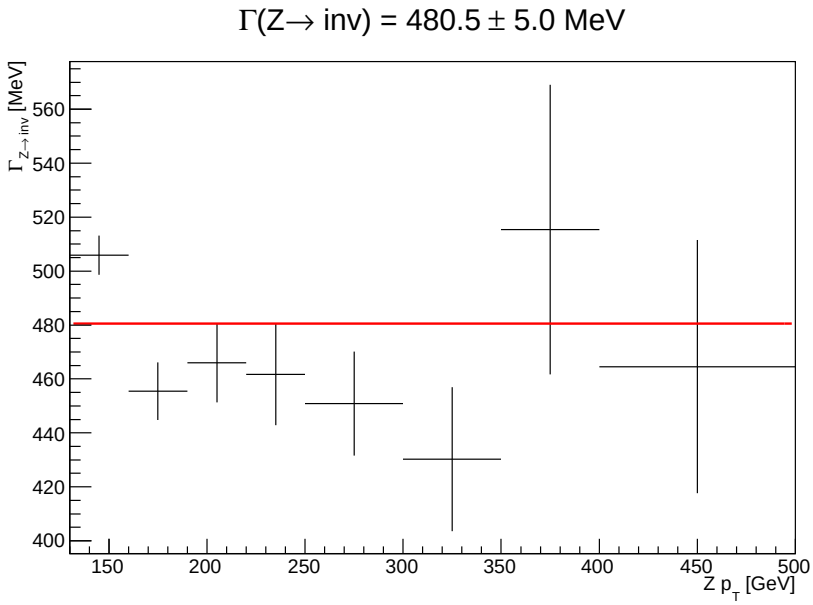


Figure 5.22: Measured invisible width as a function of Z boson p_{T}, with the calculated width of $\Gamma(Z \to \mathrm{inv}) = 480.5 \pm 5.0$ MeV.

Chapter 6

Estimation of systematic uncertainties

Systematic uncertainties are introduced into the analysis from a number of sources. They are all evaluated in a similar way by varying some parameters used in the analysis. The analysis is performed by calculating a number of terms given in equation (5.13). Each source of systematic uncertainty is evaluated by re-evaluating any relevant terms in that equation given a systematic variation in a parameter. The whole equation is then evaluated to give a final systematically shifted value of the invisible width. The total systematic uncertainty on the measurement can then be estimated as the sum (in quadrature) of all the systematic shifts from the central value. By evaluating the systematic uncertainties in this way no calculation of the complicated correlations between the different terms in equation (5.13) was required.

A number of experimental and theoretical sources of systematic uncertainty have been evaluated. The theoretical uncertainties that have been evaluated include the methods of estimating backgrounds and the choice of parton density function used for the Monte Carlo simulations. The experimental uncertainties predominantly come from the reconstruction of the jets and the electrons. The uncertainty in the measured width due to the uncertainties in the energy scale of both the electrons

and jets have been estimated. The uncertainty in the electron identification scale factor has also been taken into account, as has the uncertainty due to the effect of changing pileup conditions over the year's data taking.

In the following sections the different systematic uncertainties are estimated, giving a final value for the measured invisible width complete with statistical and systematic uncertainty.

6.1 Background estimations

The dominant background in this analysis is the $W \to \tau\nu$ background in the $Z \to \nu\nu$ channel. A best estimate of this background was made by using a simulation of the background, scaled by a data/MC ratio of the $W \to e\nu$ and $W \to \mu\nu$ selections. Whilst the $W \to e\nu$ and $W \to \mu\nu$ scale factors agree well with each other the $W \to \tau\nu$ background is subtly different to these backgrounds. The $W \to e\nu$ and $W \to \mu\nu$ backgrounds come from events where the charged lepton is not noticed by the electron, muon or isolated track vetoes. The $W \to \tau\nu$ background is very similar in the case that the τ decays leptonically. However with leptonic decays the momentum of the charged lepton is generally lower than in the $W \to e\nu$ or $W \to \mu\nu$ channels and there are additional neutrinos, so the $E_{\mathrm{T}}^{\mathrm{miss}}$ may be increased. The τ can also decay hadronically, in which case there is no charged lepton to veto. Hadronic τ jets generally have either one or three tracks, and so the isolated track veto can remove many of the hadronic τ events, and the τ jet is often aligned with the $E_{\mathrm{T}}^{\mathrm{miss}}$ which also removed events due to the $\Delta\phi(\mathrm{jet}, E_{\mathrm{T}}^{\mathrm{miss}})$ cut. However since the $W \to \tau\nu$ event signature differs from that of the $W \to e\nu$ or $W \to \mu\nu$, the scaling factor derived from these two channels may differ from a data/MC ratio of $W \to \tau\nu$ events. The data/MC scaling factor corrects for a number of factors, including higher order QCD corrections for the production of W bosons, the luminosity of the data sample and the trigger efficiency in these events. These factors should be common to all W boson decays. However there is a residual difference between data and MC that is not taken into account, which is due to the differences in the reconstructed

leptons. Since the scale factors derived from the $W \to e\nu$ and $W \to \mu\nu$ agree well with each other the differences between leptons in data and MC must be small compared to the differences in W production. The scale factors should therefore be expected to model the leptonic $W \to \tau\nu$ events well. The hadronically decaying $W \to \tau\nu$ events, however, have additional small differences due to the addition of an extra jet which may slightly degrade the $E_{\mathrm{T}}^{\mathrm{miss}}$ calculations, for example. This introduces a systematic uncertainty on the analysis that is difficult to quantify. Whilst the difference due to hadronic decays is likely to be a small correction to the W production scale factor, a conservative estimation of the systematic uncertainty it introduces has been estimated by varying the scale factors applied to the $W \to \tau\nu$ MC. The scale factor $s = 1 - \delta$ was varied to $s = 1 - 0.5\delta$ and $s = 1 - 1.5\delta$. The amount of scaling was arbitrarily chosen in order to conservatively estimate this uncertainty. The difference between the measured invisible width with and without the $W \to l\nu$ scale factor applied to the $W \to \tau\nu$ background estimations is $\pm$17.0 MeV, which is a 3.5% systematic uncertainty on the measurement. This is a large shift since the $W \to \tau\nu$ background corresponds to roughly 40% of the $Z \to \nu\nu$ signal. The effect that this systematic shift has on the measurement is shown in figure 6.1.

The two QCD background estimations also introduce systematic uncertainties due to their methods. In the $Z \to \nu\nu$ channel the uncertainty comes from the background estimation in the QCD control region, as the shape of the removed backgrounds has a large impact on the fit. The fitting procedure also introduces an uncertainty. However, since the estimated QCD background in the $Z \to \nu\nu$ channel is of order 0.6%, the systematic uncertainty will have only a small impact on the invisible width measurement. Similar uncertainties are present in the $Z \to ee$ channel's QCD estimation, which relied on background estimations in the QCD control region and the fitting method. This uncertainty will contribute even less to the uncertainty on the invisible width since the estimated QCD background on the $Z \to ee$ channel is less than 0.3%. Since the uncertainties have little impact they

have been conservatively estimated by simply scaling the two QCD backgrounds by ±100%. The calculated invisible widths after applying each of these shifts individually is shown in table 6.1. The estimated systematic uncertainties due to the QCD background estimations in the $Z \to \nu\nu$ and $Z \to ee$ channels are ±3.0 MeV and ±1.5 MeV, respectively. Figure 6.1 shows the impact of these systematic uncertainties upon the measurement.

Table 6.1: Estimated systematic uncertainties due to background estimations.

Systematic	Invisible width [MeV]	Uncertainty [MeV, %]
$W \to \tau\nu$ scale up	463.5	-17.0, 3.5
$W \to \tau\nu$ scale down	497.5	17.0, 3.5
$Z \to ee$ QCD up	482.0	1.5, 0.3
$Z \to ee$ QCD down	479.0	-1.6, 0.3
$Z \to \nu\nu$ QCD up	477.5	-3.0, -0.6
$Z \to \nu\nu$ QCD down	483.5	3.0, 0.6

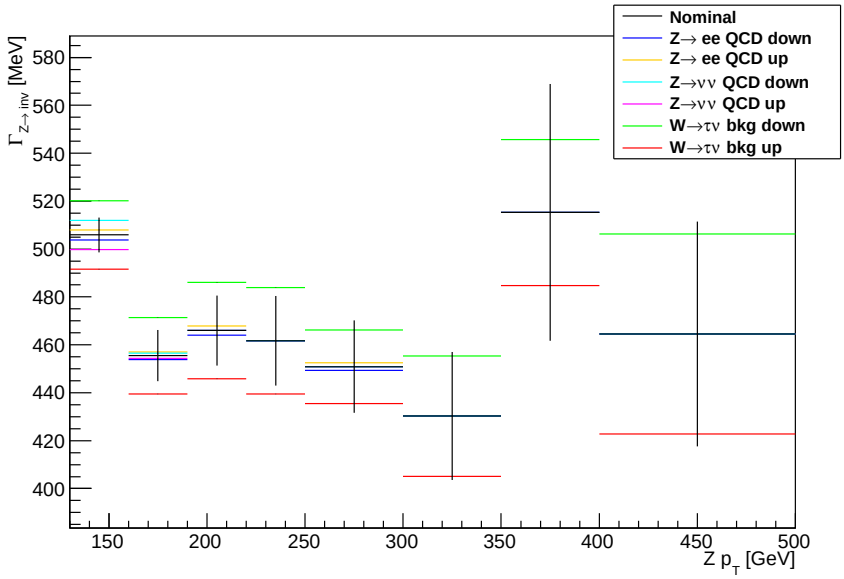


Figure 6.1: Variation in measurement of the invisible width as a function of Z boson's p_{T} due to systematic shifts in the background estimations.

6.2 Parton density functions

The simulated event samples use a set of PDFs, as explained in section 1.2. These functions give the probability for the parton-parton pair in a proton-proton collision to be of specific flavours, with specific fractions of each proton's momentum and with a given momentum transfer. There are a number of uncertainties in the result of the best fit of the PDF to all these data. The error matrix for each PDF has been diagonalised, giving a number of eigenvalues for uncorrelated sources of systematic uncertainty to the PDF. Each PDF comes with an error set. This gives the result of fitting the PDF with a 1 σ shift up and down for each of these eigenvalues. Using the LHAPDF[32] tool it is possible to estimate the uncertainty on a measured value due to the uncertainties upon the PDF used in any simulated samples. This tool allows a number of event weights to be calculated for each simulated event. For each of the two PDFs from systematically shifting an eigenvalue up or down the event weight is found by taking the ratio of the probability the original PDF produces the collision partons in the event to the probability that the shifted PDF would have produced those two partons. For a given analysis the result of the simulation can therefore be shifted $2 \times N$ times by applying the weights from shifting the N eigenvectors up or down on an event by event basis. If the central value measured was X then this procedure produces N values from systematic up shifts, X_i^+, and N from systematic down shifts, X_i^-. The total upward and downward shift on the calculated value, X, is then given by

$$\Delta X^+ = \sqrt{\sum_{i=1}^{N} [\max(X_i^+ - X, X_i^- - X, 0)]^2} \tag{6.1}$$

$$\Delta X^- = \sqrt{\sum_{i=1}^{N} [\max(X - X_i^+, X - X_i^-, 0)]^2}. \tag{6.2}$$

The subtlety that the maximum of the two shifts differences from the central value, or alternatively 0, is used for each shifted eigenvalue is due to the fact that a systematic shift upwards in any given eigenvalue is not guaranteed to increase the calculated

result. Similarly a downwards shift is not guaranteed to decrease the calculated result. As such the maximum upward or downward shift should be used in evaluating systematic upward or downward shifts of the measured value due to choice of PDF.

The measurement of the invisible width relies heavily upon ratios of simulations. By taking ratios of two simulated samples using the same PDF set the uncertainty due to the PDF shifting mostly cancels. The three factors of equation (5.13) where this is not the case is the correction for the electron acceptance and the purely MC based background estimations to $Z \to \nu\nu$ or $Z \to ee$. The purely MC based background estimations account for approximately less than 1% of either channel, and so the PDF systematic uncertainty from these backgrounds will have a negligible impact upon the measured width.

The PDF uncertainty was estimated for the electron acceptance correction factor, using the procedure of weighting each event for each systematic shift. The combined result of shifting the different eigenvalues is a change of ±2.0 MeV, or 0.4%.

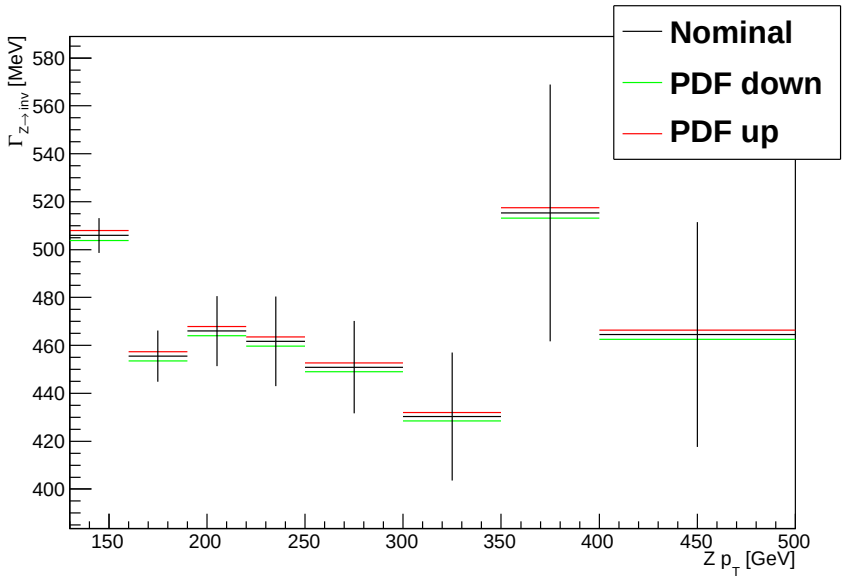


Figure 6.2: Variation in measurement of the invisible width as a function of Z boson's p_{T} due to systematic shifts in the PDF.

6.3 Jets

The Jet Energy Scale (JES), used to calibrate the energy of jets from the electromagnetic scale has been determined from test beam data, MC studies and physics analyses such as studying the momentum balance of jets recoiling from photons. There is an uncertainty in the JES of order 1%. By taking the ratio of two channels which should have the same hadronic activity, this uncertainty should have a small impact on the measured value of the invisible width. A systematic uncertainty has been measured by scaling the reconstructed jets up and down by the uncertainty in the JES. This impacts the events selected from data, the background estimations, the trigger correction, the electron correction and the Z p_{T} correction. The measurement has been performed with the JES shifted up and down and a systematic uncertainty estimated by the variation in the measured width in each case. The uncertainty was again taken from the variations in the extracted width, and found to be asymmetric, with values of $+1.6$ and -3.3 MeV. An average of the two was taken as a symmetric uncertainty of ± 2.5 MeV or $\pm 0.5\%$. The JES systematic shifts have a complicated impact on the measurement, since it probes how well the event selection and corrections controlled differences between the two channels in the jet $+$ Z production. The fact that this uncertainty is small shows validates the selection and correction procedures developed for this measurement. The impact of the systematic shifts upon the measured width is shown in figure 6.3.

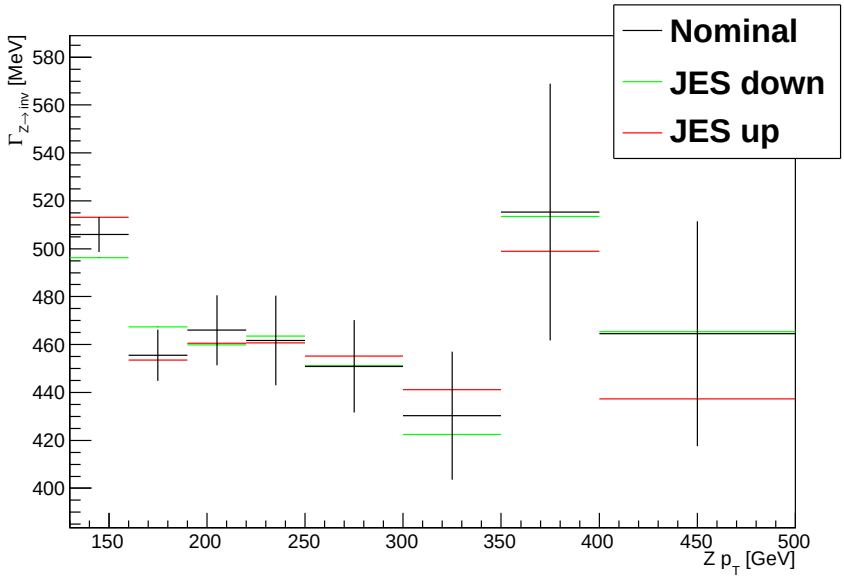


Figure 6.3: Variations in the measured invisible width as a function of Z boson's p_{T} due to systematic shifts in the Jet Energy Scale.

6.4 Electrons

In the MC samples the electron's energy has been corrected to better match the energy of electrons measured in data [33]. This correction is provided along with an uncertainty on the scaling. A systematic uncertainty due to incorrect scaling of the electron's energy has been estimated using the provided uncertainties. The uncertainty was estimated by scaling the electrons' energy up and down by the uncertainty in the scaling factor and measuring the invisible width in the two cases. This systematic shift impacts the MC samples used in the $Z \to ee$ background estimations, the electron trigger efficiency and the electron correction. The uncertainty was then calculated by comparing the extracted invisible width with the central value and found to be ± 8.7 MeV or $\pm 1.8\%$. The impact of the systematic shifts upon the measured width is shown in figure 6.4.

There is also an uncertainty due to the electron identification efficiency scale factor that is applied to the MC samples. The uncertainty in the scaling factors is propagated to an uncertainty on the invisible width by measuring the width with the scale factors systematically shifted up or down. As with the energy scale factors this impacts the MC samples used in the $Z \to ee$ background estimations, the electron trigger efficiency and the electron correction. The resulting uncertainty is found to be ± 5.1 MeV or $\pm 1.1\%$. The variations are also shown in figure 6.4.

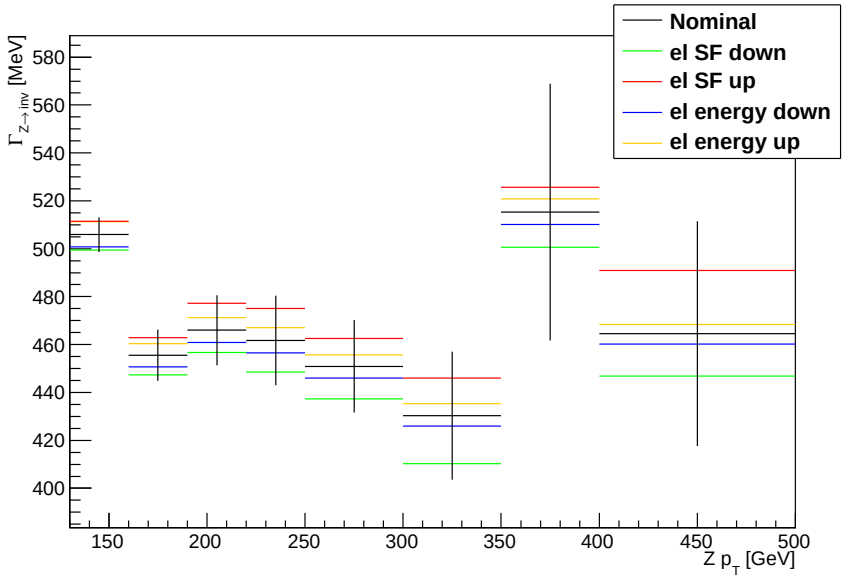


Figure 6.4: Variations in the measured invisible width as a function of Z boson's p_{T} due to systematic shifts of the electron energy or identification scale factors.

6.5 Pileup

A systematic uncertainty due to the changing pileup conditions of the data taking period has been considered. The stability of the measurement in different pileup conditions has been measured by splitting the events selected from the data sample into low- and high-pileup sub samples. The average number of interactions per beam crossing, μ, varied from 10 to 35 over the data taking period. The two sub samples have therefore been been separated by the average $\mu = 20.5$. The ratio of the $E_{\mathrm{T}}^{\mathrm{miss}}$ or $E_{\mathrm{T,had}}^{\mathrm{miss}}$ distributions measured in data for the low- and high-pileup conditions was found for the $Z \to \nu\nu$ and $Z \to ee$ channels respectively. This is shown in figure 6.5, where it can be seen that there is approximately a 5% decrease in the events in the high-pileup sample. However, the important value is the measured ratio of the two channels. The ratios in the low- and high-pileup samples were measured and the ratio of these is shown in figure 6.6. The ratio is consistent with unity, showing that the effect of pileup cancels by taking the ratio of the two channels. Since the measured ratio is robust against changing pileup conditions and the simulated samples have all been weighted to give the sample pileup conditions as the data sample, the uncertainty due to mismeasurement of the pileup conditions is estimated to be negligible.

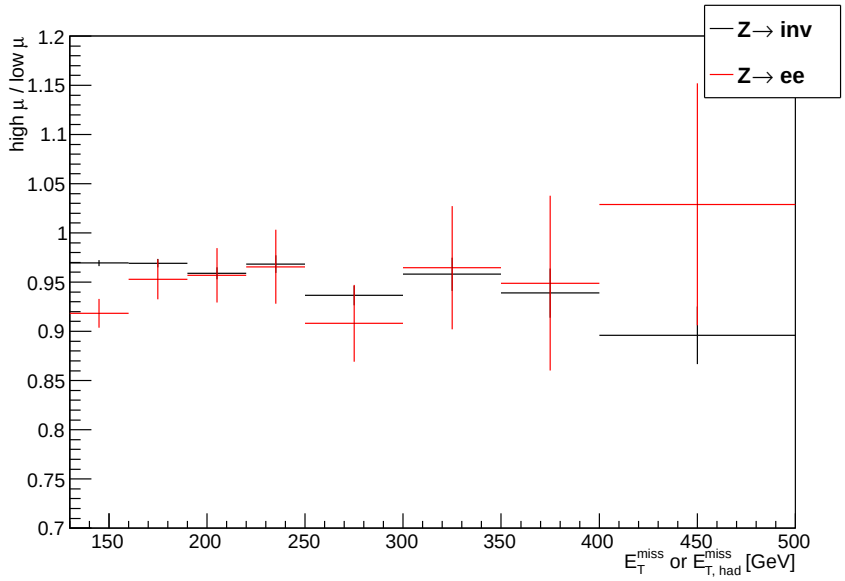


Figure 6.5: Ratios of measured $E_{\mathrm{T}}^{\mathrm{miss}}$ or $E_{\mathrm{T,had}}^{\mathrm{miss}}$ distributions in low- and high-pileup conditions.

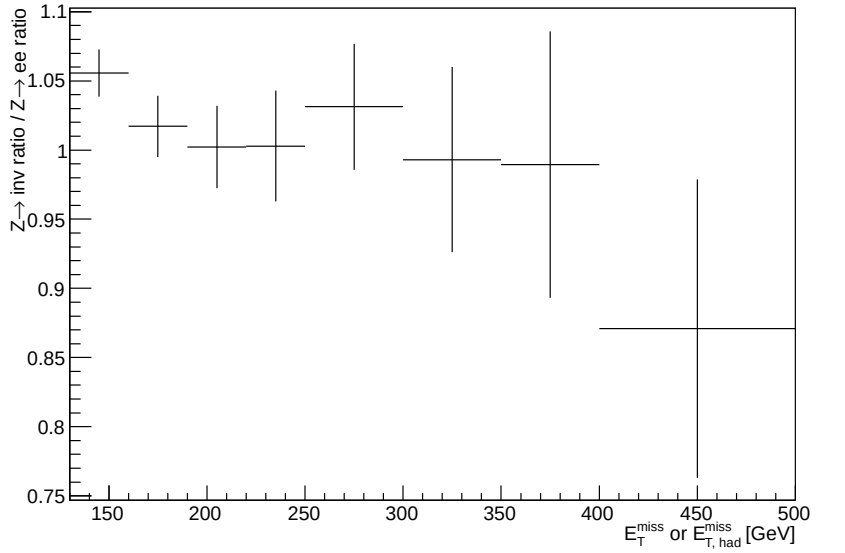


Figure 6.6: Ratio of the pileup stability as a function of $E_{\mathrm{T}}^{\mathrm{miss}}$ or $E_{\mathrm{T,had}}^{\mathrm{miss}}$ in the neutrino and electron channels.

6.6 Combined systematic uncertainty

For each bin in the differential measurement the systematic uncertainties were calculated as the sum, in quadrature, of all estimated systematic uncertainties. The total systematic uncertainty on the measurement was then calculated as the weighted average, where the weight in each bin, i, was

$$w_i = 1/(\sigma_i^{\text{stat}})^2 \tag{6.3}$$

The total systematic uncertainty is found to be ± 21.6 MeV, or $\pm 4.5\%$. A summary of the systematic uncertainties is shown in table 6.2. The uncertainty on the $W \to \tau\nu$ background is by far the dominant systematic uncertainty in the measurement.

The final measurement of the invisible width, including statistical and systematic uncertainties was found to be

$$\Gamma(Z \to \text{inv}) = 480.5 \pm 5.0(\text{stat.}) \pm 21.6(\text{syst.}). \tag{6.4}$$

Figure 6.7 shows the measured width as a function of Z p_{T} including both statistical and systematic uncertainties. The final result will be discussed in chapter 7.

A fit for a constant value of the invisible width can be made using the combined

Table 6.2: Systematic uncertainties on the invisible width measurement.

Source	Systematic uncertainty (MeV, %)
$W \to \tau\nu$ bkg	17.0, 3.5
Electron energy	8.7, 1.8
Electron ID	5.1, 1.1
Jet energy	2.5, 0.5
$Z \to \nu\nu$ QCD	3.0, 0.6
$Z \to ee$ QCD	1.5, 0.3
PDFs	2.0, 0.4
Total	21.6, 4.5

statistical and systematic uncertainties. The result of this fit finds

$$\Gamma(Z \to \text{inv}) = 470.5 \pm 10.7, \tag{6.5}$$

with

$$\chi^2/\text{NDF} = 0.75. \tag{6.6}$$

This fit has a better χ^2 value, however the first result is considered better defined since this second fit includes a large statistical uncertainty due to the scaling of the $W \to \tau\nu$ background which was arbitrary chosen. Varying this arbitrary scaling has a large impact on this combined fit, and so the fit with only statistical uncertainties is quoted as the main result in this thesis.

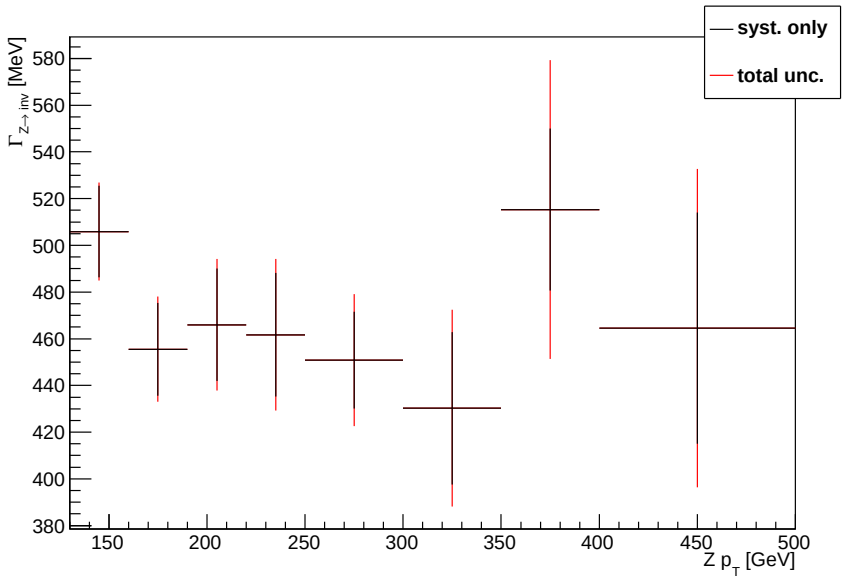


Figure 6.7: Measured invisible width of the Z boson as a function of its p_{T}.

Chapter 7

Discussion of results

The analysis was carefully designed to allow a precise measurement of the invisible width of the Z boson using the ATLAS detector with data from the 2013 LHC run. Events were selected in both $Z \to \text{inv}$ and $Z \to ee$ channels. Backgrounds in each channel were measured using a combination of Monte Carlo and data driven estimations, which were removed from the selected events. A number of corrections were estimated and applied to take into account the differences introduced by the final state leptons to correct the measured ratio to a ratio of the Z branching ratios. This was then multiplied by the world average value for the Z's partial width to electrons to find the invisible width. The invisible width of the Z boson has been measured to be

$$\Gamma(Z \to \text{inv}) = 481 \pm 5(\text{stat.}) \pm 22(\text{syst.}) \text{ MeV}, \tag{7.1}$$

which is consistent with the precisely measured indirect measurement of $\Gamma(Z \to \text{inv})_{\text{ind}} = 499.0 \pm 1.5$ MeV [3]. Further, this measurement rivals the precision of the LEP direct measurements, which have a combined result of 503 ± 16 MeV [3].

The measured invisible width is consistent with the Standard Model expectation (given in the indirect measurement) and therefore does not show any evidence of physics beyond the Standard Model. The measurement was also performed as a function of the Z boson p_{T}. This was done since additional contributions to

the measured ratio, for example from new, non-interacting particles mimicking the $Z \rightarrow$ inv channel, may only appear above a threshold given by their mass. No significant deviations are seen in the higher p_{T} bins of the measurement, however the uncertainties mean that the measurement is not yet sensitive to small additional signals.

The relative statistical uncertainty on the measurement is 1.4%. The contribution to this uncertainty from the data sample is 0.5%. The remaining statistical uncertainty comes from the Monte Carlo samples used to estimate the backgrounds given in chapter 4 and the corrections calculated in chapter 5. The total statistical uncertainty could therefore be improved by generating larger MC samples, specifically the $Z \rightarrow \nu\nu$ sample to match the size of the much larger $Z \rightarrow ee$ sample used in the corrections. Increased $W \rightarrow l\nu$ samples would also improve the background estimations, particularly the $W \rightarrow \tau\nu$ sample, which forms the largest background in the measurement yet has the smallest simulated sample.

The systematic uncertainty due to the Jet Energy Scale is only 2.5 MeV. The small uncertainty is due to the fact that the measurement is well designed. By taking advantage of the ratio of $Z \rightarrow \nu\nu$ and $Z \rightarrow ee$ channels with very similar hadronic characteristics the Jet Energy Scale uncertainty was minimised.

The dominant systematic uncertainty on the measurement comes from the estimation of the $W \rightarrow \tau\nu$ background. A data driven estimation of the hadronically decaying $W \rightarrow \tau\nu$ background would remove this systematic uncertainty, however it is much more difficult to estimate than the $W \rightarrow e\nu$ or $W \rightarrow \mu\nu$ backgrounds. Whilst a high purity $W \rightarrow e\nu$ or $W \rightarrow \mu\nu$ data sample can be selected simply by altering the $Z \rightarrow$ inv selection to require a single electron or muon, a high purity hadronic $W \rightarrow \tau\nu$ sample will be difficult to select. Designing such a selection will require studies of various methods, such as requiring an isolated track, but no electrons or muons to try and select single prong τ jets. Additionally considering reversing the $\Delta\phi(\mathrm{jet}, E_{\mathrm{T}}^{\mathrm{miss}})$ cut may help, as this sample has a large $W \rightarrow \tau\nu$ contribution. Using ATLAS τ identification methods will also help, although care will

need to be taken in assessing them in the high $E_{\mathrm{T}}^{\mathrm{miss}}$ region used in the analysis. An important consideration in forming a hadronic τ sample to use in a data/MC scaling estimation will be that it will be difficult to minimise the QCD background in this sample, which will also be difficult to quantify. As such the development of a data driven hadronic $W \to \tau\nu$ background estimation is a task which is beyond the scope of this thesis.

The systematic uncertainties due to the electron energy and identification efficiency are important uncertainties. Since the leptons differ in the two channels there is no cancellation of these uncertainties. Looking forward, they may reduce as the understanding of the performance with which ATLAS detects and measures electrons improves. These two uncertainties are likely to be the limiting factor in minimising the systematic uncertainty on this measurement. However, if these two uncertainties were to become the dominant ones the measurement would have a systematic uncertainty better than that in L3's measurement. Given that the statistical uncertainties are already lower than L3's statistical uncertainty, it should be possible for ATLAS to make the world's most precise direct measurement of the invisible width of the Z boson. An improved measurement could be made by also considering the ratio of the invisible channel to a $Z \to \mu\mu$ channel. This second measurement would share most of the systematic uncertainties except for those due to the elections. Additionally, the uncertainties due to muons are likely to be reduced compared to those originating from electrons. This is expected since the muons are minimally ionising, and therefore deposit little energy in the calorimeter. The muons should therefore have only a very small impact on the jet phase space difference between the invisible and muon channels.

The measurement could also be improved by a data driven estimation of the $E_{\mathrm{T}}^{\mathrm{miss}}$ trigger efficiency. Since muons are not used in the trigger level calculations of the $E_{\mathrm{T}}^{\mathrm{miss}}$, an analysis of the trigger efficiency for the $Z \to$ inv events could be made using a $Z \to \mu\mu$ data sample. By selecting events with very similar hadronic activity and correcting for the small energy loss of the muons in the calorimeter,

the $E_{\mathrm{T}}^{\mathrm{miss}}$ trigger efficiency could be measured directly. It is expected that such an improvement would only impact the lowest Z p_{T} bin in the analysis, since the trigger is seen to be almost fully efficient in higher p_{T} bins. The measurement may also be slightly improved due to ongoing measurements of the reconstruction performance for the electrons, jets and $E_{\mathrm{T}}^{\mathrm{miss}}$.

Finally, the measurement could be improved by also considering the ratio of $Z \to \mathrm{inv}/Z \to \mu\mu$. Whilst such an analysis would require a detailed study of the corrections on the measured ratio and the background estimations it is hoped that this thesis will provide significant help in doing such an analysis. Not only would combining the results of $Z \to \mathrm{inv}/Z \to ee$ with $Z \to \mathrm{inv}/Z \to \mu\mu$ improve the data statistics, it would also provide a strong check that the experimental design to reduce the impact of the electrons on the $Z + \mathrm{jet}$ event selection is correct.

It is hoped that with some or all of these improvements implemented the invisible width measurement at ATLAS will be the most precise direct measurement in the world and that it will provide a robust method of searching for new physical phenomena beyond the Standard Model.

Chapter 8

Conclusion

The invisible width of the Z boson is a quantity that is well understood within the Standard Model. It was measured very precisely using an indirect method by the LEP experiments and also measured in a less precise direct method. A direct measurement has been performed using the ATLAS detector at the LHC which provides a test of the Standard Model in a very different energy regime in a hadronic environment.

The measurement was carefully designed to take advantage of a ratio of the $Z \to \text{inv}$ and $Z \to ee$ channels to cancel many experimental uncertainties. Events were selected in the two channels to make the Z + jet event selection as similar as possible. Estimations of the backgrounds in each channel were removed. The measured ratio was then corrected for a number of differences introduced by the difference in the neutrino and electron selections. The systematic uncertainties due to theoretical and detector effects were estimated and the invisible width measured with the ATLAS detector was found to be

$$\Gamma(Z \to \text{inv}) = 481 \pm 5(\text{stat.}) \pm 22(\text{syst.}) \text{ MeV}. \tag{8.1}$$

This measurement rivals the precision of the LEP experiments and shows no evidence for deviation from the Standard Model.

This thesis not only provides a measurement of a well understood Standard

Model quantity but can also be used in robust searches for new physical phenomena that would contribute to the invisible channel. The measurement was made as a function of the Z boson's p_{T} with all detector effects corrected in order to provide sensitivity to any additional contributions that appear above a threshold energy. No such contributions were seen, however the statistical and systematic uncertainties could hide a small contribution. Improvements to the measurement have been suggested that will reduce both statistical and systematic uncertainties and therefore help provide a more precise measurement at high Z p_{T} and allow limits on theories to be calculated.

Bibliography

[1] B. T. Huffman, C. Issever, N. C. Ryder, and A. R. Weidberg, "The radiation hardness of specific multi-mode and single-mode optical fibres at -25c beyond a full slhc dose to a dose of 500 kgy(si)," *Journal of Instrumentation*, vol. 5, no. 11, p. C11023, 2010.

[2] N. C. Ryder, P. Hamilton, B. T. Huffman, P. K. Teng, A. R. Weidberg, and C. Issever, "The radiation hardness and temperature stability of planar light-wave circuit splitters for the high luminosity lhc," *Journal of Instrumentation*, vol. 6, no. 10, p. P10007, 2011.

[3] J. Beringer *et al.*, "Review of particle physics," *Phys. Rev. D*, vol. 86, p. 010001, Jul 2012.

[4] The ATLAS Collaboration, "Search for New Phenomena in Monojet plus Missing Transverse Momentum Final States using 10fb-1 of pp Collisions at sqrts=8 TeV with the ATLAS detector at the LHC," Tech. Rep. ATLAS-CONF-2012-147, CERN, Geneva, Nov 2012.

[5] The ALEPH Collaboration, "Measurement of the Z resonance parameters at LEP," *Eur. Phys. J. C*, vol. 14, pp. 1–50, 2000.

[6] The DELPHI Collaboration, "Cross-sections and leptonic forward-backward asymmetries from the Z^0 running of LEP," *Eur. Phys. J. C*, vol. 16, pp. 371–405, 2000.

[7] L3 Collaboration, "Measurement of cross sections and forward-backward asymmetries at the Z resonance and determination of electroweak parameters," *Eur. Phys. J. C*, vol. 16, pp. 1–40, 2000.

[8] The OPAL Collaboration, "Precise determination of the Z resonance parameters at LEP: 'Zedometry'," *Eur. Phys. J. C*, vol. 19, pp. 587–651, 2001.

[9] ALEPH Collaboration, "A direct measurement of the invisible width of the Z from single photon counting," *Phys. Lett. B*, vol. 313, pp. 520–524, 1993.

[10] L3 Collaboration, "Determination of the number of light neutrino species from single photon production at LEP," *Phys. Lett. B*, vol. 431, pp. 199–208, 1998.

[11] OPAL Collaboration, "Measurement of single photon production in e^+e^- collisions near the Z^0 resonance," *Z. Phys. C*, vol. 65, pp. 47–65, 1995.

[12] CDF Collaboration, "Direct measurement of the invisible width of the Z^0 boson using monojet events." `http://http://www-cdf.fnal.gov/physics/ewk/2007/ZnunuWidth/`, 2007.

[13] J. Pumplin, A. Belyaev, J. Huston, D. Stump, and W. Tung, "Parton distributions and the strong coupling: CTEQ6AB PDFs," *JHEP*, vol. 0602, p. 032, 2006.

[14] A. Martin, W. Stirling, R. Thorne, and G. Watt, "Parton distributions for the LHC," *Eur.Phys.J.*, vol. C63, pp. 189–285, 2009.

[15] ATLAS Collaboration, "Diagram of the ATLAS detector." `http://www.atlas.ch/photos/full-detector-cgi.html`, 2013.

[16] The ATLAS Collaboration, "The ATLAS experiment at the CERN large hadron collider," *Journal of Instrumentation*, vol. 3, p. S08003, Aug. 2008.

[17] The ATLAS Collaboration, "Jet energy measurement and its systematic uncertainty in proton–proton collisions at $\sqrt{s} = 7$ TeV with the ATLAS detector," 2014.

[18] M. Cacciari, G. P. Salam, and G. Soyez, "The anti-kt jet clustering algorithm," *Journal of High Energy Physics*, vol. 2008, p. 063, Apr. 2008.

[19] The ATLAS Collaboration, "Jet Energy Scale uncertainties." `https://twiki.cern.ch/twiki/bin/view/AtlasPublic/JetEtmissApproved2013JESUncertainty`, 2013.

[20] The ATLAS Collaboration, "Electron efficiency measurements with the ATLAS detector using the 2012 LHC proton-proton collision data," Tech. Rep. ATLAS-CONF-2014-032, CERN, Geneva, Jun 2014.

[21] The ATLAS Collaboration, "Update of electron efficiency plots." `https://atlas.web.cern.ch/Atlas/GROUPS/PHYSICS/EGAMMA/PublicPlots/20130926/ATL-COM-PHYS-2013-1287/index.html`, 2013.

[22] The ATLAS Collaboration, "Preliminary results on the muon reconstruction efficiency, momentum resolution, and momentum scale in ATLAS 2012 pp collision data," Tech. Rep. ATLAS-CONF-2013-088, CERN, Geneva, Aug 2013.

[23] The ATLAS Collaboration, "Performance of Missing Transverse Momentum Reconstruction in ATLAS studied in Proton-Proton Collisions recorded in 2012 at 8 TeV," Tech. Rep. ATLAS-CONF-2013-082, CERN, Geneva, Aug 2013.

[24] The ATLAS Collaboration, "Performance of Missing Transverse Momentum Reconstruction in ATLAS studied in Proton-Proton Collisions recorded in 2012 at 8 TeV," Tech. Rep. ATLAS-CONF-2013-082, CERN, Geneva, Aug 2013.

[25] M. Wielers, R. Mantifel, A. Tricoli, and P. Bell, "Single Electron Trigger Performance Plots," Tech. Rep. ATL-COM-DAQ-2012-146, CERN, Geneva, Jun 2012. Also available at `https://twiki.cern.ch/twiki/bin/view/AtlasPublic/EgammaTriggerPublicResults`.

[26] The ATLAS Collaboration, "Characterisation and mitigation of beam-induced backgrounds observed in the ATLAS detector during the 2011 proton-proton run," *JINST*, vol. 8, p. P07004, 2013.

[27] T. Gleisberg, S. Hoeche, F. Krauss, M. Schonherr, S. Schumann, *et al.*, "Event generation with SHERPA 1.1," *JHEP*, vol. 0902, p. 007, 2009.

[28] H.-L. Lai, M. Guzzi, J. Huston, Z. Li, P. M. Nadolsky, J. Pumplin, and C.-P. Yuan, "New parton distributions for collider physics," *Phys. Rev. D*, vol. 82, p. 074024, Oct 2010.

[29] S. Alioli, P. Nason, C. Oleari, and E. Re, "A general framework for implementing NLO calculations in shower Monte Carlo programs: the POWHEG BOX," *JHEP*, vol. 1006, p. 043, 2010.

[30] B. P. Kersevan and E. Richter-Was, "The Monte Carlo event generator AcerMC version 2.0 with interfaces to PYTHIA 6.2 and HERWIG 6.5," 2004.

[31] T. Sjöstrand, S. Mrenna, and P. Skands, "PYTHIA 6.4 physics and manual," *Journal of High Energy Physics*, vol. 2006, no. 05, p. 026, 2006.

[32] M. Whalley, D. Bourilkov, and R. Group, "The Les Houches accord PDFs (LHAPDF) and LHAGLUE," *arXiv hep-ph/0508110*, 2005.

[33] The ATLAS Collaboration, "Electron performance measurements with the ATLAS detector using the 2010 LHC proton-proton collision data," *The European Physical Journal C*, vol. 72, no. 3, pp. 1–46, 2012.